MICROCOPY RESOLUTION TEST CHART

NATIONAL BUREAU OF STANDARDS-1963-A

AFWAL-TR-83-2044
Part III

AD-A134 693

LASER DIAGNOSTIC DEVELOPMENT AND MEASUREMENT AND
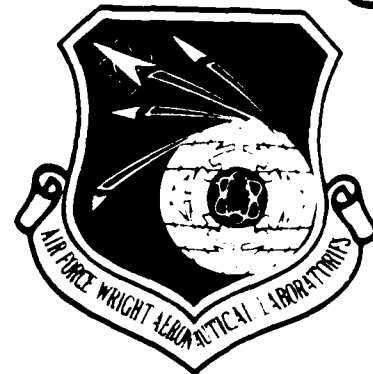MODELING OF TURBULENT FLOWFIELDS OF JETS AND WAKES

Part III
The Development of a Two-Channel CW Time-Resolved Laser Raman
Spectroscopy (TiLaRS) System for Measurements in Gas Flowfields

P. P. Yaney, R. J. Becker, P. T. Danset, and M. R. Gallis
University of Dayton
Research Institute
Dayton, Ohio 45469

June 1983

FINAL REPORT FOR PERIOD 1 APRIL 1978 - 30 SEPTEMBER 1982

AERO PROPULSION LABORATORY
AIR FORCE WRIGHT AERONAUTICAL LABORATORIES
AIR FORCE SYSTEMS COMMAND
WRIGHT-PATTERSON AIR FORCE BASE, OH   45433

DTIC FILE COPY

NOTICE

When Government drawings, specifications, or other data are used for any purpose other than in connection with a definitely related Government procurement operation, the United States Government thereby incurs no responsibility nor any obligation whatsoever; and the fact that the government may have formulated, furnished, or in any way supplied the said drawings, specifications, or other data, is not to be regarded by implication or otherwise as in any manner licensing the holder of any other person or corporation, or conveying any rights or permission to manufacture use, or sell any patented invention that may in any way be related thereto.

This report has been reviewed by the Office of Public Affairs (ASD/PA) and is releasable to the National Technical Information Service (NTIS). At NTIS, it will be available to the general public, including foreign nations.

This technical report has been reviewed and is approved for publication.

W. M. Roquemore
W. M. ROQUEMORE
Fuels Branch
Fuels and Lubrication Division
Aero Propulsion Laboratory

Arthur V. Churchill
ARTHUR V. CHURCHILL,
Chief, Fuels Branch
Fuels and Lubrication Division
Aero Propulsion Laboratory

FOR THE COMMANDER

Benito P. Botteri
BENITO P. BOTTERI, Assistant Chief
Fuels and Lubrication Division
Aero Propulsion Laboratory

REPORT DOCUMENTATION PAGE	READ INSTRUCTIONS BEFORE COMPLETING FORM

1. REPORT NUMBER	2. GOVT ACCESSION NO.	3. RECIPIENT'S CATALOG NUMBER
AFWAL-TR-83-2044, Part III	AI94693	

4. TITLE *(and Subtitle)*	5. TYPE OF REPORT & PERIOD COVERED
Laser Diagnostic Development and Measurement and Modeling of Turbulent Flowfields of Jets and Wakes, Part III	Final Report for Period 1 Apr 1978- 30 Sept 1982
	6. PERFORMING ORG. REPORT NUMBER
	UDR-TR-83-52

7. AUTHOR(s)	8. CONTRACT OR GRANT NUMBER(s)
P. P. Yaney, R. J. Becker, P. T. Danset, and M. R. Gallis	F33615-78-C-2005

9. PERFORMING ORGANIZATION NAME AND ADDRESS	10. PROGRAM ELEMENT, PROJECT, TASK AREA & WORK UNIT NUMBERS
University of Dayton Research Institute Dayton, Ohio 45469	P.E. # 62203F, Proj. # 3048, W.U. # 30480596

11. CONTROLLING OFFICE NAME AND ADDRESS	12. REPORT DATE
Aero Propulsion Laboratory (AFWAL/POSF) Air Force Wright Aeronautical Laboratories (AFSC) Wright-Patterson Air Force Base, Ohio 45433	June 1983
	13. NUMBER OF PAGES
	133

14. MONITORING AGENCY NAME & ADDRESS(if different from Controlling Office)	15. SECURITY CLASS. *(of this report)*
	Unclassified
	15a. DECLASSIFICATION DOWNGRADING SCHEDULE

16. DISTRIBUTION STATEMENT *(of this Report)*

Approved for Public Release, Distribution Unlimited

17. DISTRIBUTION STATEMENT *(of the abstract entered in Block 20, if different from Report)*

18. SUPPLEMENTARY NOTES

19. KEY WORDS *(Continue on reverse side if necessary and identify by block number)*

Optical Probe Techniques	Optical Multichannel Detection
Spontaneous Raman Spectroscopy	CH_4 Flame
Rotational Raman Scattering	CO_2 Jet
Molecular Spectroscopy	Axisymmetric Free Jet
Time-Resolved Spectroscopy	Temperature Measurements in Flames

20. ABSTRACT *(Continue on reverse side if necessary and identify by block number)*

The design and performance of a photon counting, two-channel spectroscopic system using the 6-W, 488-nm line of a cw argon ion laser is described. The two channels are formed by the use of cylindrical optics and special slit mirrors set up following the exit slit of a conventional double spectrometer. The system is capable of dynamic, simultaneous measurements of either the concentrations of two gas species in cold flow or the temperature and

DD FORM 1 JAN 73 1473 EDITION OF 1 NOV 65 IS OBSOLETE

19. Concentration Measurements in Gases
     Noise Analysis
     Processing Random Signals

20. concentration of a single gas species, such as N_2 in a flame.
     The measurements are accomplished by recording the intensities
     of two spontaneous rotational Raman lines with spectral band-
     widths between 0.04 and 0.08 nm. Up to 4096 samples (or reads
     from each of the two channels) can be recorded by a dedicated
     minicomputer at rates up to 10 kHz. Studies of a CH_4 diffu-
     sion flame at sampling rates of 20 to 100 Hz and a room-tem-
     perature, axisymmetric CO_2 jet at rates up to 2.0 kHz were
     carried out. The analysis of the data from these studies in-
     clude mean and rms profiles, probability density functions
     (pdf's), power spectral density functions, autocorrelation
     functions, cross correlation functions, and determinations of
     skewness and kurtosis in the pdf's and the CO_2 fluctuations.

Accession For		
NTIS GRA&I	X	
DTIC TAB	☐	
Unannounced	☐	
Justification		
By		
Distribution/		
Availability Codes		
Dist	Spe	
A-1		

DTIC
COPY
INSPECTED
2

PREFACE

iii

TABLE OF CONTENTS

LIST OF ILLUSTRATIONS

LIST OF TABLES

x

LIST OF SYMBOLS

Symbols

$\left. \begin{array}{l} a, b \\ e, d \end{array} \right\}$ Constants defined in text.

$\dot{b}$ Background count rate averaged over a single read $(\sec^{-1})$.

$\dot{b}'$ Total corrected non-Raman count rate $(\sec^{-1})$.

$\left. \begin{array}{l} \bar{b}'_{BB} \\ R_B, \; R_f \end{array} \right\}$ Quantities defined in text.

B_0 Rotational constant for state $v = 0$.

B_v Rotational constant for vibrational state v.

c Speed of light, 2.998×10^8 m/s.

c Concentration (mole-fraction or m-f).

$\left. \begin{array}{l} C_A, C_B \\ K_A, K_B \\ K_1, K_2 \end{array} \right\}$ Constants defined in text.

$C(\tau)$ Autocorrelation coefficient which is the autocorrelation function normalized by the variance, $R(\tau)/R(0)$.

$\dot{d}$ Photomultiplier dark count rate averaged over a single read $(\sec^{-1})$.

E_J Energy of state J relative to the ground state (cm^{-1}).

f Fluctuation frequency (Hz).

f_b Sampling or read frequency (or rate) during a background measurement (Hz).

f_r Sampling or read frequency (or rate) during a Raman measurement (Hz).

g_J Nuclear spin factor for state J.

G, G_A, G_B Channel gain factors.

$G(f)$
G_p, G_T } Power spectral densities (K^2/Hz or m-f^2/Hz).

h Planck constant, 6.626×10^{-34} J/s.

I Nuclear spin quantum number.

J Initial-state quantum number of rotational transition.

k Boltzmann constant, 1.381×10^{-23} J/K.

ℓ Effective length of excited volume (cm).

M Average total number of counts per read.

$\dot{M}$ Total count rate averaged over a single read (sec^{-1}).

$\overline{M}$ Average total count rate taken over all reads (sec^{-1}).

M_j Factorial moments of measured distribution, $p(M, \Delta t)$.

n Number of Raman photoelectrons per read.

$\dot{n}$ Number of Raman photoelectrons per second averaged over a single read.

N Average molecular concentration during read interval (cm^{-3} or m^{-3}).

N_J Average population density in Jth state during read interval (cm^{-3}).

N_r Reference gas concentration (cm^{-3}).

p Gas pressure (Newtons/m^2).

$p(M, \Delta t)$ Measured photoelectron count distribution function for a read time of Δt.

$P(c)$ Concentration probability density function (m-f^{-1}).

P_e Average excitation photon rate incident on observed volume (sec^{-1}).

Q_v Rotational partition function.

r, d Radius, diameter of nozzle orifice.

R_m — Ratio A to B of Raman counts per read of 60 and 84-cm^{-1} lines.

R_0 — Ratio A to B of Raman counts per read for lines J_A and J_B.

R_ε — Responsivity of channel A relative to channel B.

$R(\tau)$ — Autocorrelation function (K^2 or $m-f^2$).

s — Standard deviation.

s_{ac} — Air-CO_2 covariance (see text).

t_c — Integral time scale (sec).

T — Absolute temperature (K).

v — Vibrational quantum number.

W — Integrated photon count rate on PMT during Δt.

X,Y,Z — Nozzle coordinates (cm).

α_e — Rotation-Vibration interaction constant (cm^{-1}).

β_3 — Skewness ($\mu_3/\mu_2^{1.5}$).

β_4 — Kurtosis (μ_4/μ_2^2).

γ — Anisotropy factor of the molecular-polarizability tensor (cm^3).

Δt — Time interval of one read (sec).

ε — System detection efficiency, vis. overall optical transmittance times η.

η — Quantum efficiency of PMT.

λ — Wavelength of light (cm or nm).

μ_m — Central moments of concentration distribution, P(c).

ν_J — Frequency of Raman scattered light from state J (cm^{-1}).

ν_L — Frequency of laser light (cm^{-1}).

ξ — Function defined in text.

σ_J Differential rotational Raman scattering cross section of state J (cm^2/ster).

τ Time delay (sec)

T   Defined in text.

Ω Solid angle of collection for Raman scattered light (ster).

Subscripts and Other Labels

a,c   Air, CO_2

A,B   Channels

r   Reference or calibration value

"$-$"   Average over all samples in data set

"."   Time rate of change (sec^{-1})

p   Poisson

Acronyms and Abbreviations

acf   Autocorrelation function

APL   Aero Propulsion Laboratory

ASME   American Society of Mechanical Engineers

BCD   Binary coded decimal

CARS   Coherent anti-Stokes Raman spectroscopy

ccf   Cross-correlation function

cw   Continuous wave

fwhm   Full width at half maximum

GPIB   General purpose interface board

NIM   Nuclear instrument module

pdf   Probability density function

PMT   Photomultiplier tube

ppm   Parts per million

prf   Pulse repetition frequency

psdf   Power spectral density function

QE   Quantum efficiency

RS   Spontaneous Raman scattering

TiLaRS   Time-resolved laser Raman spectroscopy

SECTION 1
INTRODUCTION AND BACKGROUND

This three-part final report documents the research program performed for the Air Force Wright Aeronautical Laboratories, Aero Propulsion Laboratory, by the University of Dayton. The research had two overall objectives: (a) providing profile data that can be used to evaluate combustor and fuel combustion models and (b) evaluating the performance of combustor models and different diagnostic techniques in various combustion environments.

The technical efforts dealing with the design and development of a two-dimensional laser Doppler anemometer are described in Part I, with the experimental data collected. The analysis and modeling tasks involving the numerical flowfield predictions and their comparisons with the experimental data are described in Part II. The design, development and performance of a two-channel time-resolved laser Raman spectroscopy system are described in this volume, Part III of the report.

1.1 BACKGROUND

The development of laser-based optical diagnostic probes using spontaneous Raman scattering (RS) in combustion and gaseous flow measurements has achieved a reasonable degree of success in characterizing time-averaged temperature spatial profiles in steady flows.[1,2,3] Measurements have been systematically carried out in which the Raman temperatures have been shown to be in excellent agreement with the temperatures determined from standard thermocouple and gas-sampling probe data.[4,5] However, characterization of turbulent flow requires the capability of resolving not only spatial differences, but more important, the temporal fluctuations as well. Basically, the type of measurement that can be made is determined to a large extent by

1

the type of laser being used. Generally, high-energy, ($\gtrsim 1$ J), short-pulse ($\lesssim 1\mu s$) lasers with suitable beam and wavelength characteristics are limited to low ($\lesssim 20/s$) repetition rates. This means that techniques utilizing such lasers can provide probability density functions (pdf's) of the fluctuating variable.[6,7,8] However, since the frequency spectrum is limited to half the measurement rate (Nyquist interval),[9] little information regarding the frequency content of the fluctuations can be obtained. Pulsed lasers of the Q-switched variety are being used in nonlinear scattering techniques such as coherent anti-Stokes Raman spectroscopy (CARS) to generate pdf's of temperature and species concentration in various turbulent flows,[10,11] while a flashlamp-pumped dye laser has been successfully employed to generate pdf's in a turbulent diffusion hydrogen flame using RS.[8]

Ideally, the most fruitful experimental approach to characterizing the fluctuations of any variable is to record in real time the values of that variable. Then, the power spectral density function (psdf) or the autocorrelation function (acf), as well as the pdf and other statistical parameters, can be determined. To avoid aliasing in the common circumstance involving nearly instantaneous sampling and a synchronous sampling rate, the sampling frequency must be high compared to the highest frequency contained in the signal to be recorded. This measurement scenario can be accomplished with a cw laser; however, since the power is too low for nonlinear techniques to be viable, some other scattering phenomenon must be used. The signals available in a typical RS measurement on a gas such as N_2 are, for example, commonly on the order of 100's of counts/sec. If the measurements were made over 10 ms intervals (i.e., a 100 Hz read rate), then on the order of one count could be expected for any measurement. The resulting high statistical uncertainties would require a very large number of measurements to be made before results of any value could be expected.[7] Thus,

2

to make real time measurements using light scattering, schemes for enhancing the signal must be used.

Higher signal count rates can be achieved several ways. One way is to use a molecule with a large scattering cross section. For example, concentration fluctuation studies have been carried out with RS on turbulent[12] and unsteady[13] flows using CH_4 which has a vibrational Raman scattering cross section nearly an order of magnitude higher than N_2.[14] Another approach is to use elastic, that is, Rayleigh scattering instead of an inelastic scattering scheme of which RS is an example. Rayleigh scattering, which is observed at the laser wavelength, is about 10^3 times stronger than the vibrational Raman signal due to the Q branch of N_2. The Rayleigh signal from a gaseous sample is related to the total number density in the observed volume. In subsonic cold flow, this relationship is expected to be a proportionality. In combustion flows, the effective overall Rayleigh cross section can be adjusted by introducing "dopant" gases so as to become almost independent of the state of the gases, namely unburned, burning, or combustion products.[15] In these special cases, the observed Rayleigh signal is proportional to the total number density. Furthermore, if the pressure is constant throughout the flow, the temperature can be obtained by application of the ideal gas law.[15] Because of the very large signal levels and the simplicity of only a single measurement, this method is very attractive for making dynamic measurements of temperature in turbulent flows.

The above approaches, by themselves, have a rather limited capability with respect to providing information concerning the mixing processes in turbulent cold and combustion flow fields. The dominant constituent in any air-breathing combustion flow field is N_2 and two of the principal molecules in the combustion process, aside from H_2O and the fuel, are O_2 and CO_2. Therefore, a great deal of information concerning mixing processes in turbulent combustion flow can be obtained by studying the

simultaneous fluctuations of temperatures and the concentrations of these three molecules. This requires a measurement approach that provides strong signals using a cw laser and species selectivity. Selectivity in light scattering by the above molecules means a Raman technique is needed and the strongest RS signals from these molecules are from the pure rotational RS lines.[16] However, the rotational lines for these molecules are densely spaced ($\gtrsim 3$ cm^{-1}) in bands within 100-200 cm^{-1} on either side of the laser frequency. This means that fairly high spectral resolution is required (i.e, <1 cm^{-1}) to achieve the desired selectivity and that there will be interferences between at least some of the lines of the different species.

Ideally, what is needed here is a high read rate optical multichannel detection system. Low read rates, as used by CARS, permit the use of detector arrays.[10,11] Data rates in excess of 30 Hz can presently be accomplished only by some sort of polychromator approach using photomultiplier tubes (PMT's). Such an approach, for example, is being used to measure the Rayleigh line and RS from the Q branches of various molecules simultaneously with velocity measurements using laser Doppler velocimetry (LDV).[17] Spontaneous Raman scattering measurements of this sort, however, require high-energy, pulsed lasers which permit measurements of, at most, pdf's and joint pdf's. Furthermore, because the read rate is so low (~ 1 Hz), it is difficult to acquire enough measurements to clearly identify the characteristics of the desired statistical functions. Therefore, if two or more pure rotational RS lines are to be measured simultaneously, a PMT-based polychromator must be constructed.

The primary concept in measuring the concentration of a gas or its temperature using an optical probe is the spectroscopic detection of laser-excited emissions or scattered light from specific spectral features of the gas which contain the desired information. For Raman temperature measurements in air, it is

4

convenient (and customary) to use N_2 as the probe molecule. In the rotational spectrum, the temperature can be obtained from the ratio of the intensities of any two lines[18] or groups of lines.[1] A feature common to all such two-frequency measurements is the requirement that any laser-induced background spectrum be reasonably steady in magnitude and shape. This restricts the measurements to noncombusting flows or to relatively clean flames. Constant background signals, such as PMT dark count and ambient light, can be subtracted out with no difficulty, provided they are small compared to the Raman signal.

The objective of this work was to develop the capability for making real-time measurements of temperature and species concentrations as a function of position in turbulent flow. An important part of this goal was to characterize the temporal mixing processes in turbulent cold flow. Both temperature and fuel-air mixing processes require that a minimum of two simultaneous wavelength channels be recorded. With two channels, these two types of measurements are mutually exclusive. Although more channels could have been designed into the current system, it was decided that the additional complexity and cost were not warranted and could best be deferred to later system upgrading. System performance objectives were to record the two wavelength channels at up to at least 1 kHz read rates from a sample volume of <1 mm^3. For example, a fluctuation frequency capability out to 1 kHz, corresponding to an integral time scale of about 1 ms, would permit a reasonable range of turbulent flows to be investigated.[19] This would require a read rate of at least 2 kHz. For a 10% Poisson uncertainty for a single measurement, an average count per read of 100 would be necessary. This means average count rates on the order of 200 kcounts/s are required. Such count rates were obtained in this work with a CO_2 jet in room temperature air; however, the signals were considerably lower in a flame. This report describes the development of a two-channel, time-resolved laser Raman spectroscopy system. This

5

system, hereafter referred to as the TiLaRS system, was designed
to measure simultaneously two rotational Raman lines in real
time.   A dedicated minicomputer records the two channels in less
than 1 μs. An optical multipass cell increased the laser beam
intensity in the observed volume by a factor of about 13.   A
reverse-optics mirror nearly doubled the observed signal.   High
quantum efficiency PMT's were used along with an argon ion laser
giving about 6 W at 488 nm.   The essential features of this
system and some of the preliminary results are presented.

SECTION 2
THEORY

2.1 GENERAL

The theory of RS and the results of experimental studies,
particularly for diatomic molecules, have been reported in great
detail.[16,20-23] Only those features of the theory essential to
the derivation of the working equations will be presented. The
objective is to determine expressions relating concentration and
temperature to the observed intensities and the corresponding
uncertainties to the measurement parameters. The rotational
energy levels are labeled by the rotational quantum number J.
Pure Stokes rotational Raman transitions of a diatomic molecule
can occur only to levels where J increases by two.[20] Thus,
expressions for given transitions are adequately identified by
the initial J value of the transition.

The 90°-scattering geometry was used in this work wherein
the direction in which the scattered light is collected was, on
the average, at a right angle to the focused laser beams. The
average number of photoelectrons per second $\dot{n}_J$, measured at the
anode of a PMT during a given read time interval Δt due to light
of frequency ν_J scattered into the collecting solid angle Ω
resulting from a $J \rightarrow J + 2$ rotational transition is given by

$$\dot{n}_J = \varepsilon P_e \sigma_J \Omega \ N_J \ell \nu_L / \nu_J,\tag{1}$$

where P_e is the average excitation photon rate incident on the
observed volume during Δt due to the laser light having frequency
ν_L, ε is the system detection efficiency factor which includes

7

the transmittance of the optics and the spectrometer and the PMT quantum efficiency, σ_J is the differential rotational Raman scattering cross section in cm^2/ster, N_J is the average number of molecules per cm^3 in the initial state J during Δt, and ℓ is the effective length in cm of the focused laser-beam image passed through the entrance slit of the spectrometer. The ratio ν_L/ν_J can be dropped from Equation (1) since it is essentially unity for pure rotational RS. It arises from the fact that the cross section is defined in terms of the scattered power per unit of incident power.[21] The population density N_J in molecules/cm^3 is given by

$$N_J = Ng_J \, (2J + 1) \, \exp[-(hc/k)E_J/T]/Q_r, \qquad (2)$$

where N is the average molecular concentration in cm^{-3} during the read interval, g_J and $2J + 1$ are respectively the nuclear spin and the rotational degeneracy factors, E_J is the energy separation in cm^{-1} of the J level from the ground state (J = 0 level), T is the absolute temperature in Kelvins (K), Q_r is the rotational partition function, and the factor hc/k contains the usual fundamental constants which give 1.4388 K/cm^{-1}. The energy separations of the levels are given by[20]

$$E_J = B_v J(J + 1), \qquad (3)$$

where B_v is the rotational constant which is a weak function of the vibration quantum number v. For $^{14}N_2$, $B_0 = 1.9895$ cm^{-1}.[20,22]

The rotational partition function or state sum can be expressed by

$$O_r = \sum_{J=0}^{\infty} g_J (2J + 1) \exp[-(hc/k) B_0 J(J + 1)/T]. \quad (4)$$

The nuclear spin degeneracy g_J depends on the nuclear spin I of the molecule. For integral I, as for N_2 in which $I = 1$, g_J is equal to $(2I + 1)(I + 1)$ and $(2I + 1)I$ respectively for symmetric and antisymmetric rotational levels.[20] Even J states in N_2 are symmetric while odd J states are antisymmetric. This gives $g_J = 6$ or 3, which increases the signals obtained from the even J lines calculated via Eqs. (1) and (2) by a factor of two over the odd J lines. This fact means that generally the even J lines are preferred for measurements on the N_2 spectrum. Since $(hc/k)B_0/T \ll 1$ in Eq. (4) for N_2 with $T > 300$ K, the summation can be replaced by an integral,[20] which gives

$$O_r \approx (2I + 1)^2 T/(2B_0 hc/k). \quad (5)$$

In addition to the T^{-1} dependence introduced by Eq. (5) into the observed count rate $\dot{n}_J$, there is a T^{-1} contribution from N via the kinetic theory (i.e., the gas law) given by the

$$N = p/kT \text{ in } m^{-3}, \quad (6)$$

9

where here p is the partial pressure of N_2 in Newtons/m^2 and k is the Boltzmann constant which is equal to 1.3806 x 10^{-23} J/K. The resulting T^{-2} factor, which is in contrast to the $\sim T^{-1}$ factor that is in the vibrational Raman expression due to Eq. (6), makes a significant contribution to the ultimate limit on the upper temperature that can be usefully measured under constant pressure using a specific pair of pure rotational Stokes lines.

Equations (4) and (5) are acceptable provided that the population of the excited vibrational levels (i.e., v > 0) are negligible. At T = 1000 K, only about 3.5% of the N_2 concentration is associated with the first excited vibrational level (v = 1). However, at 2000 K this fraction increases to about 19%. The situation is further complicated by the fact that the pure rotational transitions from molecules in vibrationally excited states are shifted towards the laser line by an amount given by [20,24]

$$\delta\nu_J = -4(J + 3/2)\alpha_e v \qquad (7)$$

where α_e is the rotation-vibration interaction constant. For N_2, $\alpha_e = 0.0187$ cm^{-1}.[20] The effect of this shift is to displace the center of the observed rotational line away from the room temperature position with increasing temperature by an amount that is different for different J values. For example, the v=1 shifts given by Equation (7) for J = 8 and 11 are respectively -0.71 and -0.94 cm^{-1}. If the spectrometer slit function were rectangular and had a width somewhat larger than the biggest v=1 shift, then the error in using Equation (5) would be less than 3.5% at 2000 K. The error increases as the slit function becomes more triangular for a fixed full width at half maximum (fwhm). For example, an error of 3% (too low) has been reported using a triangular slit width of 2.6 cm^{-1} fwhm.[25]

The scattering cross section σ_J depends on the polarizations of the incident and scattered light. In the scattering geometry used in this work the incident laser beam is plane polarized perpendicular to the plane formed by the laser beam direction and observation direction. The scattered light was collected by the spectrometer without passing through a polarizer or a de-polarizer. However, the spectrometer transmittance depends on both the incident polarization and wavelength. Since the rotational lines used in this work were located within a narrow, 80-cm^{-1} interval and the polarization was fixed, the factors which account for these effects are constant and independent of the J values of interest, and therefore can be neglected for our purposes. Thus, for convenience, we will use the sum of the polarized component (i.e., parallel to the laser polarization) and the depolarized component (i.e., perpendicular to the laser polarization) for the cross section as expressed by[23]

$$\sigma_J = \frac{56\pi}{15} \frac{(J+1)(J+2)}{(2J+1)(2J+3)} \, \nu_J^4 \, \gamma^2 , \qquad (8)$$

where γ is the anisotropy of the molecular-polarizability tensor in cm^3. The value of γ^2 for N_2 excited by 488 nm laser light is $0.518 \pm 8\% \times 10^{-48}$cm^6.[16] The scattered frequency ν_J is reasonably approximated by[20]

$$\nu_J = \nu_L - B_0(4J + 6) , \qquad (9)$$

where ν_L is the laser frequency in cm^{-1} (i.e., the inverse of the laser wavelength).

2.2 TEMPERATURE AND CONCENTRATION EQUATIONS

In order to determine temperature from the measured count rates of two rotational lines, let the J values of these two channels be given by J_A and J_B where the B channel is taken as closest to the laser line. For ease of expression, we shall replace the subscript J by A or B from here on, as appropriate. The ratio of the observed Raman counts accumulated during an accurately known read time interval Δt is obtained from Eq. (1) as

$$R_O = \frac{n_A}{n_B} = \frac{\dot{n}_A \Delta t}{\dot{n}_B \Delta t} = \frac{\varepsilon_A \sigma_A N_A}{\varepsilon_B \sigma_B N_B} . \tag{10}$$

The system efficiency factors are in general different since two different detectors are used. Using Eq. (2), the ratio in Eq. (10) can be expressed as

$$R_O = R_\varepsilon (C_A/C_B) \exp \left[(K_B - K_A)/T \right] , \tag{11}$$

where $R_\varepsilon = \varepsilon_A/\varepsilon_B$ is the responsivity or detection gain of channel A relative to channel B, and

$$C_A = g_A N B_0 \sigma_A (2J_A + 1)/(2I + 1)^2 . \tag{12}$$

From Eq. (3)

$$K_A = 1.4388 \, B_0 J_A (J_A + 1) . \tag{13}$$

12

The equations for C_B and K_B are the same as Eqs. (12) and (13) with A replaced by B. From Eq. (11), the temperature equation can be written as

$$T = K_1/\ln(K_2 R) \qquad (14)$$

where

$$R = R_O/R_\varepsilon \qquad (15)$$

and

$$K_1 = K_B - K_A$$
$$\qquad (16)$$
$$K_2 = C_B/C_A$$

The ratio R_ε is effectively a gain factor which must be experimentally determined. It provides an adjustable parameter for calibration purposes. Note that the factor in Eq. (8) involving the fourth power of the scattered frequency is practically unchanged when going from channel A to channel B, thereby making the ratio of these factors in C_B/C_A essentially unity.

Values of the constants in Equation (14) for cases of interest in this report are given in Table 1.

13

TABLE 1
Constants for the Temperature Equation Using Two Rotational
Raman Lines of N_2

J_A/J_B	K_1 (K)	K_2
7/4	−103.05	1.2879
9/6[a]	−137.40	1.4255
11/8	−171.75	1.5182
14/10	−286.25	0.74130

[a]These lines are overlapped by O_2 lines. See text.

The plots of the calibration curves using Equation (14) and the values in Table 1 are given in Figure 1. Except for the last case, the portion of the observed Stokes rotational Raman spectrum of air applicable to Table 1 is given in Figure 2.

As can be seen in Figure 2, the case of $J_A/J_B = 9/6$ involves the accidental overlap or mixing of the $J = 9$ and 13 lines of O_2 respectively with the $J = 6$ and 9 lines of N_2. The resultant "mixed" lines are the strongest in the Raman spectrum of air which makes them very attractive for measurements when the O_2 and N_2 concentration ratio is constant and the behavior of the two molecules is indistinguishable. This would be the case, for example, in noncombustion, subsonic flows. The lines are not perfectly overlapping. In channel A, the $J = 9$ N_2 line is shifted 84.03 cm^{-1} from the laser line while the $J = 13$ O_2 line is at 83.39 cm^{-1}. In channel B, the $J = 6$ N_2 line and the $J = 9$ O_2 line are respectively at 60.02 and 60.39 cm^{-1}.

14
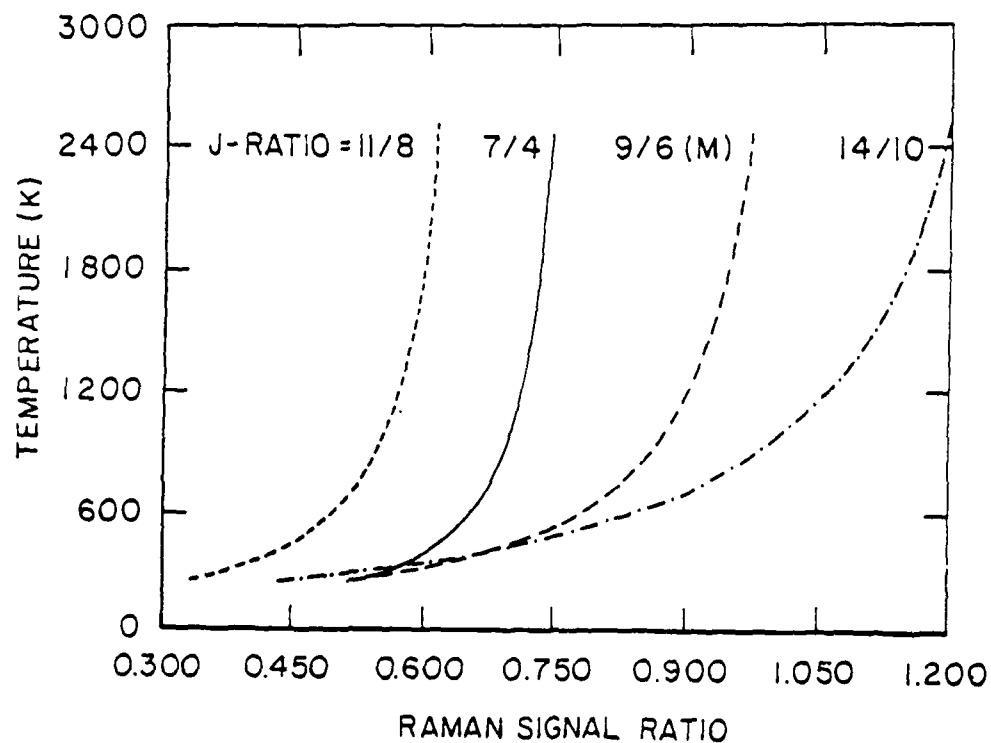
Figure 1.   Theoretical Temperature Calibration Curves for Four
Pairs of Stokes Rotational Raman Lines of N_2.   [The
9/6(M) pair includes the J = 13 and 9 lines of O_2.]

15
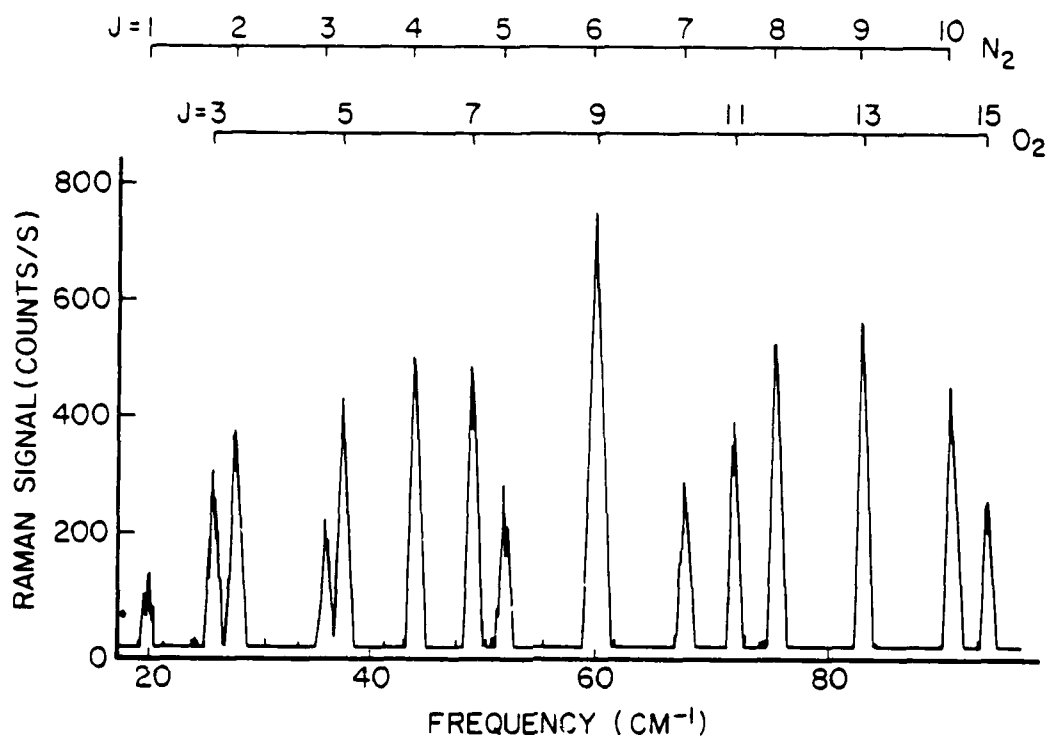
Figure 2.   A Typical Stokes Rotational Raman Spectrum of Room
Air for a Single Pass of a 2-W, 488-nm Laser Beam.
(Bandwidth was about 0.8 cm⁻¹.)

16

In order to use the mixed lines for temperature measurements, it is necessary that the channel or slit widths be wide enough to completely encompass the lines from both species.[13] If this is the case, the relationship between the temperature and the ratio of the mixed lines R_m can be found by referring to Equation (10) which now becomes

$$R_m = \frac{n_A' + n_A''}{n_B' + n_B''} = R_o' \left[\frac{1 + n_A''/n_A'}{1 + n_B''/n_B'} \right] = R_o' \xi \tag{17}$$

where the single and double primes denote respectively N_2 and O_2. The quantity in the brackets represented by ξ can be calculated using Equations (12) and (13),

$$\xi = \frac{1 + (C_A''/C_A') \exp[-(K_A''-K_A')/T]}{1 + (C_B''/C_B') \exp[-(K_B''-K_B')/T]} \quad . \tag{18}$$

The constants needed to calculate Equations (12) and (13) for O_2 are $\gamma^2 = 1.35 \times 10^{-48}$ cm^6,[16] $B_0 = 1.4377$ cm^{-1},[20,22] and $g_A = g_B = 1$ for $I =$ zero.[20] The factor ξ is a weak monotonically decreasing function of temperature. Its values at 300 and 1500 K respectively are 0.76909 and 0.68724. An expression relating temperature to R_m was determined by fitting the quotient of two polynomials in R_m to a table of values of R_m and T numerically

generated from Equations (11), (17), and (13). The resulting equation is given by

$$T = (aR_m^2 - bR_m - e)/(R_m - d), \qquad (19)$$

where $a = 28.94$, $b = 153.04$, $e = 63.94$, $d = 1.052442$, and T is in Kelvins. This equation is accurate to within $\pm$ 0.13% over the range of 250 to 2500 K. Thus, the curve given in Figure 1 for the "9/6" case is a plot of Equation (19).

The dependence of the species concentration N on the observed Raman signal $\dot{n}_J$ can be derived from Equations (1), (2), and (5). We replace ε in Equation (1) by ε' which now includes all the constants that appear in the expression relating $n_J = \dot{n}_J \Delta t$ to N. Thus, we obtain

$$N = n_J \left\{ \frac{\lambda_J^3 \lambda_L T f_r}{\varepsilon' P_e \ell} \exp \left[(hc/k) E_J/T \right] \right\}, \qquad (20)$$

where $\lambda_J = \nu_J^{-1}$ (see Eq. 9), $\lambda_L = \nu_L^{-1}$, $f_r = (\Delta t)^{-1}$, and E_J is given by Equation (3). The utility of Equation (20) in variable-temperature measurements, such as in flames, is that it permits the calibration to be independent of the various measurement parameters such as the read rate f_r. It should be noted that the units of the pre-exponential factors can be chosen for convenience since the value of the calibration constant ε' is arbitrary.

18

A more convenient quantity to compute in concentration measurements than N is the mole fraction c where, using Equation (6), we have

$$c \equiv N/N_r = N \, k \, T/p \quad , \qquad (21)$$

with p now the total pressure of the gaseous mixture. The reference concentration N_r can be given or it can be computed as shown in Equation (21) for subsonic, constant-pressure flows. In constant-temperature measurements with the measurement parameters held constant, the quantity in the braces in Equation (20) is constant. Equation (21) can now be expressed as

$$c = n_J/\overline{n}_{Jr} \quad , \qquad (22)$$

where $\overline{n}_{Jr}$ is the mean counts per read for the line specified by J that corresponds to 100% concentration of the measured gas.

2.3 POISSON UNCERTAINTY EQUATIONS

Since photon-counting measurements follow Poisson statistics, it is possible to arrive at expressions which give the precision uncertainties in measurements of temperature and/or species concentration. Of course, the accuracy uncertainty depends not only on the precision of the measurement but also on the calibration procedure and the calibration standard. The primary goal here is to be able to predict the precision of a measurement given the signal levels and the measurement parameters.

The measured count rate $\dot{M}$ in general is the sum of the Raman count rate $\dot{\Lambda}$, the laser-induced background count rate $\dot{b}$[2],

the nonlaser-induced background count rate $\dot{b}^{(n\ell)}$, and the detector dark count rate $\dot{d}$. We assume that in any particular measurement circumstance these four quantities are statistically stationary random variables. Thus, if the sum of the two background signals is given by

$$\dot{b} = \dot{b}^{(\ell)} + \dot{b}^{(n\ell)} \tag{23}$$

for each channel, then the Raman count rate is given by

$$\dot{n} = \dot{M} - (\dot{b} + \dot{d}) \ . \tag{24}$$

In a multichannel system, however, Equation (24) does not adequately deal with the problem of calibration of the responsivity ε of a given channel [see Equation (1)]. Either the responsivities of the channels can be made equal, or correction factors can be determined by calibration against a reference light level. We chose the latter approach, since it permits the system response determining parameters to be held constant.

The total photoelectron count rate $\dot{n} + \dot{b}$ is the quantity affected by the channel detection efficiency ε. A reference photon count rate $[(\dot{n} + \dot{b})/\varepsilon]_r$ can be used to effectively modify or "correct" the channel responsivity to produce a particular photoelectron count rate for a given total light signal. Thus, using Equation (24) we can write

$$\dot{M} - \dot{d} = \frac{\varepsilon \left[(\dot{n} + \dot{b})/\varepsilon \right]}{\varepsilon_r \left[(\dot{n} + \dot{b})/\varepsilon \right]_r} (\dot{n} + \dot{b})_r \ . \tag{25}$$

20

Since the photon rates in the brackets are made equal in the calibration, we have

$$\dot{M} - \dot{d} = G(\dot{n} + \dot{b}) , \qquad (26)$$

where $G \equiv \varepsilon/\varepsilon_r$ is the channel "gain" factor needed to correct the measured photoelectron count rate $\dot{M} - \dot{d}$ in order to ensure that the resulting Raman photoelectron count rate $\dot{n}$ can be traced to a known responsivity. Thus, the quantities $\dot{n}$ and $\dot{b}$ determined from Equation (26) are now calibrated against the reference responsivity ε_r. For temperature measurements, we will choose the B-channel responsivity to be the reference, namely $\varepsilon_r = \varepsilon_B$.

It is now convenient to define the corrected "total" background signal $\dot{b}'$ as

$$\dot{b}' = G\dot{b} + \dot{d} . \qquad (27)$$

Then Equation (25) can be written

$$\dot{n} = (\dot{M} - \dot{b}')/G . \qquad (28)$$

It is common to measure the total background at a lower read rate f_b than the intended measurement read rate f_r. This has an impact on Equation (28) written in the count-per-read form; namely

$$n = (M - b' f_b/f_r)/G . \qquad (29)$$

21

Thus, using this equation with Equations (10) and (15), we obtain the "true" ratio of the Raman signals in the two channels to be

$$R = \left[\frac{M_A - b_A' f_b/f_r}{M_B - b' f_b/f_r} \right] \frac{1}{R_\epsilon} \quad , \tag{30}$$

where

$$R_\epsilon = G_A/G_B = \epsilon_A/\epsilon_B \tag{31}$$

We note that R_ϵ is the gain of channel A relative to the gain of channel B. Equations (29) and (30) apply respectively to concentration and temperature measurements. It is assumed here that the total background counts b_A' and b_B' on a per-read basis can be obtained respectively when $n_A = n_B = 0$ from the actual observed counts as given by Equation (29) for $f_r = f_b$. These measurements are independent of the Raman measurements. Thus, the M and b' quantities in Equations (29) and (30) are the actual numbers of counts observed. Generally, this approach is most satisfactory when $\dot{b}' << \dot{n}$. The detailed procedures for arriving at suitable values for $\dot{b}_A'$ and $\dot{b}_B'$ are discussed in Section 4.

The uncertainties in the temperature and concentration result from the propagation of the uncertainties in the various quantities in Equations (14), (20), (29), and (30). This propagation is relatively straightforward provided that the various uncertainties are not too large (say $\leq 30\%$) or the quantities are normally distributed, and where the quantities are uncorrelated.[26] The basic properties of a Poisson-distributed variable are that the expectation value of the variable and its variance both equal the mean of the distribution. These are

22

respectively the first moment about the origin and the second central moment of the distribution. Thus, the standard deviations s_M and s_b in the observed counts per read for M and b' are respectively $\sqrt{\bar{M}}$ and $\sqrt{\bar{b}'}$.

The fractional (or relative) uncertainty in a single measurement of temperature using Equation (14) is given by

$$s_T/\bar{T} \approx \left\{ (s_1/K_1)^2 + \left[(s_2/K_2)^2 + (s_R/\bar{R})^2 \right] (\bar{T}/K_1)^2 \right\}^{1/2} , \qquad (32)$$

where s_T, s_1, s_2 and s_R are respectively the standard deviations in T, K_1, K_2 and R. Since K_1 and K_2 are fixed values in any series of measurements, their uncertainties affect the accuracy of the measurements while s_R characterizes the precision of each measurement. Thus, the uncertainty in the measured temperature of primary interest becomes, from Equation (32),

$$s_T \approx (s_R/\bar{R})\bar{T}^2/\mid K_1 \mid . \qquad (33)$$

In the calculations of $s_R/\bar{R}$ it was assumed that the read rates f_r and f_b and the gain ratio R_c in Equation (30) are constants in any given measurement and that any uncertainties in these quantities impact the accuracy rather than the precision of the measurement. Actually, the read frequency was determined by a crystal-controlled oscillator to 1 ppm and the gain ratio was measured to better than 0.1%. In the derivation, we make liberal

23

use of Equation (29) while referencing all signal levels to channel B. Thus, after considerable manipulation, we obtain

$$\left(\frac{s_R}{\overline{R}}\right)^2 \approx \frac{1}{\overline{M}_B(1 - \overline{b}'_{BB})} \left[\frac{1}{R_e\overline{R}}\left(1 + \frac{R_b R_f \overline{b}'_{BB}}{R_\varepsilon \overline{R}(1 - \overline{b}'_{BB})}\right)\right.$$

$$\left. + \frac{R_f \overline{b}'_{BB}}{1 - \overline{b}'_{BB}} + 1\right], \tag{34}$$

where

$$\left.\begin{array}{l} \overline{b}'_{BB} \equiv \overline{b}'_B \ (f_b/f_r)/\overline{M}_B \\ \\ \text{or} \\ \\ \qquad = \overline{b}'_B/\overline{M}_B \end{array}\right\} \tag{35}$$

and

$$R_b \equiv \overline{b}'_A/\overline{b}'_B \tag{36}$$

$$R_f \equiv 1 + (f_b/f_r) \ . \tag{37}$$

24

We note that in the limit of $\bar{\delta}_B' = \bar{\delta}_A' = 0$,[13]

$$s_R/\bar{R} \approx \sqrt{f_r[(1/\bar{\dot{n}}_A) + (1/\bar{\dot{n}}_B)]} \quad , \tag{38}$$

which clearly shows the desirability of having high Raman count rates when a high read rate is used.

Evaluations of Equation (33) using Equation (34) are conveniently accomplished by calculating $s_T \sqrt{\bar{M}_B} = s_T \sqrt{\bar{\dot{M}}_B/f_r}$. Figures 3 and 4 show plots of this quantity as a function of temperature respectively for equal backgrounds, namely $R_b = 1$, and for $R_b = 0.5$ using the $J_A = 11$ and $J_B = 8$ lines of N_2. The plots show a range of background levels from $\bar{\delta}_{BB}' = 0$ to 0.5. The read rate factor R_f was 1.0 in these plots which is easily accomplished in practice. For example, in Figure 3, for $\bar{\delta}_{BB}' = 0.5$ at 2500 K, s_T increases only 4% for $R_f = 1.1$. The impact of choosing a wider-spaced pair of lines can be seen in Figure 5 where the calculation of Figure 3 was repeated using $J_A = 14$ and $J_B = 10$. Comparing these two figures shows that the temperature uncertainty is reduced by approximately a factor of two in Figure 5 compared to Figure 3. This means that for a given uncertainty, the 14/10 pair will permit a measurement at about twice the temperature permitted for the 11/8 pair.

The uncertainty in variable-temperature concentration measurements for constant-pressure subsonic flows can be obtained from Equations (20) and (21) by substituting Equation
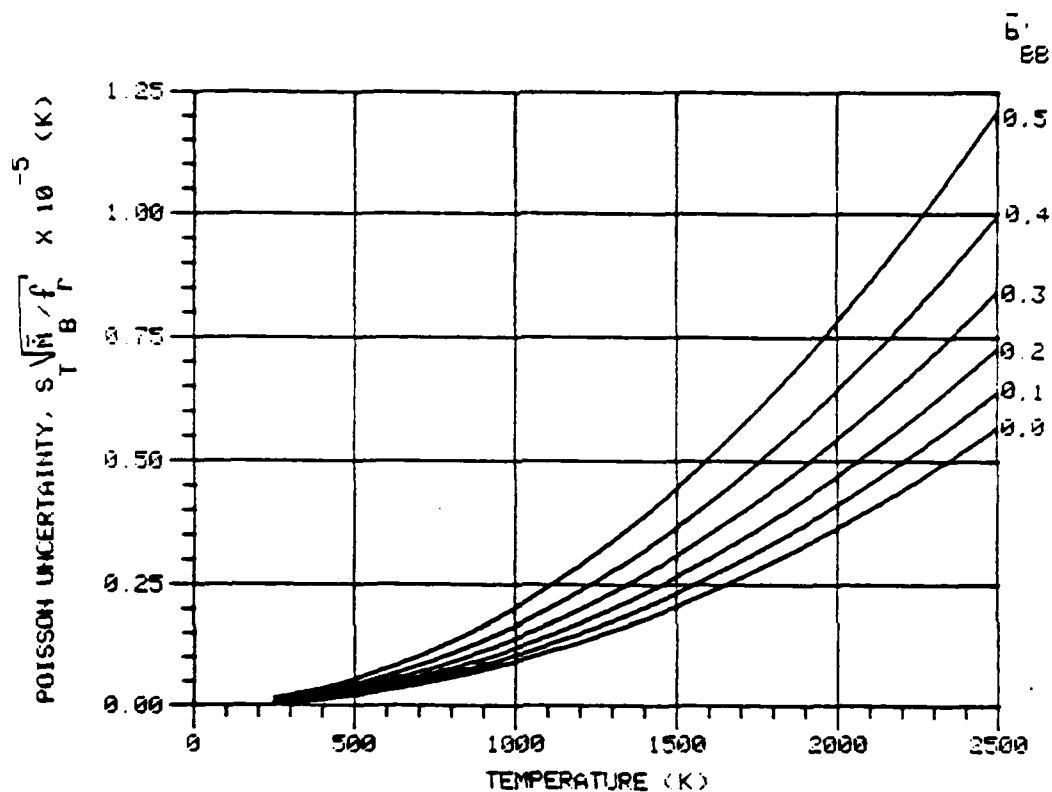
Figure 3. The Temperature Poisson Uncertainty s_T for the J_A/J_B Ratio of 11/8 of N_2 for an A/B Background Ratio of 1.0. [The curves are for channel-B background-to-total signal ratio $\bar{b}'_{BB}$ of 0.0 to 0.5. See Equations (33) through (37).]

26
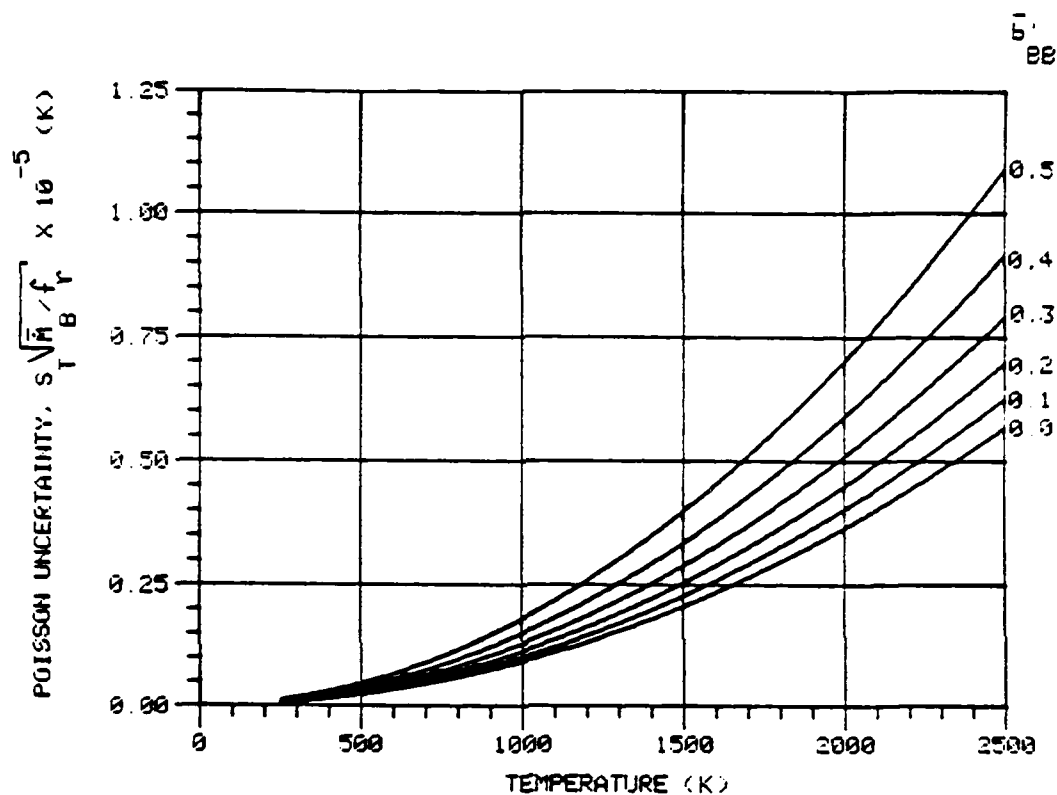
Figure 4.   The Temperature Poisson Uncertainty s_T for the J_A/J_B
             Ratio of 11/8 of N_2 for an A/B Background Ratio of
             0.5.   [The curves are for channel-B background-to-
             total signal ratio $\bar{b}'_{BB}$ of 0.0 to 0.5.   See Equations
             (33) through (37).]

POISSON UNCERTAINTY, $s_T \sqrt{\bar{M}_B / f_r}$ (K)

TEMPERATURE (K)

$\bar{b}'_{BB}$

0.5
0.4
0.3
0.2
0.1
0.0
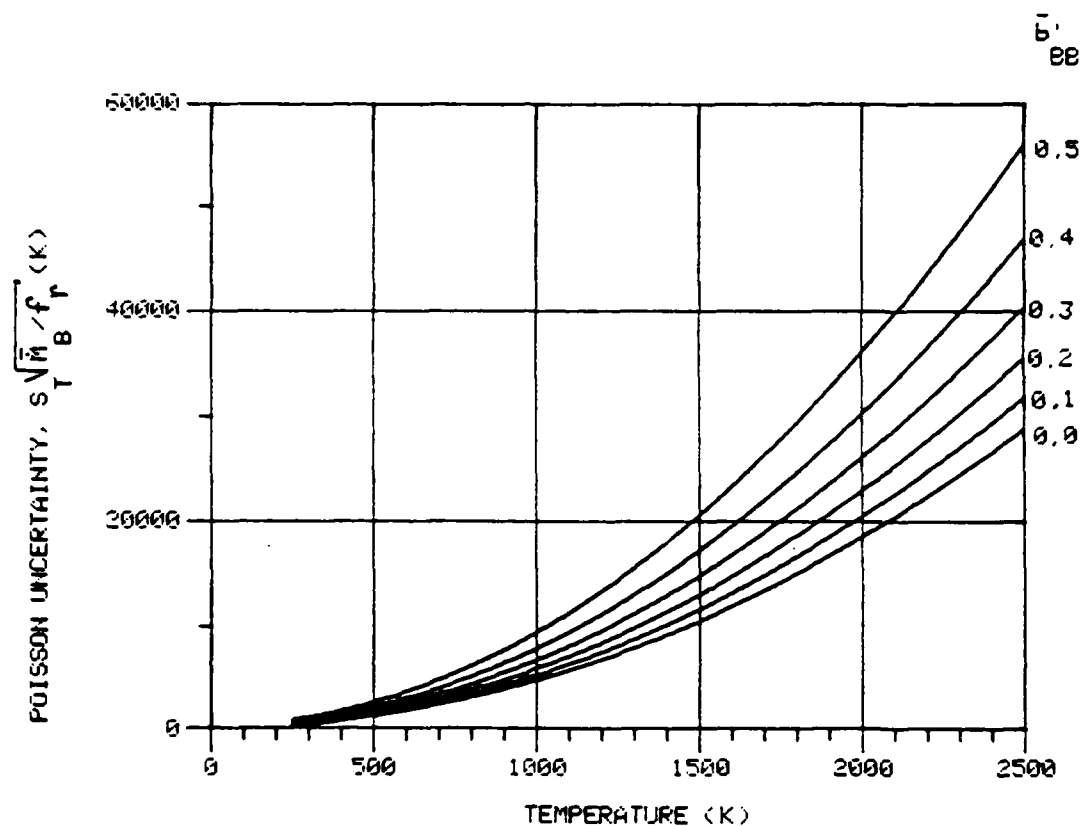
Figure 5.   The Temperature Poisson Uncertainty s_T for the J_A/J_B
Ratio of 14/10 of N_2 for an A/B Background Ratio of
1.0.   [The curves are for channel-B background-to-
total signal ratio $\bar{b}'_{BB}$ of 0.0 to 0.5.   See Equations
(33) through (37).]

28

(14). Assuming the concentration is measured in channel B and the uncertainty in the mole fraction c_B is s_{cB}, we obtain

$$\left(\frac{s_{cB}}{\bar{c}_B}\right)^2 \approx \frac{1}{\bar{M}_B(1 - \bar{b}'_{BB})}\left(\frac{R_f\bar{b}'_{BB}}{1 - \bar{b}'_{BB}} + 1\right) + \left(\frac{K_B}{\bar{T}} - 2\right)^2\left(\frac{s_T}{\bar{T}}\right)^2 \quad (39)$$

where $s_T/\bar{T}$ is obtained from Equations (33) and (34). The impact of Equation (39) is that the percent uncertainty in a concentration measurement in a variable-temperature may be near zero or as high as twice the percent uncertainty in temperature, depending on the value of $K_B/\bar{T}$. This suggests that the choice of J_B, which determines the value of K_B, is an important decision if optimum simultaneous measurements of temperature and concentration are to be made. In constant-temperature measurements the second term in Equation (39) propagates the accuracy uncertainty in the given temperature value, while the first term is all that is needed to calculate the precision uncertainty associated with Equation (22).

The precision uncertainty in the temperature determined using the mixed lines discussed in association with Equations (17) and (18) is given by $s_{Tm} \approx |\partial T/\partial R_m| s_R$ where the derivative (evaluated at $\bar{R}_m$) is most easily obtained from a numerical evaluation of Equation (19) and s_R is given by Equation (34).

29

SECTION 3
SYSTEM DESIGN AND PERFORMANCE

In this section are descriptions of the optical subsystems, electronics, and software. The impact of the basic objectives of the work on the system design is discussed, and the performance characteristics of the various subsystems as well as the overall TiLaRS system are presented. Many details concerning the design, adjustment, and operation of the TiLaRS system, including computer program listings, are contained in the Operations Manual.[27]

3.1 DESIGN OBJECTIVES

The TiLaRS system was designed to measure simultaneously the intensities of two pure Stokes rotational Raman lines. The two-channel capability was obtained by selecting two wavelength regions in the exit slit plane of the spectrometer using a specially designed crossed-axis cylindrical lens system and a pair of custom-fabricated slit mirrors.[18] High sampling or "read" rates were accomplished by parallel data transfer to high-speed parallel input ports of a dedicated minicomputer.

The TiLaRS system has two measurement capabilities: (a) to measure the dynamic temperature of a diatomic probe gas, typically N_2, and the probe gas concentration simultaneously in gas flows or flames, and (b) to measure the dynamic concentration of two molecular species simultaneously in constant temperature (i.e., in "cold" or noncombusting) gas flows. In the latter case, the species of primary interest were N_2, O_2, and CO_2. The essential requirement for the data to have a reasonable degree of accuracy in any measurement is that the background signals be steady and have fluctuations that are small compared to the fluctuations in the Raman signals. This is accomplished most

conveniently when the background signals are weak compared to the Raman signals.

It should be noted that although the system was intended to be used with pure rotational Raman lines, it can also measure concentration and temperature using the first hot band and the ground-state band of the Q-branch of the Stokes vibrational-rotational Raman spectrum of N_2.[1,5] Because of the weak intensity of the hot band, this possibility was not pursued.

Since high read rates require high Raman signal levels, the available laser power in the observed volume was increased by passing the laser beam through an optical multipass cell. In addition, a reverse optics mirror was used to nearly double the collected light. These features, plus the use of a high-power cw argon ion laser and selected high-quantum-efficiency PMT's, provided the highest Raman signals possible using the available spectrometer.

3.2 SYSTEM OVERVIEW

A complete block diagram of the TiLaRS system as presently configured is shown in Figure 6. The laser tube is water cooled using a closed-loop heat exchanger system. The laser is equipped with a power meter which can be used to maintain the output power constant to better than 0.5% via a feedback loop to the laser current control. Although the cavity dumper is mounted and aligned, the laser was normally operated without the dumper, due to the lower power output (-38%) of the cavity-dumped configuration.

The scattered light from the focus of the laser beams in the multipass cell is collected and focused on the entrance slit of the spectrometer. The exit slit optics focuses the two wavelength channels onto the photocathodes of the PMT's which are
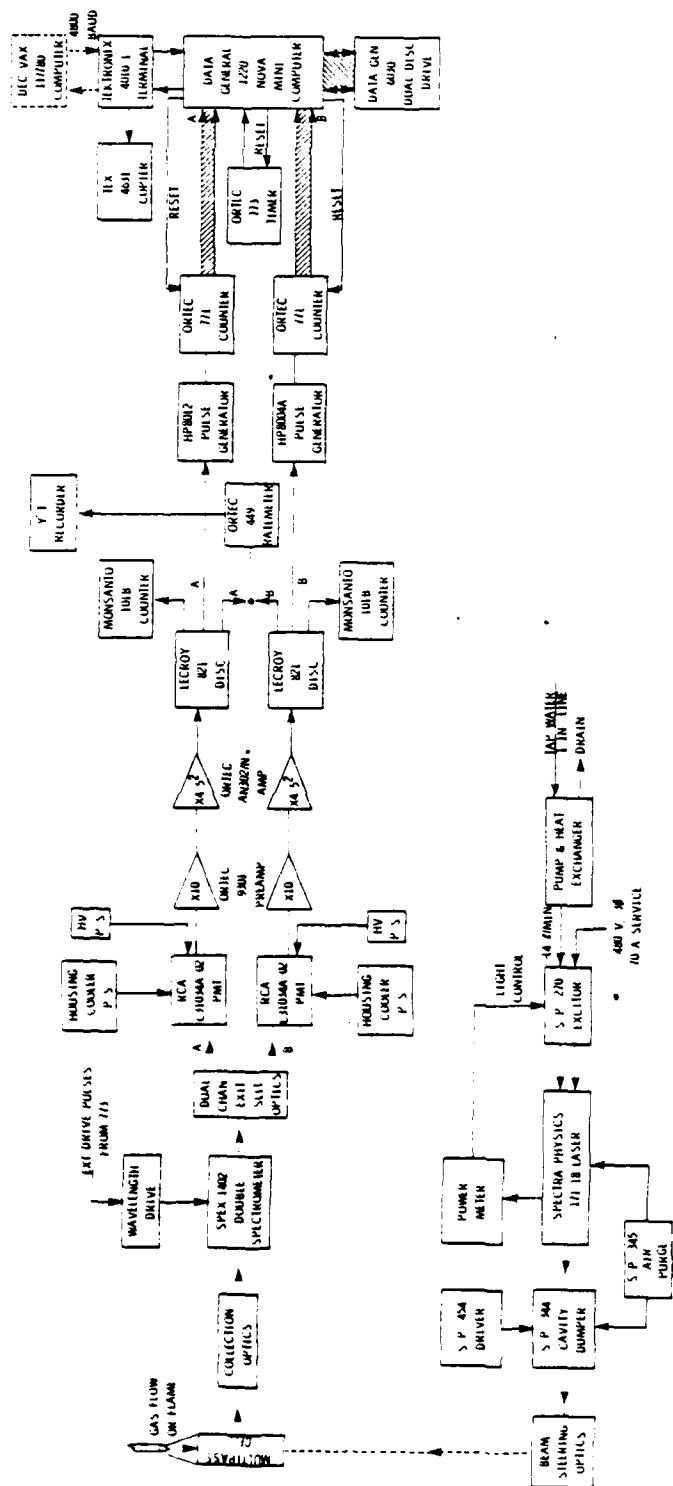
Figure 6. Block Diagram of the Two-Channel TILaRS System.

33

connected for photon counting. The PMT pulses are amplified and sent to discriminators which produce fast NIM pulses of adjustable width. Each discriminator has several outputs. One is used to drive a digital frequency counter to permit monitoring the count rate of that channel. Another can be used to drive an analog rate meter to provide a signal for recording the spectrum with a recorder. A third output has its levels translated to TTL levels via a pulse generator to permit driving the main counter. The two main counters are equipped with parallel data buffers connected to two parallel input ports of the minicomputer's interface board. The 16-bit minicomputer has a 32-kword (or 64-kbyte) memory.

The timing for each read is provided by a crystal-controlled timer modified to give a time interval multiplier of 0.01 ms. This timer produces an interrupt pulse at the end of each interval. The computer then reads the contents of the counter buffers and resets the counters and the timer. The next read interval begins as soon as the reset pulse goes low. The operating system and the data recording are provided through an eight-inch, dual floppy disk drive. Computer control is accomplished via a Tektronix terminal and companion hard-copy unit. Control can be transferred to the UDRI Digital Equipment Corporation (DEC) VAX 11/780 computer via a 4800-baud hard-wire line or to a W-PAFB computer via an acoustic coupler and the telephone line.

3.2.1 Optical Subsystems

The TiLaRS optics are conveniently organized into five subsystems: the laser and cavity dumper, the laser beam steering optics, the multipass cell for the laser beam, the collection optics for the scattered light, and the spectrometer with the two-channel exit-slit optics. A diagram showing the assembly of these subsystems is given in Figure 7. A photograph of the

34
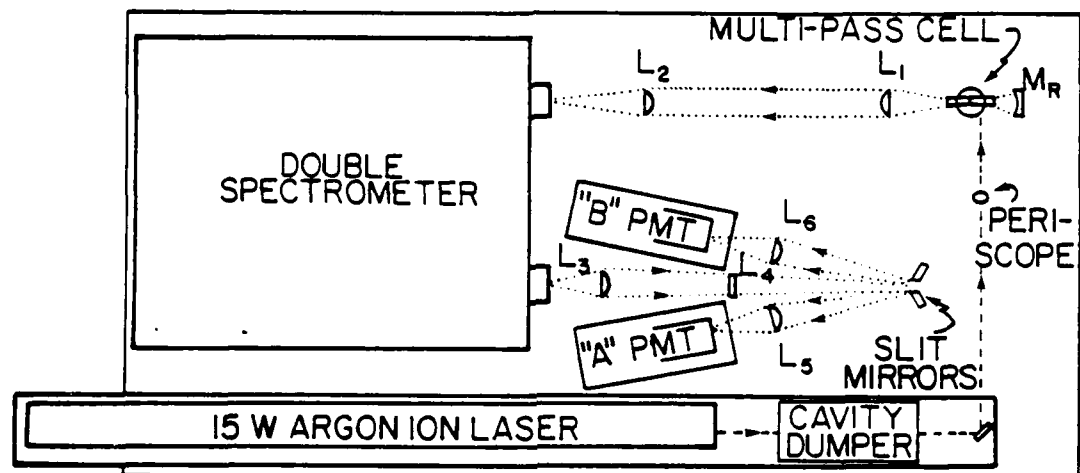
Figure 7.   Layout of the Two-Channel TiLaRS System.

TiLaRS system is shown in Figure 8. In the following paragraphs, the designs for each subsystem are described.

A Spectra-Physics model 171-18 argon ion laser was used to provide up to 6 W cw (in the "donut" mode) at 488 nm. This wavelength was chosen because it is the strongest blue line available from the laser. A blue line was chosen because it was experimentally observed that a portion of the C_2 spectrum (Swan band) of a simple methane flame coincides with the Stokes pure rotational region of the strong green line at 514.5 nm. This interference makes the green line unsuitable for rotational Raman studies in flames.

The stability of the laser power was important in these studies because there was no provision to record the laser power during the runs. This concern was resolved by using the light-control feature of the laser. The power meter built into the laser provides the feedback signal for the light-control circuit. The manufacturer specifies the rms noise level and the stability to be 0.5% using the light-control function. The actual performance exceeded these specifications, at least for the measurements carried out to date.

The Spectra-Physics model 344 cavity dumper was obtained to permit pulsed operation. With the pulse width adjusted to about 10 ns fwhm and a base width of nearly 30 ns, a maximum of 2.3 W was obtained with the "4 MHz" pulse repetition frequency (prf) provided by the model 454 driver. The output power is roughly proportional to the prf. The value of using a pulsed laser relative to a cw laser is the possibility of using gated detection which can reduce the background signal relative to the Raman signal.[28] The nonlaser-induced background signal in a gated detection system is multiplied by the gate duty cycle, whereas the laser-induced background signal depends on both the duty cycle and the gate pulse width (i.e., assuming the gate
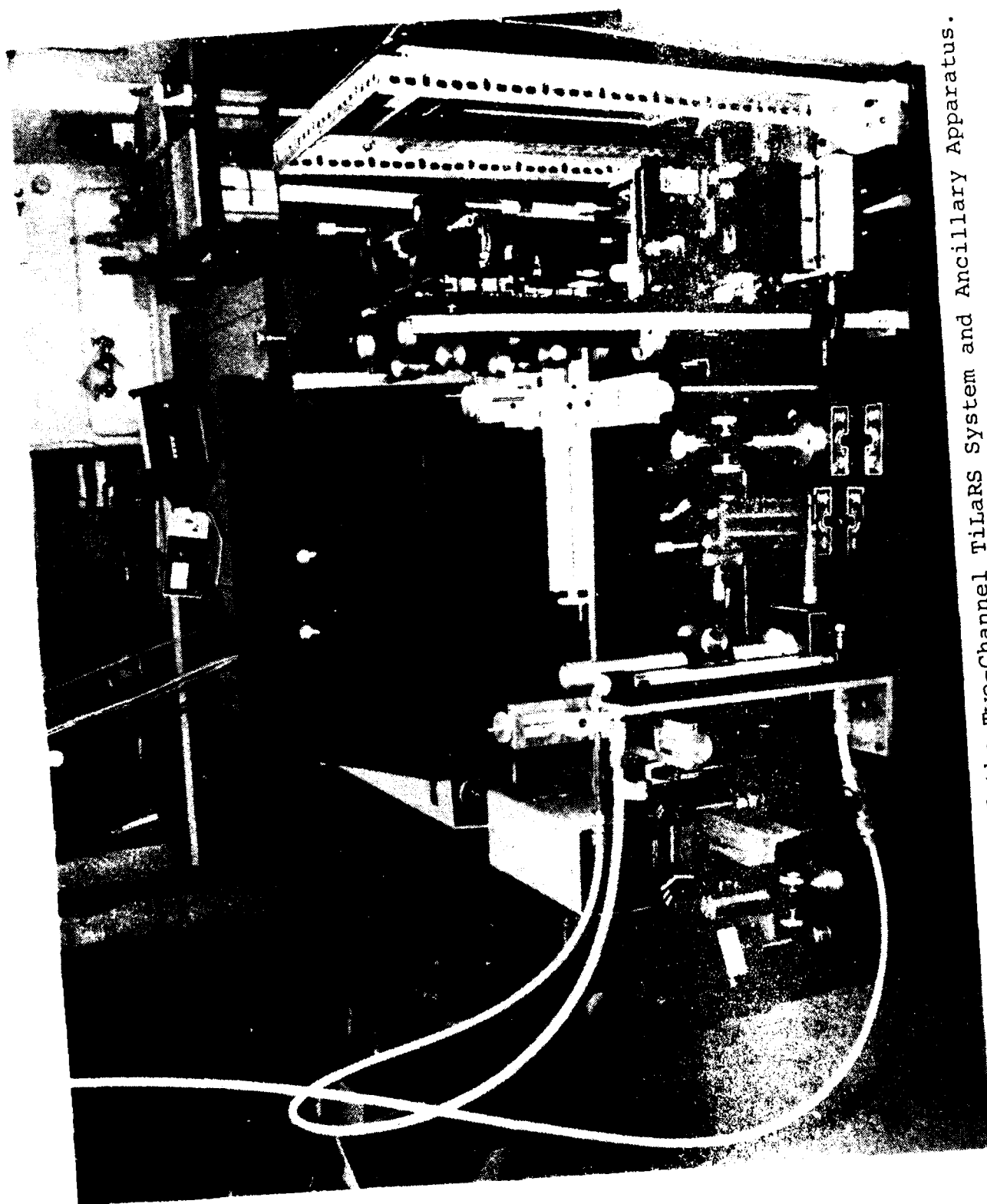
Figure 8. Photograph of the Two-Channel TiLaRS System and Ancillary Apparatus.

pulse is wider than the laser pulse). The gate duty cycle is the gate width multiplied by the laser (and gate) prf. The gate must be wide enough to minimize the loss of Raman signal when the gate is applied. Generally, this requires a gate width equal to the sum of the base width of the laser pulse and the effective turn-on and turn-off times of the gate circuit. This means for a triangle pulse width of 7.5 ns (smallest obtainable), a gate width of at least 20 ns is needed. This gives a gate duty cycle of 0.08 for a prf of 4 MHz which, with the 20-ns gate width provides only moderate discrimination against laser-induced fluorescence background signals that have a decay time constant which falls between about 50 and 150 ns.[28] This rather limited discrimination capability, due largely to the high prf and the significant reduction in the available average beam power when using the cavity dumper, prevented the pulsed mode from being useful in the studies reported here.

The laser beam is steered to the multipass cell by means of a right-angle reflecting mirror, a vertically displacing periscope, and a small mirror at the base of the multipass cell. The right-angle reflecting mirror and the periscope are located as shown in Figure 7. The small mirror used to insert the laser beam into the multipass cell is identified as M_{C1} in Figure 9. The orientations of the first mirror and the periscope mirrors are set to direct the beam parallel to the optical table and perpendicular to the plane of the multiple passes of the laser beam in the multipass cell. The performance of the multipass cell is extremely sensitive to the tilt adjustments of all four mirrors. An iris diaphragm positioned immediately following the first mirror provides some coarse spatial filtering and reduces the laser light feedback into the laser from the multipass cell.
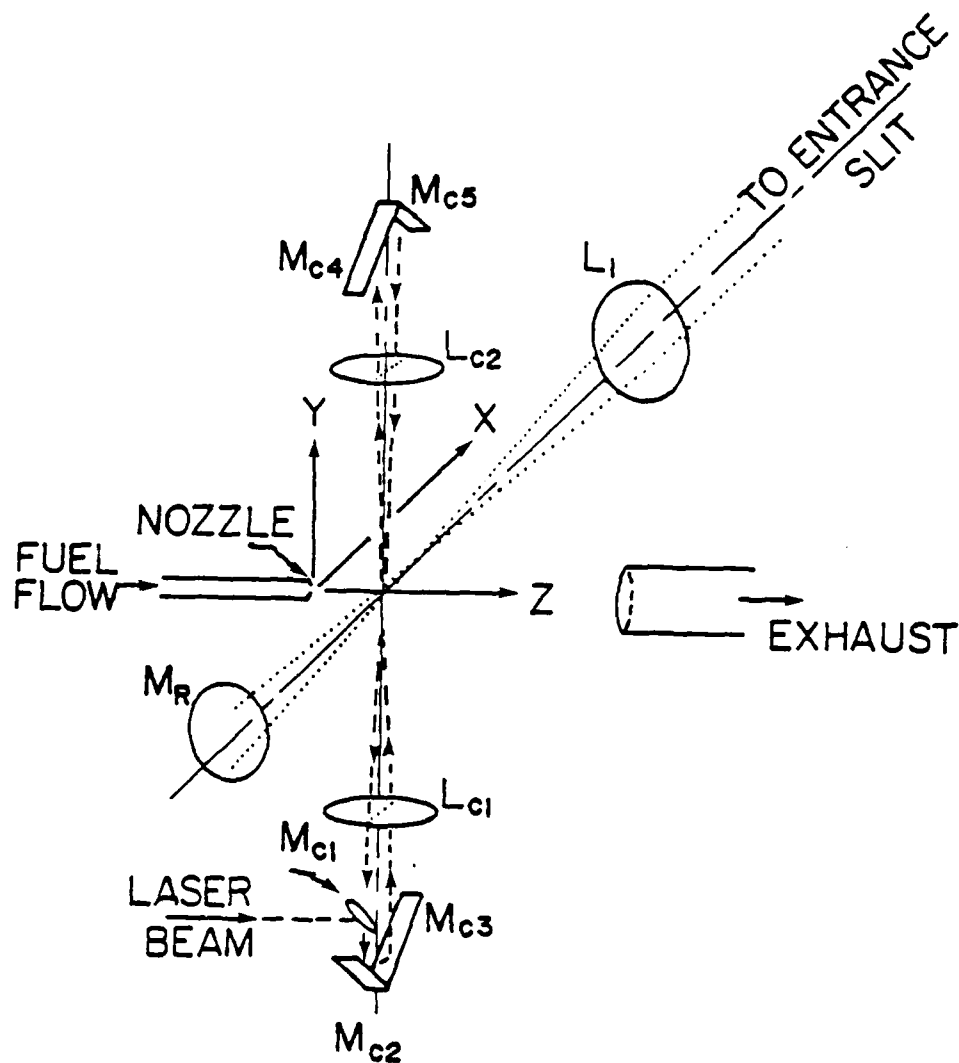
Figure 9.   Schematic Diagram of the Laser Excitation and the
            Raman Collection Geometries Relative to the Gas
            Nozzle.

The layout of the laser beam retroreflecting multipass cell is given in Figure 10. The design is very similar to that described by Hill, Mulac, and Hackett.[29] Its orientation with respect to the gas flow and the spectrometer are shown in Figure 9. This orientation was chosen to optimize the light collected by the spectrometer. This occurs when the aspect ratio of the light source matches the aspect ratio of the spectrometer entrance slit. The lenses L_{C1} and L_{C2} are identical plano-convex, 76-mm diameter lenses made from Dynasil-4000 fused quartz and obtained from Broomer Research Corporation. The material was chosen for its low absorption. The lenses are antireflection coated for <0.1% reflectance at 488 nm for s-polarized light at 0-12° incidence. The effective focal length obtained from the spacing of the lenses in the cell is about 140 mm. The four mirrors M_{C2} through M_{C5} form two planar corner mirror assemblies. The mirrors, also obtained from Broomer Research, are 20 mm wide by 60 mm long by 10 mm thick and are flat to $\lambda/4$ with a scratch and dig number of 60-40. They are multidielectric coated for >99.9% reflectance at 488 nm for s-polarized light at 45° incidence. One mirror of each corner pair has had one 20-mm edge cut so the coating extends to the edge of the mirror. The uncut mirror in each pair is moved past the corner so that the cut mirror can almost touch the reflecting surface of its partner. This arrangement minimizes the losses when the beam straddles the corner.

The alignment of the optical multipass cell is quite tedious, due to the large number of degrees of freedom of the design. The desired performance of the cell is when the beams lie in a plane parallel to the spectrometer entrance slit and produce a tight, "bow-tie" shaped focus centered on the optical axis of the spectrometer. With the undumped laser beam, a gain of 13 over a single pass is obtained when alignment is optimum and the optics are clean. This corresponds to about 13 passes.
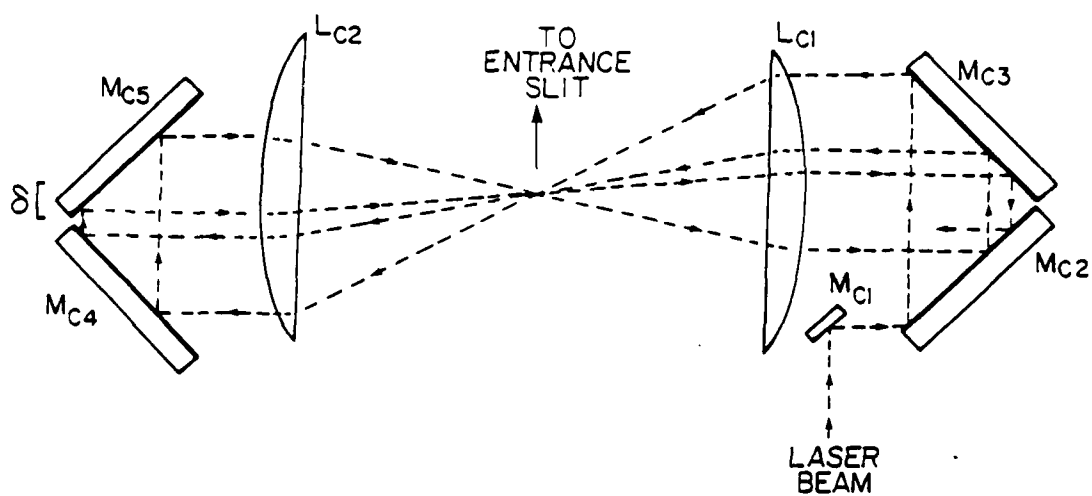
Figure 10. Configuration of the Laser Beam Retroreflecting
Multipass Cell. (The orientation of M_{C1} is rotated
for clarity. See Figure 9 for true orientation.)

The number of passes is determined by the displacement of the beam in each pass. The minimum displacement is restricted to the beam diameter due to the insertion mirror M_{C1} location inside the cell. For example, with the cavity-dumped beam which is smaller than the undumped beam, a gain of 18 was obtained corresponding to about 32 passes.

The laser beam diameter at M_{C1} is 1.54 mm (at e^{-2} points). The calculated diameter of the focused beam at the center of the cell is 40 μm. The corresponding Rayleigh range is 2.6 mm, which gives a waist range of 5.2 mm. The width of the center of the bow tie corresponding to the region of intersection of the beam passes is approximately 0.3 mm. The width increases about 0.2 mm for each millimeter distance from the center due to the outermost passes of the beam. This would correspond to the 2-mm setting of the spectrometer entrance slit height. The volume occupied by the laser beams determined by the projection of this slit height is about 0.04 mm^3. The alignment of the cell on which this performance depends is reasonably stable when the ambient temperature is steady.

The collection optics consists of a lens train and a reverse-optics mirror. The lens train is made up of two identical lenses, L_1 and L_2 in Figures 7 and 9. These planoconvex lenses have a diameter of 102 mm and a focal length of 251 mm. They are positioned for maximum signal and give a magnification of about -0.9 with a collection solid angle of 0.018 ster.[30] The on-axis spot diameter of these lenses is 46 μm. This gives a width of the laser beam image at the entrance slit of about 80 μm, which is consistent with the observed signal reduction with decreasing slit width.

The lens L_2 is fitted with an iris set so that the cone of light entering the spectrometer from the multipass cell just fills the aperture of the spectrometer collecting mirror. This reduces the background signal due to laser light scattered inside the spectrometer. The contribution of ambient light to the background is also reduced by a baffle and an opaque tube mounted on the entrance slit housing. The observed signal is increased by about 90% using the reverse optics mirror M_R shown in Figures 7 and 9. This first-surface spherical mirror is 50 mm in diameter with a 200 mm radius of curvature.

The dispersing instrument used in the TiLaRS system is a wavelength-scanning SPEX 1402 double spectrometer. It is equipped with 1200-g/mm ruled gratings blazed at 500 nm. The instrument is used in second order which gives a measured linear reciprocal dispersion of 0.23 nm/mm at the exit slit for 488 nm light. The maximum width of this slit is 3 mm, which limits the maximum bandwidth to 29 cm^{-1} for this wavelength. To achieve a two-channel capability, a cylindrical lens train was designed which projects the exit-slit image onto two specially fabricated slit mirrors. These mirrors reflect the two spectral channels to their respective PMT's. The layout of these optics is shown in Figure 7 with the detailed design given in Figure 11.

The purpose of the cylindrical lenses in the exit slit optics shown in Figure 11 is to change the aspect ratio of the projected image on the slit mirrors. The lens L_3 magnifies the exit slit width in the horizontal or wavelength dimension by 5.85. The lens L_4 projects the height of the exit slit onto the slit mirrors with essentially unity magnification. Each channel is formed by one edge of the spectrometer slit focused on the channel slit mirror and by the inner sharp edge of that slit mirror. These slit mirrors (supplied by Broomer Research) are 25-mm squares, 6 mm thick with one edge bevelled at 20-25°, as

43
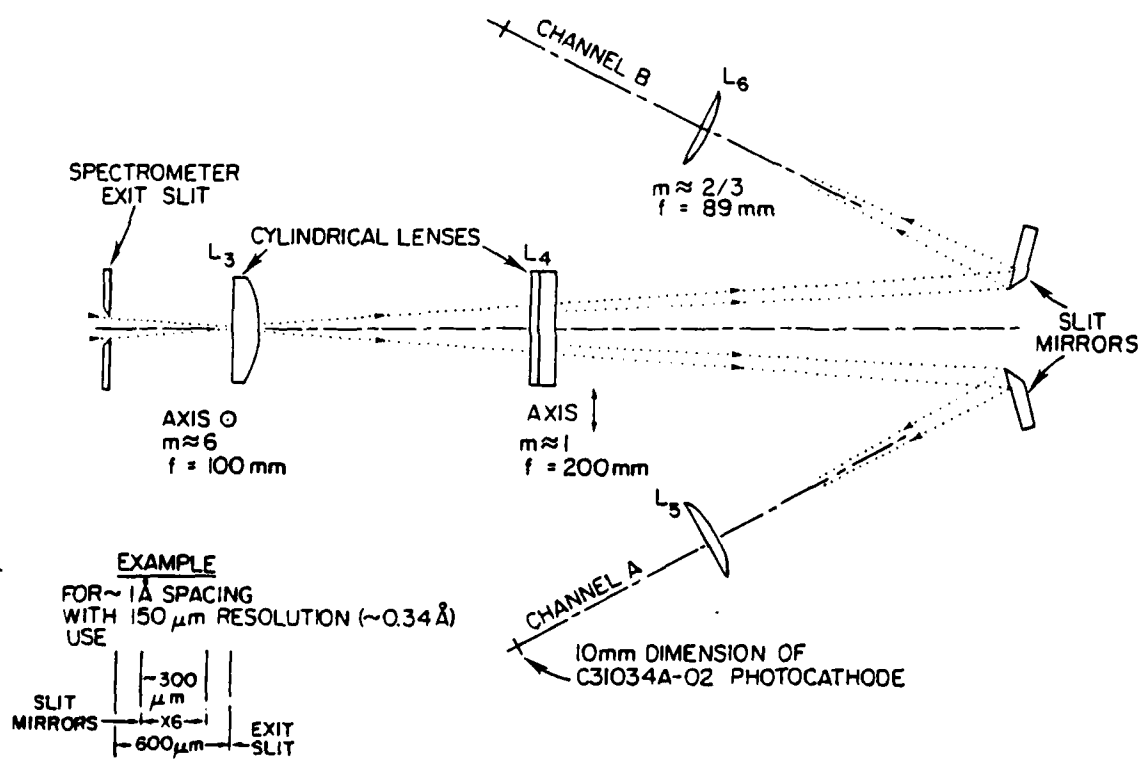
Figure 11. Configuration of the Exit Slit Optics of the Two-
Channel TiLaRS System.

shown in Figure 11, to give a reflecting edge straight and sharp to within 100 µm. They are coated for better than 98% reflectance of unpolarized light at 10-15° incidence in the 470-560-nm band. The light reflected from each slit mirror is focused by a 50-mm-diameter convex spherical lens L_5 or L_6 onto the PMT. The entire exit-slit optical subsystem and the PMT's are enclosed in a light tight box. The box has a removable lid or cover which uses a strong aluminum-angle frame and interlocking strips of neoprene sponge stripping to create a multicorner light trap between the cover and the box. The dark count rate of the PMT's shows no increase when the PMT shutters are opened and the exit slit is closed, provided all access holes in the box are covered.

The success of the two-channel exit-slit optics depends on the quality of the internal alignment of the spectrometer exit slit. The history of the instrument[31] plus the magnification to be used as shown in Figure 11 made it necessary that the instrument performance be checked. At the onset of the construction of the exit slit optics, a detailed alignment was carried out on the final focus and orientation of the exit slit of the spectrometer. The measured performance of the instrument in third order following realignment showed good agreement with the manufacturer's performance data. Figure 12 presents the second-order performance needed for the TiLaRS design. It is evident from Figure 12 that for slits widths over 100 µm, slit heights up to 10 mm can be used with no loss in resolution and that heights up to 5 mm can be tolerated for slit widths under 100 µm.

The performance of the system with regard to signal level was checked against the predicted level obtained from Equations (1) through (9), with the exception of Equation (7). The detection efficiency ε, which is the product of the QE of the PMT
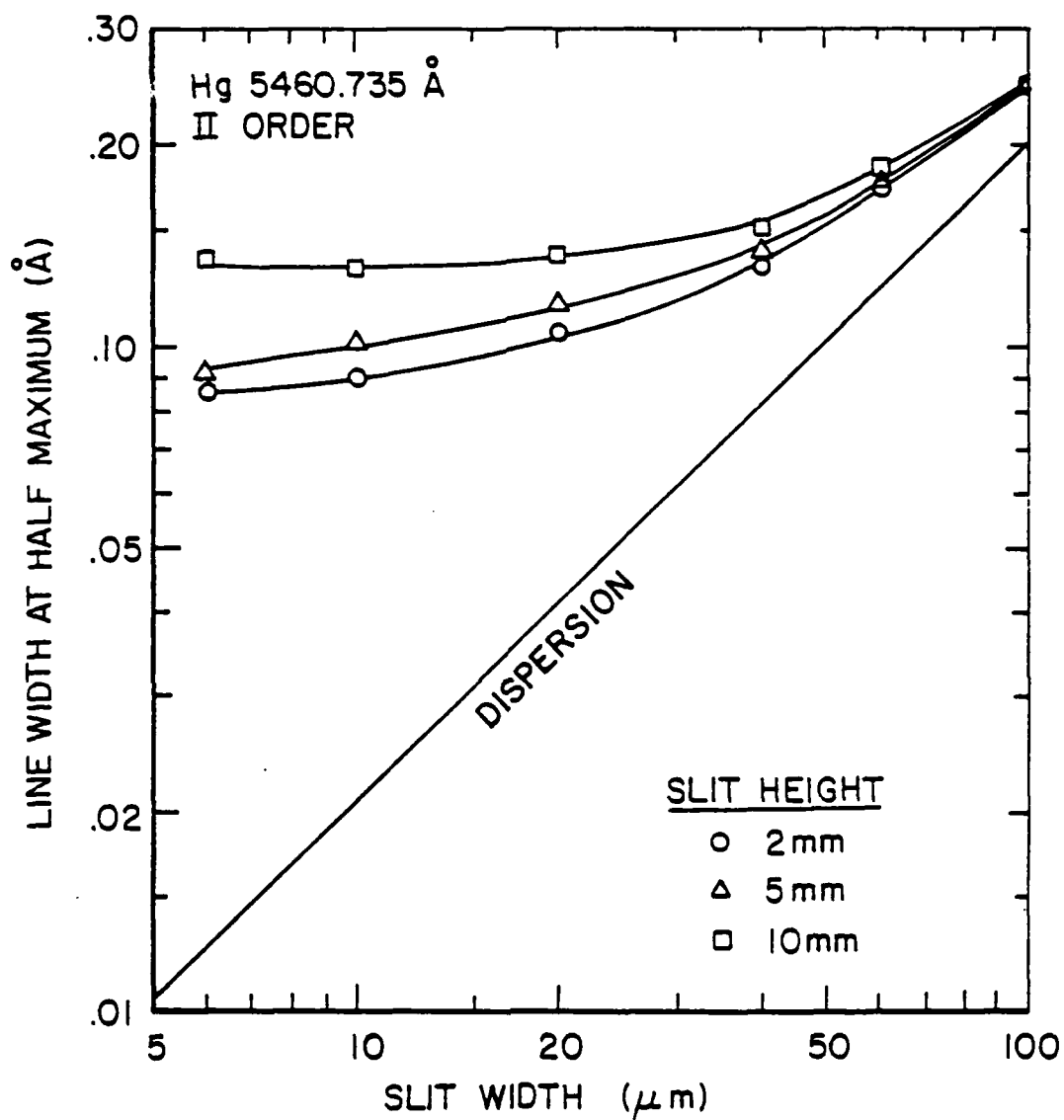
Figure 12. Resolution Measurements on SPEX Model 1402 Double Spectrometer Using the Mercury 546 nm (5,460.735 Å) Line in Second Order. (The reciprocal-linear-dispersion line is the manufacturer's specification.)

46

and the transmittance of the optical system, was estimated to be about 1.5% to give the observed signal. If the QE is assumed to be 20%, the overall transmittance is 4%, accounting for the increase by a factor of 1.9 due to the reverse optics mirror. This is somewhat less than the 8.6% value arrived at by direct measurement and estimates. The on-axis transmittance of the spectrometer weighted for the polarization of rotational Raman light was measured to be 15.6%. Apparently a combination of low QE and light losses, probably in the exit slit optics, is responsible for the loss in detection efficiency. This discrepancy is probably not too unreasonable in view of the complexity of the route over which the light travels. It should also be noted that the expected transmittance of the spectrometer based on reasonable estimates was nearly a factor of three higher than the measured value. This can be attributed to the deterioration of the grating and mirror surfaces due to many long exposures to hot, humid conditions in the studies that preceded this work.[31]

3.2.2 Electronics

The layout of the two-channel, photon-counting electronic system and the data acquisition scheme is given in Figure 6. The RCA C31034A-02 PMT's are selected by the manufacturer for high QE (the "A") and for low dark count (the "02"). These tubes are specified to have a QE of ~25% and a dark count of ~12 counts/s. Furthermore, the relative response is virtually flat over the 300-to-800-nm range and they have a rise time of <2 ns. These positive characteristics are offset by a relatively high vulnerability to damage by high count rates and by the low 0.3-to-3-mV output pulse height into 50 Ω. We have observed that these tubes show a permanent increase in dark count followed by a loss in QE with illuminations that produce much in excess of 350 kcounts/s. As shown in Figure 6, a total gain of about 200 is needed to exceed the minimum discrimination level of 30 mv of

47

the LeCroy 821 module for good counting efficiency. (Except for the Ortec 9301 preamps, the LeCroy and the Ortec units are NIM modules.) The PMT output is governed by the high voltage level. The values used are those specified by RCA to give a multiplier gain of 10^6. The PMT's are cooled to about $-30°C$ which is essential with these tubes to obtain the low dark count.

The standardized output pulses from the discriminators are counted by the Ortec 771 counters supplied with the parallel output option. The four lowest BCD digits of the parallel output register of the counters all transferred to a general purpose interface board (GPIB) of the Nova minicomputer. The Ortec counters require a positive logic, TTL input pulse where the LeCroy 821 supplies the negative logic, fast NIM pulse with variable pulse width. Two Hewlett-Packard (HP) pulse generators are used to couple the discriminators to the counters.

The time interval of each pair of measurements is determined by the setting on a modified Ortec 773 timer. The modification entailed changing the countdown circuit driven by a crystal-controlled clock, so as to reduce the reference time base to 0.01 ms.[27] The time-base accuracy is specified to be 1 ppm. At the end of the interval an interrupt pulse is sent to the minicomputer, which subsequently reads the contents of the counter registers and then sends reset pulses to the 771's and the 773. The read cycle repeats as soon as the 773 reset pulse goes low. The number of read intervals recorded is determined by software. The read-to-read time interval was measured to be a constant 10 μs longer than the interrupt or read interval at least up to a read rate of 20 kHz. Since this is directly due to the 10-μs reset pulse, it indicates that the computer read cycle is of negligible duration (<1 μs).

48

The LeCroy discriminators have several outputs which are useful for supplemental functions. As shown in Figure 6, one output of each channel drives a Monsanto counter which is used as a digital count rate monitor. Such a function is extremely useful in the final alignment of the optics and gain measurements. Another output can be connected to the Ortec 449 analog ratemeter. The output of this ratemeter is used to drive the Y axis of an X-Y recorder in which the X deflection is scanned linearly in time. The "Compudrive" wavelength drive unit for the spectrometer can be externally triggered using the interrupt pulses from the 773 timer. This capability permits spectral scans to be recorded, which is essential to determining the shape and width of the channel pass band. Ordinarily a given line is scanned through channel A first, after which the ratemeter input is quickly moved to channel B to record the same line through B channel without interrupting the scan. Thus, the channel width, shape, and spacing can be recorded and measured. Examples of these scans are given in Section 4.

3.2.3 Software

The software for the TiLaRS system can be conveniently divided into data acquisition and data analysis routines. The most recent version of the acquisition program is LABMATE; while ANPRO2 is the latest version of the data analysis program. The program LABMATE resides in the Data General (DG) Nova 1220 minicomputer and uses the real-time operating system RTOS. This operating system permits Fortran and Assembler languages to be used in the program. The program ANPRO2 is written in Fortran IV, extended, for the VAX 11/780 computer. These interactive programs are briefly described in this section, while more detailed descriptions of them and their subroutines are given in the Operations Manual for the TiLaRS system.[27]

The other programs important to the operation of the TiLaRS system are TRANS, NOVAIN, and PROFPLOT. The program TRANS resides in the Nova and is used to prepare and send a data set stored on floppy disk to the VAX. The program is completely interactive and guides the operator through the transfer procedure. The program NOVAIN resides in the VAX, accepts the data transmitted by the Nova, and creates a disk file. The program PROFPLOT is an interactive routine which makes PLOT 10 software available for plotting profiles of data generated through the use of ANPRO2.

The program LABMATE was written to take data for time-resolved TiLaRS experiments. It was designed to facilitate the process of calibrating the system and taking a series of runs based on that calibration. The program runs on the Nova minicomputer and must be used in conjunction with the Tektronix 4010-1 graphics terminal and the Tektronix 4631 hardcopy unit.

The program has four modes of operation: (a) Real-Time Temperature Mode, (b) Calibration Mode, (c) Data Acquisition Mode, and (d) Browse Mode. The Real-Time Mode takes a set of data and displays the mean temperature, the standard deviation, and the Poisson uncertainty for that set. The Calibration Mode enables the user to calibrate the relative gain between the two channels and the background signal level of each channel. Data taken during the calibration process are not stored. On the other hand, data taken during the Data Acquisition Mode may be stored in disk files (at the user's discretion). The Data Acquisition Mode also requires knowledge of the relative gain and the backgrounds prior to taking the data set, since these parameters are needed to calculate the temperature. The Browse Mode provides a means to examine the data set header, which

contains information such as the number of data points, the read rate at which the data were taken, etc.

The program ANPRO2 performs off-line data reduction and statistical analyses of two-channel TiLaRS measurements of temperature and/or species concentration fluctuations. The data files are uploaded from the minicomputer data acquisition system to the VAX. Each data file consists of a header, followed by the sequential data, which is in terms of photoelectron counts per read. Each sequential pair of data corresponds to the simultaneous measurements of two channels, and is interpreted either as a temperature measurement, two concentration measurements at constant temperature, or a simultaneous measurement of temperature and concentration.

Several methods are employed to ensure the validity of the analysis. Reduced data outside a user-determined number of standard deviations can be substituted with another value, and values exceeding a threshold value may be deleted. The signal-to-noise ratio of each read may be increased by reducing the effective read rate of the run. This is done by adding the reads within sequential, nonoverlapping intervals, this assuming that the dead time between reads is negligible.

All plots are produced by PLOT 10 utilities and a Tektronix 4010-1 terminal. Plots can be made of probability histograms, power spectral densities, autocorrelations, crosscorrelations, and real-time values of the reduced data. Various IMSL routines are used to calculate these functions. The average of a series of power spectral densities, autocorrelations, or crosscorrelations of similar runs may also be plotted.

A data file can be created, using ANPRO2, which contains some of the results of the statistical parameters calculated by the program and the X-Y-Z coordinates (with respect to the nozzle) where the data were taken. From this file, a profile of the flame or jet can be plotted using the PROFPLOT program.

The main program supplies most user prompts, organizes the sequence of subroutine calls, determines parameters to be passed to the subroutines, initializes some of the variables, and calculates the averages of the analysis as discussed above. The various options described above are provided through a master menu and an analysis menu.

3.3 SYSTEM PERFORMANCE

The programs described in the previous section, as well as the earlier versions not mentioned here, required extensive development and testing to bring them to their current operational status. The testing not only included the analysis of pseudodata prepared with known parameter values, but also testing of the entire TiLaRS hardware-data-acquisition-data-analysis system using light signals having known characteristics. In the latter regard, several tests were carried out using a sine-wave-modulated light source. One series used a green-emitting LED driven by a current source giving a 20-Hz sine wave with a dc offset.[7] Runs with varying signal levels at constant read rate and varying read rates at constant signal level were analyzed by means of pdf's and psdf's. These functions were found to be in excellent agreement with theoretical predictions.[32]

A second series involved an 84-Hz sine-wave modulation of the laser using the built-in light-control circuit. A peak-to-peak modulation equal to 27% of the average count rate was used. The temperature psdf of a 4096-point record showed that the

temperature fluctuation amplitude could be no greater than
5 K rms. The measured mean temperature was ~300 K. Actually,
there was no unambiguous indication of a signal at 34 Hz since
about 4% of the spectrum due to noise was >5 K rms. Since the
temperature depends only on the ratio of the signals from the two
channels, this test result confirmed that the dual-channel
hardware and data-acquisition software were functioning
precisely.

During the early stages of testing, the temperature-
measuring capability of the system was checked with hot, flowing
air. This check was carried out using a pair of PMT's that had
been damaged by excessive light levels such that the count rates
were about a factor of five smaller than the currently available
signals. (The paper on the TiLaRS work, which is Reference
No. 18, also used these damaged tubes.) Nevertheless, even
though the signals were not optimum, the calibration was able to
be checked.

The calibration checks were made using both the 7/4 and
9/6-mixed pairs of lines. (See Table 1 and Figure 1.) A No. 20
beaded chromel-alumel thermocouple mounted within 2 mm of the
downstream side of the Raman sample volume on the Z-axis was used
(see Figure 9). A Keithley model 870 digital thermometer and a
type 8686 Leeds and Northrup potentiometer were used to determine
the thermocouple temperature. The 7/4 and the 9/6 Raman
temperatures and the thermocouple values usually agreed within
3-4% between 300 and 450 K. These checks were made using
electrically heated air flowing in a 0.5 in. OD (~1 cm ID)
stainless steel tube 75 cm long fitted with optical access
openings. The flow rate was 2 to 4 m/s. The observed relative
standard deviations in the temperature data ranged between 10% at
room temperature to 20% at the high temperature for the 7/4 line
pair and from 4% to 7% for the 9/6-mixed line pair. These data

53

were all taken at a read rate of 10 Hz with 1024 reads. These
uncertainties are essentially equal to the values calculated with
Equation (33) indicating that there was no detectable system
noise and no observable fluctuations in the temperature of the
air. Regular checks on the temperature accuracy are accomplished
indirectly by comparing the directly measured gain ratio R_ϵ to
the gain ratio needed to bring the calculated temperature in line
with the observed temperature. The agreement between these
values is on the order of 0.1% when the measurements are done
very carefully.

The analysis software was extensively tested at the various
stages of development. Scaling problems were resolved by
comparing computed values against the known input parameters.
The effect of data preparation and presentation procedures on the
results was examined extensively. For example, it was found
that when generating histograms of the data from one channel, as
in concentration studies, the synchronous, time-averaged sampling
of the data caused periodic "holes" or dips in the histogram
whenever the width of the bins (given in kcounts/s) is not an
integer multiple of the read rate. This arises simply from the
fact that the signal within the read (i.e., sample) intervals is
a discrete number of pulses, and therefore can only change in
integer steps which, in fact, correspond to integer multiples of
the read rate. A pdf bin width that is not an integer multiple
of the read rate is subject to a periodic digitizing bias that is
a function of the electronic decision-making circuits.

The latest version of the analysis program ANPRO2 was
tested using artificially generated data, referred to as
pseudodata, which could be configured to have precise properties.
The temperature pdf, psdf, and acf were checked using pseudodata
containing a fluctuation of temperature having a constant sine
wave amplitude. Similarly, tests using a damped sine wave were

carried out. The plots of the three functions for these signals were in excellent agreement with the input parameters of the data after the debugging was completed. This effort identified the need to use "sliding" limits and normalization in using the acf code supplied by the IMSL utility software. This "apparent acf" gives a viable plot as long as the maximum lag is somewhat less than the record length.[33]

The calculation of the psdf is distinct from the calculation of the acf in that the acf involves an averaging of a large number of products for each lag value, at least for lag values that are much smaller than the record length. Therefore, to obtain a reasonable (i.e., low noise) estimate of the acf, a record length much greater than the integral scale of the signal is required. The integral scale is the integral of the correlation function over all lags. It is a measure of the correlation time of the signal. However, in the calculation of the psdf from the Fourier transform of a single data record, it is easy to show that this amounts to only a single determination of the "power" at each frequency of the calculated spectrum.[34] This means the uncertainty of this determination is 100%. Thus, a psdf determined from a single data record will have a noise level equal to the mean value of the spectrum. This noise level can be reduced by averaging a large number of spectra, by smoothing a single spectrum, or by a combination of the two methods. The smoothing operation can be accomplished either directly in the frequency domain or by applying a "lag window" to the acf and obtaining the psdf by a Fourier transformation of this smoothed acf.[33]

In the current version of ANPRO2, two smoothing schemes are provided. One is a simple cosine filter function applied directly to the frequency spectrum, and the other permits averaging the psdf's or the acf's taken from a number of

55

independent records or from a number of segments of a single record where overlapping segments are permitted.[35] Basically, the fractional uncertainty of a spectral value is approximately $1/\sqrt{N}$ where N is either the number of records or segments averaged, or it is the product $T\Delta f$ where T is the time-length of record used in calculating the psdf and Δf is the bandwidth of the smoothing filter.[34] Thus, to obtain a 10% uncertainty in the psdf, 100 records or segments can be averaged. Or, a ~4-sec record obtained from 4096 reads at a 1-kHz read rate can be smoothed using a 25 Hz filter to give ~10% uncertainty. In this latter example, the maximum frequency allowed by the Nyquist criterion is 500 Hz,[9] which means the resulting frequency resolution is 5%. The resolution of the unsmoothed spectrum is 1/T which, in this case, is 0.05%. Thus, the smoothing operation and segment averaging trades resolution for precision, while averaging independent records trades uncertainty for measurement time. Smoothing definitely introduces a bias while averaging may or may not, depending on the character of the data.

In the segmenting procedure, there is the additional problem of the "data window" used to define the segment.[35] As the segment is reduced in length, the frequency resolution in the psdf drops. The shape of the data window in the time domain, when transformed to the frequency domain, introduces "ringing" which adds signal due to a particular frequency to neighboring frequency points. This represents a bias which can be adjusted by the choice of data window. ANPRO2 provides the option of three data windows for this type of analysis.

SECTION 4

MEASUREMENTS

The measurement activity during this program was directed at
one or more of the following: testing the hardware, testing the
software, and/or testing the measurement capability in a CH_4
flame or a CO_2 jet. The first results of this testing activity
were presented in a paper given to the Sixth International
Temperature Symposium held in Washington, D.C. from March 15 to
18, 1982.[18] The purpose of these preliminary results was to
illustrate the capability of the TiLaRS system. At this point,
an extensive effort was begun to expand and develop both the data
acquisition and data analysis software as well as to make
improvements in the hardware. Fortunately, the new and revised
analysis programs were completed in time to allow two new
measurement studies of gas flow dynamics. The first was
essentially a repeat of the flame measurements reported at the
symposium, and the second was our first quantitative study of a
room-temperature CO_2 jet. The measurement circumstances differed
from the first measurements in that we had two new PMT's and we
used $J_A = 11$ and $J_B = 8$ lines for the temperature measurements.
The new PMT's provided about a five-fold increase of QE and the
11/8 pair of lines provided the capability for going into the
flame, which was not possible with the mixed-9/6 lines used in
the early work.[18]

4.1 METHANE FLAME STUDIES

Temperature measurements in a flame using two pure Stokes
rotational RS lines can be accomplished, provided the following
conditions can be fulfilled: (a) the background signals in the
two channels, including RS from species other than the probe

57

molecule, are sufficiently steady to permit them to be measured independently before and/or after the temperature measurement; (b) the slope of the calibration curve is not excessive in the temperature range of interest (see Figure 1); and (c) the spectrometer entrance slit dimensions are large enough to include any image shifts due to schlieren effects on the laser beam in the observed volume caused by the fluctuating index of refraction. Dynamic temperature measurements can be accomplished only when the observed standard deviation is noticeably larger than the Poisson uncertainty for the expected count rate and the intended read rate. The interplay between these quantities and the background signals was discussed in Section 2.3 and plotted in Figures 3 to 5.

4.1.1 Setup and Calibration

The arrangement of the fuel tube, as shown in Figure 9, was horizontal with the combustion products exhausted by means of a 50-mm diameter pipe connected to a small centrifugal blower. This blower also provided a small, stabilizing air flow around the nozzle. The pipe was set approximately axial to the nozzle and about 90 mm downstream of the nozzle. The nozzle was a Delavan No. 20, WDA, 45° spray nozzle used without the "distributor" (i.e., swirler) and the strainer. This nozzle has a 1.4-mm (0.055 in.) diameter orifice and was mounted on a straight, 75-cm-long, heavy-wall stainless steel tube. The X-Y-Z position and alignment of the tube and nozzle were accomplished by five Uni-Slide translation stages calibrated to 0.05 mm. The inside diameter of the tube was 1.0 cm. The horizontal flow of the methane flame used in these studies produced an asymmetry in the flame due to bouyancy; however, this feature was outweighed by the considerable convenience and optical simplicity of the arrangement. Ultrapure methane was used without premixing. The high purity was used to ensure that there would be minimum

58

background signals from fluorescing impurities. Methane was chosen because it is a spherical top molecule and therefore has no observed pure rotational Raman spectrum at ordinary pressures.[23]

The choice of flow conditions of the diffusion flame was largely determined by the maximum flow rate that could be achieved with a stable flame. A volume flow rate of 1.8 ℓ/min, corresponding to a mass flow of 0.07 kg/h and an exit velocity of nearly 20 m/s, was used. The cold flow Reynolds number (Re) was about 1,600. The flame extended several centimeters into the exhaust pipe where it was a bright orange. The upstream portion of the flame was blue except for a ridge of orange along the top edge.

The measurements were made along the radius (i.e., along X) at 2 1/2 nozzle diameters downstream (i.e., $Z = 2$ 1/2 d). This axial position was chosen because there was little evidence of incandescent soot at this location. Thus, the background signals were due primarily to leakage of the laser light through the spectrometer and possibly fluorescence. The reflecting surfaces of the mirrors and gratings in the spectrometer are considerably reduced in reflectance, which undoubtedly contributed to increased scattered laser light inside the spectrometer. We note here that it would not generally be possible to make viable measurements at the above axial position using a hard probe.

The first task in making a measurement with the TiLaRS system is to determine the settings of the exit slit and the slit mirrors. The maximum width of the exit slit of the current spectrometer is 3 mm. Since the gratings were blazed at 500 nm in second order, this constrained the choice of line pair of the N_2 probe molecule to those separated by $\Delta J = 3$. This limitation has a significant impact on the high-temperature performance of

the TiLaRS system. This can be seen by comparing Figures 3 and 5 which are plots of the temperature uncertainty s_T given by Equations (33) and (34). The dependence on the spacing of the lines is contained in the value of K_1 defined in Equation (16). Using Equation (13), K_1 is proportioned to $-(J_A-J_B)(J_B+J_A+1)$. Thus, the uncertainty is inversely proportioned to $\Delta J=J_A-J_B$ times the J-sum plus one. Since ΔJ changes much faster than the sum for small ΔJ, the J-difference is primary in setting the value of s_T for different J pairs.

The specific line pair chosen also impacts s_T through the uncertainty in the ratio $s_R/\bar{R}$ in Equation (33) which is given by Equation (34) or (38). This factor depends on the count rates in the two channels and the read rate. One of the disadvantages of $\Delta J=3$ is that one line is always about half the intensity of the other. This is due to the nuclear spin degeneracy factor g_J in Equation (2) which is 6 for even-J lines and 3 for odd-J lines. For $\Delta J=4$, this degeneracy factor can be 6 for both lines. An important quantity which determines in part the intensities of the lines is the Boltzmann factor in Equation (2) which characterizes the population distribution among the rotational levels. However, the dependence of the count rate $\dot{n}_J$ in Equation (1) on J includes additional factors containing J in Equation (8). By including all these factors and neglecting the J dependence of ν_J in Equation (9), we obtain the expression for the temperature at which the signal is maximum for a given J value. Thus,

$$T_{max \; \dot{n}} = 1.4388 \; B_0 \; \frac{(J+1)(J+2)(2J+1)(2J+3)}{(2J+3)^2 - 2(J+1)(J+2)} . \qquad (40)$$

The values obtained from Equation (40) are plotted in Figure 13 on the abscissa. This interchange of variables made it
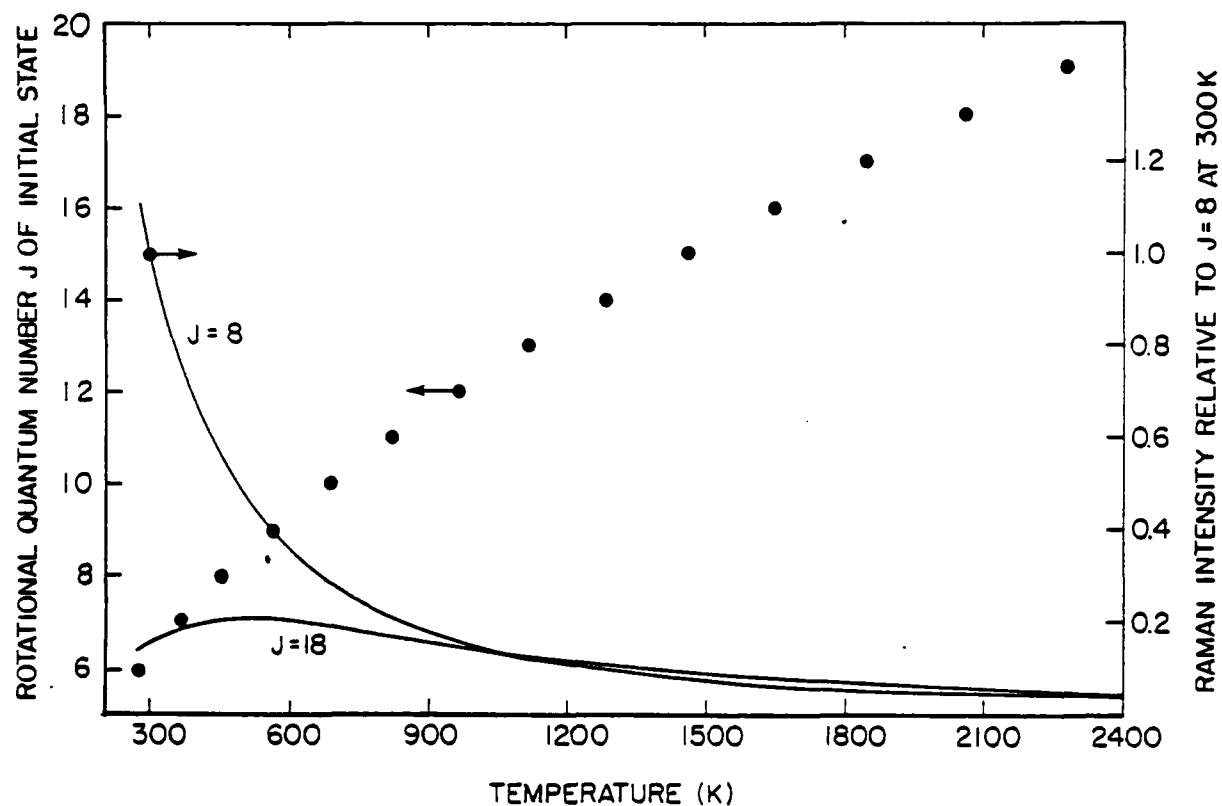
Figure 13. Temperatures of Maximum Raman Signal for Rotational States of N_2 for $J = 6$ through 19 and the Relative Intensities of the $J = 8$ and 18 Lines Versus Temperature. [See Equation (40) for the left-hand plot and Equations (1) to (3), and (8) for the right-hand plots.]

61

convenient to plot on the same graph the relative intensities of the J = 8 and 18 lines referred to the J = 8 line at 300 K. Equations (1) to (3), and (8) were used to generate these curves. The two curves include the inverse square temperature dependence introduced through the combination of the partition function and the gas law given in Equations (5) and (6). The plots show that even though J = 18 has the highest intensity at ~2,060K, the intensity of the J = 8 line is only 30% weaker. Thus, above 1,200K or so, the intensity differences are not very large, at least for the range of J = 8 through 18 approximately.

There are, finally, two additional considerations which turn out to be the most important from a pragmatic viewpoint. The first concerns the interferences between the O_2 and N_2 lines, and the second is the availability of close neighboring regions of the spectrum where the background signals can be measured. The interference-free pairs of lines available out to J = 21 that have ΔJ = 3 are 7/4, 10/7, 11/8, 14/11, 17/14, 20/17, and 21/18. Because of relatively wide bandwidth of 0.064 nm (300 μm slit) used in these studies, the J = 10 and 18 lines have some marginal interferences. This means that it would take somewhat more care and testing to ensure that either of the lines is acceptable. The line pair 7/4 proved to be unusable in the flame because of the relatively large increase in the background near the laser line wavelength. Background measurements were most conveniently made when the spectrometer wavelength setting, and therefore the two channel wavelengths, could be displaced slightly high or low to line-less regions. The width of these regions should be ideally about the channel bandwidth or wider. Only the 11/8 and 21/18 pairs satisfy this criterion. Since the high temperature intensity is not a strong function of J as described above, the 11/8 pair was chosen because of the convenience of having a strong signal at room temperature for calibration purposes. If

62

narrow neighboring background regions are feasible, the 14/11 or the 17/14 pair could possibly be used.

The channel bandwidths and the channel spacing are determined by the settings of the exit-slit width and the positions of the slit mirrors. For temperature measurements, an effective exit-slit width of 250 or 300 μm has been satisfactory. The theoretical spacing of two N_2 rotational Raman lines with $\Delta J = 3$ is 0.572 nm. For a linear reciprocal dispersion of 0.227 nm/mm, this spacing corresponds to a separation in the plane of the exit slit of 2.520 mm. This requires the exit-slit width to be 2.820 mm for 300 μm channel widths. The slit mirror spacing is then 2.220 mm referred to the exit-slit plane. The actual spacing of each mirror from the reference position corresponding to 100 μm (0.1 mm) in the exit-slit plane is given by (2.220-0.1) x 5.85/2 = 6.20 mm, where 5.85 is the magnification due to L_3 in Figure 11. This calculation is given to illustrate the procedure used for setting the exit slit and slit mirrors. The entrance slit was set to 300 μm. With the image of the laser beam being about 80 μm, this setting provided some latitude for movement of the image due to schlieren effects.

The channel bandwidths were equalized before the gain calibration was done. This is accomplished by adjusting the transverse position of L_3. The procedure is to carefully measure the full widths of the two lines at half maximum (fwhm) and then introduce the appropriate shift in L_3. This adjustment is extraordinarily sensitive. The measurement is made on a scan of the spectra of the two channels obtained with the rate meter and X-Y recorder shown in Figure 3. Generally, it is possible to equalize the widths to within ± 0.001 nm. An example of a scan of the two channels using the 60 cm^{-1} line is shown in Figure 14. The widths of the test line in the two channels are both equal to 0.064 nm for the 300 μm effective exit-slit width set up as a goal, which is only 0.004 nm smaller than the design value. The
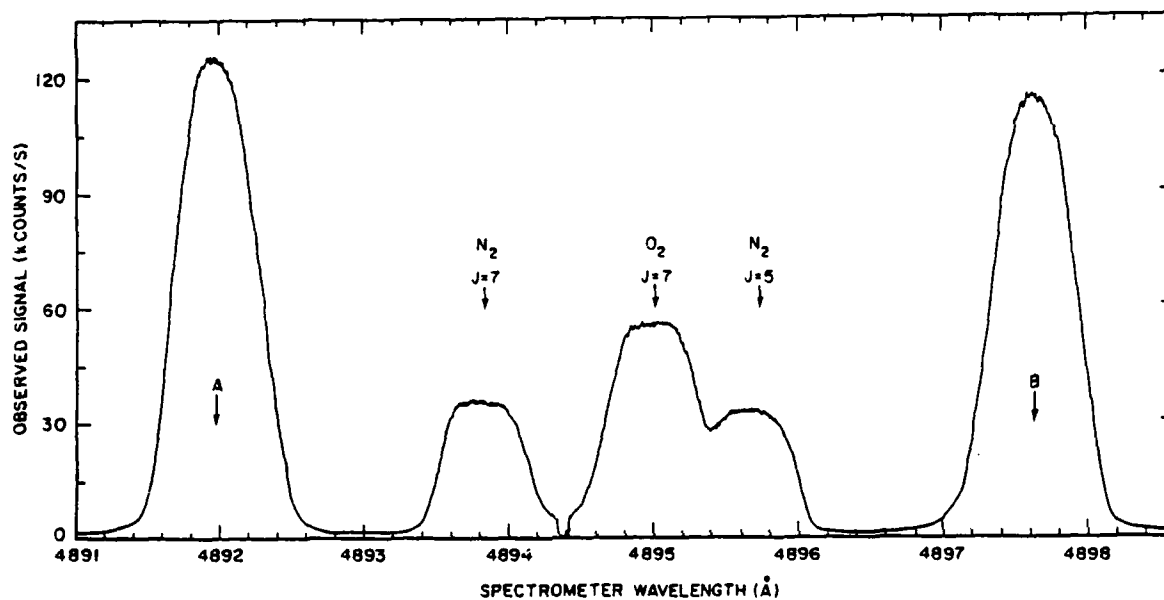
Figure 14.   Typical Sequential Scans of the 60-cm⁻¹ Line of Room
Air with Channel A Followed by Channel B of the
Aligned TiLaRS System.   [See Figure 2.   Entrance
slit source-limited to about 80 μm, exit slits at
300 μm, slit height at 2 mm, and laser power at 2 W.
The channel-B scan starts at 489.44 nm (4894.4 Å).]

64

spacing measured 0.565 nm as compared to the design value of 0.572 nm. This discrepancy was made up by adding small corrections to the adjustments.

The final task in setting up the TiLaRS system for temperature measurements is to carry out the gain calibration. This entails measuring the ratio of the channel-A gain to the channel-B gain given by R_c in Equations (15) and (31). This is most conveniently done at room temperature by determining the value of R_c that gives the temperature of the observed volume. This temperature was measured using a thermocouple placed in the ambient air near the laser beams with a Keithley model 870 digital thermometer. The specified accuracy of this instrument at room temperature is ±1°C with a resetability of ±0.2°C. The sensitivity of the feasible accuracy of measurements at high temperature, > 1000 K, to the accuracy of the room temperature calibration is significant. This sensitivity is due to the high slope in the high-temperature region compared to the slow-changing character of the curve around room temperature as seen in Figure 1. The calibration accuracy needed in a specific case can be obtained from the curves given in Figures 15 and 16. These curves were obtained from Equations (14) and (15). For example, in Figure 15, at 1,500 K for the J_A/J_B = 11/8 line pair, the temperature changes 130 K for a 1% change in gain. From Figure 16, a 5.3 K change in temperature at 300 K is produced by a 1% change in gain. Thus, the temperature calibration at 300 K must be better than 0.5 K to give a feasible accuracy of 13 K at 1,500 K. These curves also illustrate the sensitivity of the measurements on the uncertainty in the ratio (R) due to the noise on the two channels wherein the change in R (ΔR) is equated to the noise amplitude. Since the gain calibration was to better than ±0.1%, the measurement accuracy was primarily limited by the performance of the thermocouple-digital-thermometer setup. Comparison of different thermocouples and use of a potentiometer
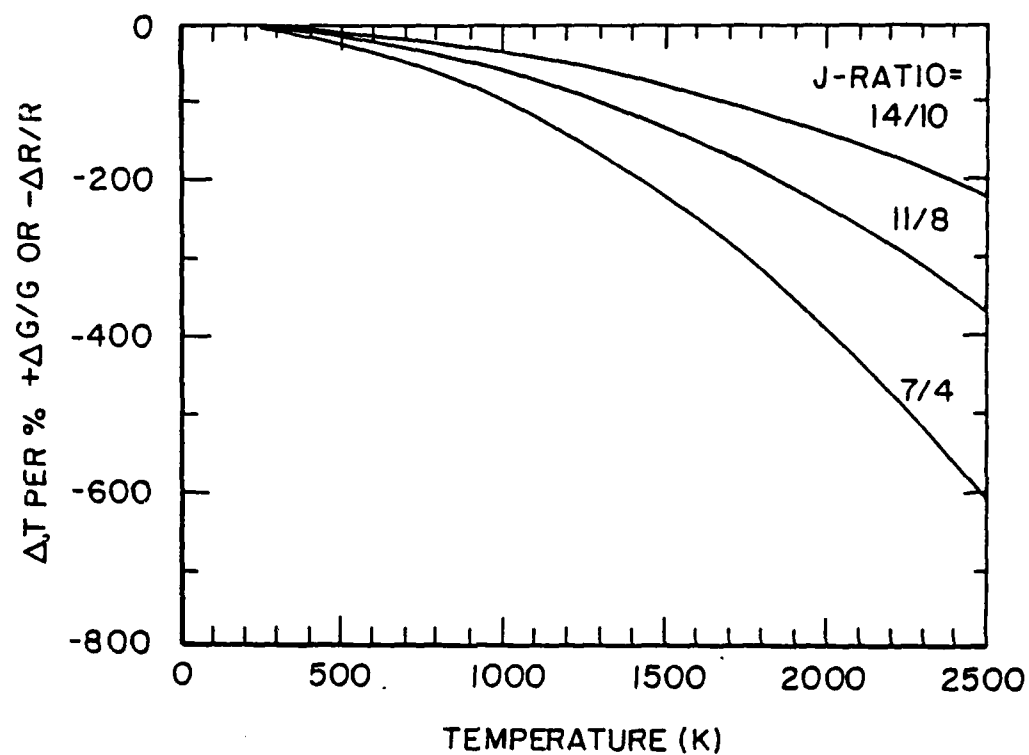
Figure 15. The Temperature Change Due to Percent Increase in Gain or Decrease in Ratio for the Calibration Curves in Figure 1.

66
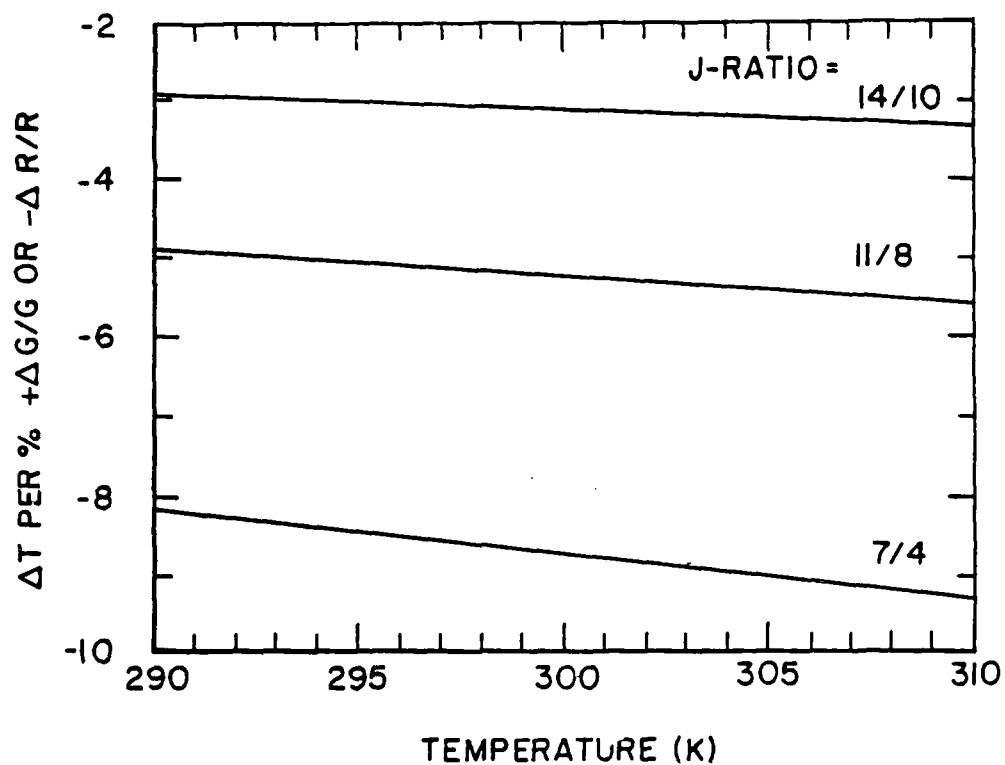
Figure 16. The Temperature Change Around 300 K Due to Percent
Increase in Gain or Decrease in Ratio for the Cali-
bration Curves in Figure 1.

67

suggested the overall accuracy was about ± 1 K at room
temperature. This corresponds to an effective gain uncertainty
of about 0.2%. This value can be used with Figure 16 to obtain
the feasible accuracy of measurements in the flame.

4.1.2 Data and Results

The radial measurements were taken from X = 0.0 to 0.5 cm in
0.1 cm intervals. Either 2,048 or 4,096 reads were taken at read
rates of 20, 50, and/or 100 Hz. The higher read rates were
possible in regions of lower temperature, namely at X = 0.0, 0.4,
and 0.5 cm. The background signals were measured by shifting the
spectrometer wavelength up 0.08 nm corresponding to 3.4 cm^{-1} in
Figure 2. These measurements were made at a read rate of 1 Hz
for 64 reads either just before or immediately after the
temperature measurement. Since the relative background signals
$\bar{b}'_{AA}$ and $\bar{b}'_{BB}$ [see Equation (35)] were ~40-60% in four of the six
runs, the background signals at the J = 8 and 11 wavelengths were
determined by linear interpolation from the values obtained at
the shifted setting. The background ratio R_b ranged from 80 to
90%.

4.1.2.1 Probability Analyses

The temperature measurements from the six runs are presented
in probability histograms given in Figure 17. The bin widths
(200 K) and the scales were made the same in all the plots to
facilitate comparisons. Except for X = 0.4 and 0.5 cm, the read
rate of the data used to obtain these plots was 20 Hz. The data
for X = 0.4 cm was acquired at a 50-Hz read rate which was
reduced to 25 Hz for Figure 17. Likewise, the data for
X = 0.5 cm were acquired at 100 Hz and reduced to 20 Hz for the
figure. The height of the highest-temperature bin results from a
clipping procedure in the analysis. In the hotter regions of the
flame, namely at X = 0.1, 0.2 and 0.3 cm, the Raman signal ratio
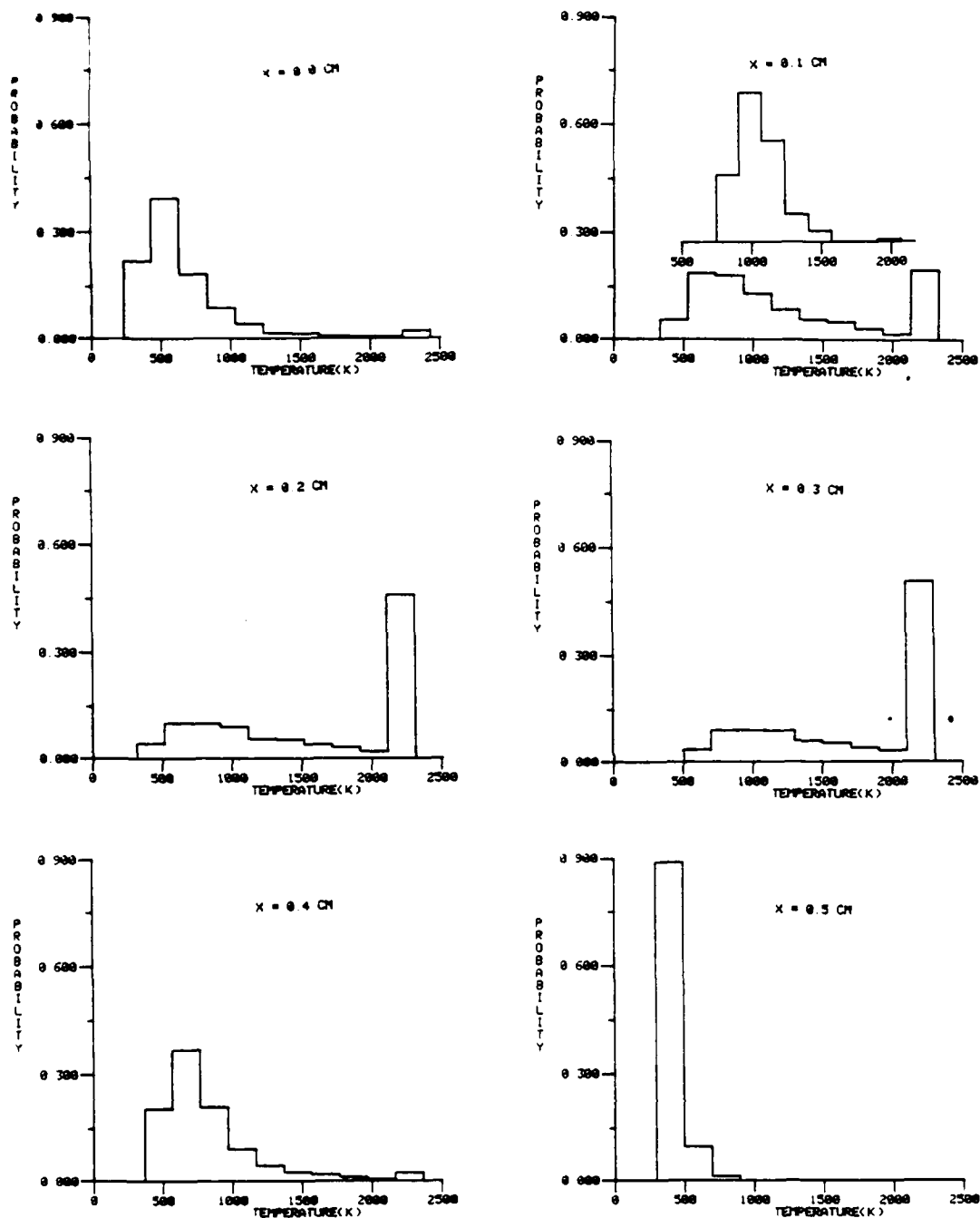
Figure 17. Temperature Probability Histograms for the Methane
Diffusion Flame in Air at Z = 0.35 cm (2.5d) for a
Read Rate of 20 Hz. (Radial positions are in steps
of 1.43r. Bin widths are 200 K. Inset at X = 0.1
cm is for a reduced read rate of 1.25 Hz. The cold
flow Reynolds number at the 1.4-mm diameter orifice
was 1600.)

69

increases to the high-slope region of the calibration curve (see the 11/8 curve in Figure 1). For example, at 2,000 K, Figure 15 gives about 2,000 K temperature change for only an 8% change in ratio. Such fluctuations produce nonphysically acceptable values. The preferred solution to this difficulty would be to use a different calibration curve, such as the 14/10 curve in Figure 1. Since this was not possible in our work, our recourse was to clip the high-temperature excursions in the calculations at 2,250 K, which is the maximum temperature allowed for a methane flame in air by the adiabatic equilibrium calculation.[36] The X = 0.1, 0.2, and 0.3 runs are the most affected by this procedure.

However, as can be seen in Figure 17, at least 50% of the measurements were not clipped. This can be appreciated by examining the time record of the actual count rate in channel B for X = 0.3 cm given in Figure 18(a). As shown in Figure 13, the Raman signal drops rapidly with increasing temperature. Thus, the low signal region in Figure 18(a) contributed to the "clipped" bin in Figure 17, while the higher signal portion provided the broad distribution ranging from 600 to 2,000 K. The Poisson uncertainties determined just for the broad distributions in the X = 0.1, 0.2, and 0.3 cm data are respectively 600, 930, and 750 K. These high uncertainties, again, are attributable to the high slope of the calibration curve for temperatures >1,000 K.

Such uncertainties can, in many cases, be reduced by reducing the effective read rate of the data by combining successive reads. This procedure will tend to integrate out the fast, high-temperature excursions that populate the "clipped" bins in Figure 17. The X = 0.1, 0.2, and 0.3 cm data were analyzed at a reduced read rate of 1.25 Hz. Since the Poisson uncertainty is proportional to the square root of the read rate in Equation (38), this lowers the Poisson uncertainty by a factor of four. The impact of this change on the X = 0.2 and 0.3 data
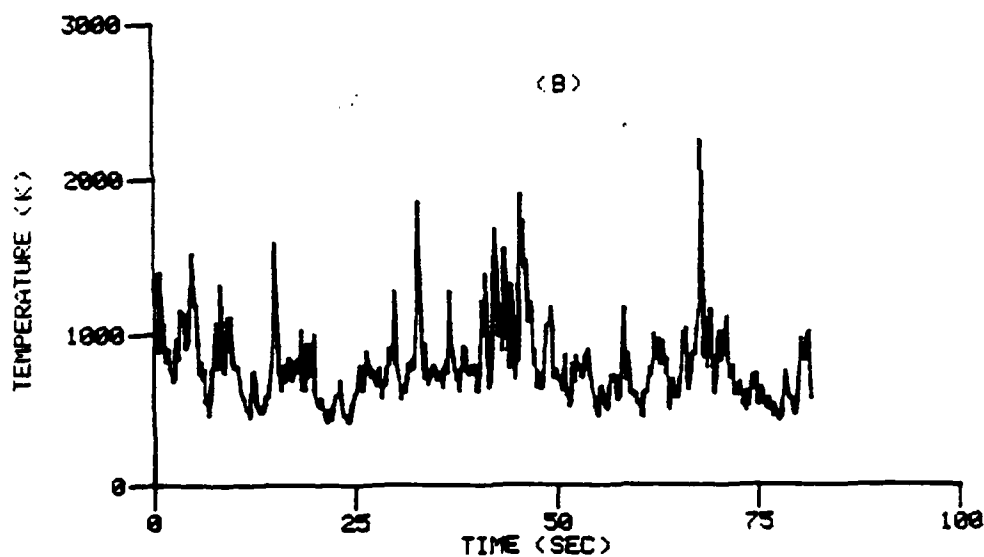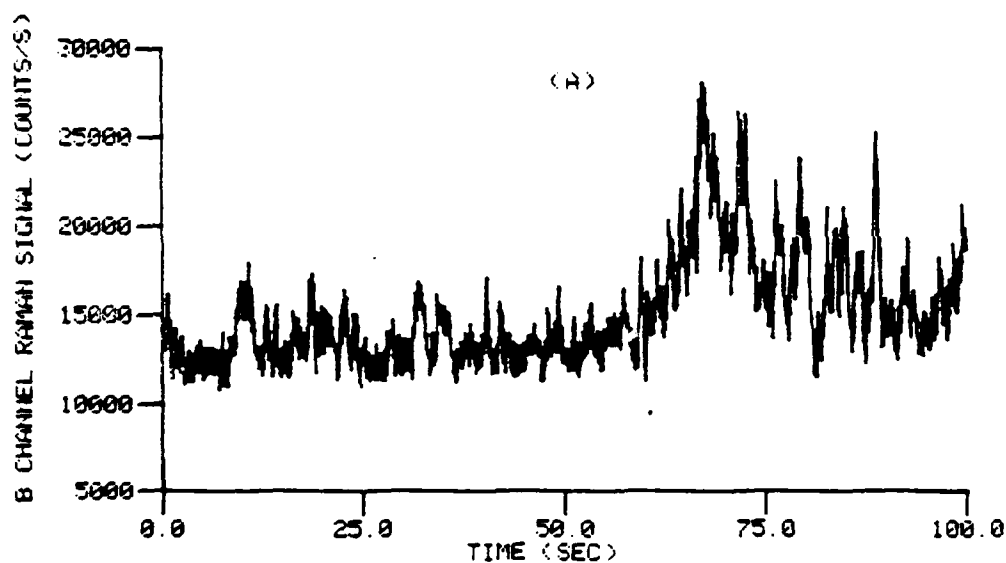
Figure 18. (a) Time Record of the Raw Raman Count Rate from
Channel B of the Methane Diffusion Flame at X = 0.3
cm (4.29r). (b) Time Record of the Temperature of
the Methane Diffusion Flame at X = 0.4 cm (5.72r)
and a Reduced Read Rate of 5 Hz. [The Poisson un-
certainty in (b) is 83 K.]

71

was to increase the measured temperature mean due to a narrowing of the broad distributions. However, the $X = 0.1$ data required no clipping at the low read rate which resulted in a lowering of the mean temperature from 1,238 to 1,060 K. The resulting histogram using the Poisson bin width of 165 K is shown in the inset in Figure 17. Reducing the read rate is also useful for illustrating the fluctuations over the entire record. The temperature record of the $X = 0.4$ data is plotted in Figure 18(b) using a read rate reduced from 50 to 5 Hz. The Poisson uncertainty per read is 83 K for this plot. Thus, the fluctuations shown are largely due to the dynamics of the flame front. This plot plainly shows why large quantities of data are needed to accurately characterize the statistical properties of variables in turbulent flows.

The results obtained from the data plotted in Figure 17 are summarized in Figure 19. In addition to the mean temperature profiles at 1.25 and 20 Hz, Figure 19 also includes plots of the channel A background signal as a percentage of the total signal, the percentage of clipped points, and the percent Poisson uncertainty in the Raman signal ratio given by Equation (34). These data show that the number of clipped points is mainly a function of temperature, and hence the calibration curve, rather than due to measurement uncertainties or background signal levels. This is particularly evident at $X = 0.0$ and 0.1 cm. The channel A Raman signal ranges from 0.32 at 300 K to 0.60 at 2,000 K of the channel B Raman signal. Since the background signals are very similar, the channel A background-to-total signal ratio given in Figure 19 is the larger of the two channels.

The importance of the Poisson uncertainty in evaluating dynamic measurements of a variable can be seen in several ways. Effectively, when the bin width is approximately equal to the Poisson uncertainty, the histogram will have only five significantly populated bins when the uncertainty due to

72
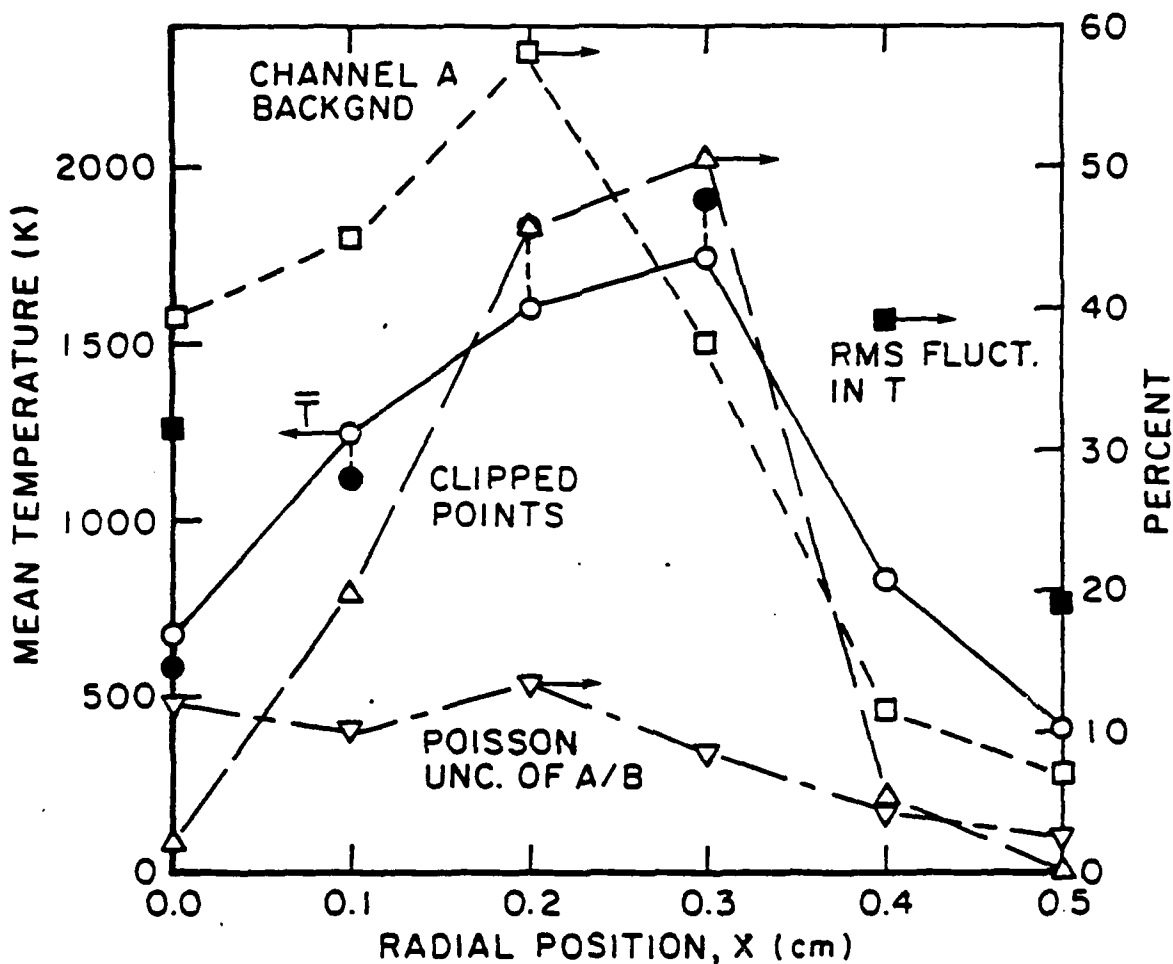
Figure 19. Radial Profile Plots for the Methane Diffusion Flame at Z = 2.5d. [○ - Mean Temperature for 20-Hz Read Rate; ● - Mean Temperature for 1.25-Hz Read Rate; □ - Channel A Background Signal as a Percentage of the Total Signal; △ - Number of Reads Clipped at 2250 K as a Percentage of the Total; ▽ - Percent Poisson Uncertainty in the Raman Signal Ratio Given by Equation (34); and ■ - The RMS Temperature Fluctuations as a Percent of the Mean (see text).]

fluctuations in the measured variable is small compared to the Poisson uncertainty. This is clearly seen in a typical calibration histogram shown in Figure 20 where the bin width and both the Poisson and measured uncertainties are all 10 K. In this case, the three central bins contain 85% of the events. Thus, this bin width represents a convenient resolution of the distribution function for revealing the characteristics of the fluctuations in the variable being measured. In effect, the measuring process of photon counting introduces intrinsic fluctuations related to the magnitude of the count accumulated over the measurement interval which is superimposed on the fluctuations of the measured variable.[12,37,38] For the contributions of these fluctuations to be visible in the histogram, the measured variance of the data must be larger than the Poisson variance. The degree of visibility depends on the difference between these variances. Use of the Poisson bin width increases the possibility that features much in excess of three bin widths are largely due to the fluctuations of the variable.

The shapes of the pdf's in Figure 17, therefore, can be understood in terms of the combination of the distribution function due to the Poisson process and the true distribution function of the temperature. At positions $X = 0.0$, 0.4, and 0.5 cm, the flowfields are made up of essentially nonreacting gases (as indicated by the small or absent 2250K bins) involving strongly fluctuating temperatures. The resolution of these fluctuations is determined by the Poisson uncertainties which are 320, 115, and 24K respectively for $X = 0.0$, 0.4, and 0.5 cm for the plots in Figure 17. It is significant that the main difference between the pdf's at $X = 0.0$ and $X = 0.4$ cm is that the latter plot is shifted up by about one-half the bin width. This is reasonably consistent with the mean temperatures at the two positions. However, even though the Poisson uncertainty in the $X = 0.0$ plot is 1.6 times the bin width, the plot has a shape very similar to the higher temperature plot at $X = 0.4$ where its Poisson value is 0.58 of the bin width. The implication is that the observed
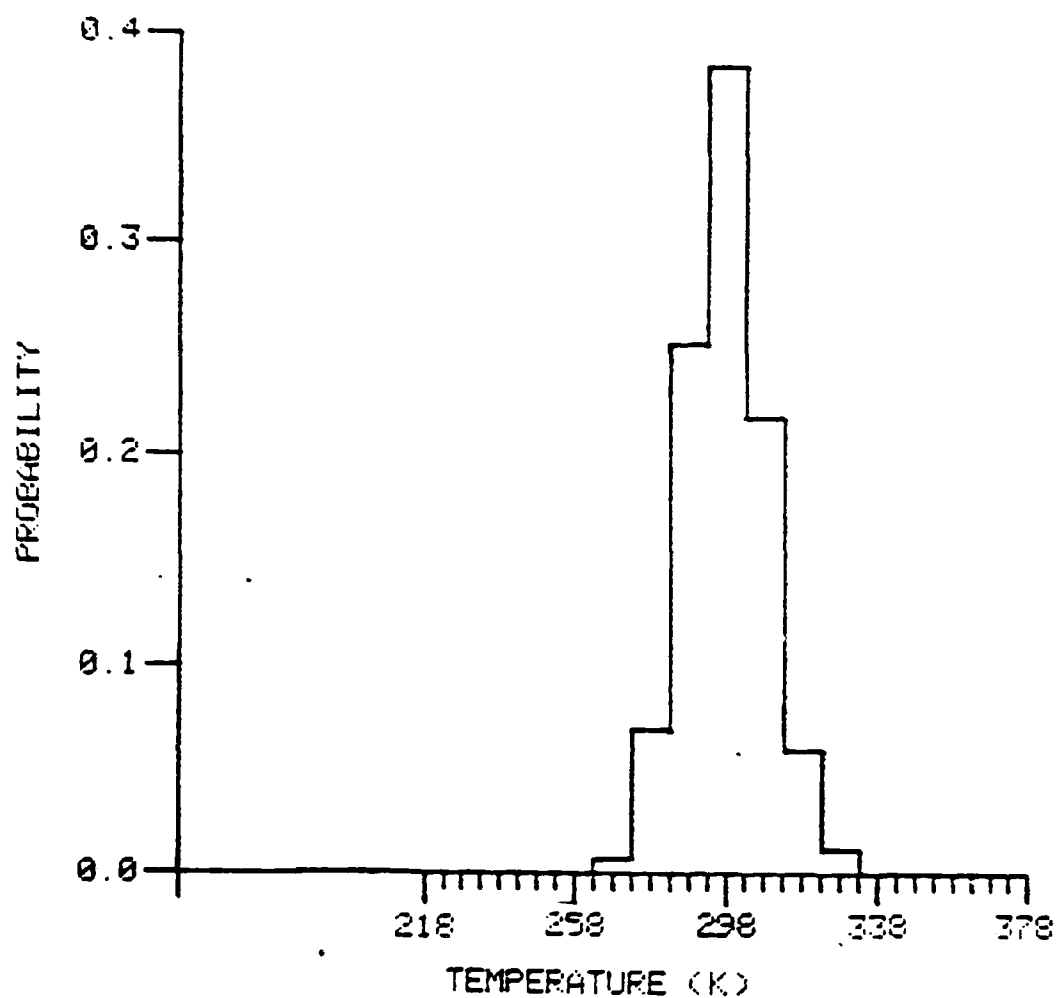
Figure 20.   Temperature Probability Histogram for a Typical Room-
             Temperature Calibration in Air. [Data record was for
             1024 reads at a 20-Hz read rate. The bin width
             equals the Poisson uncertainty which equals tne
             measured standard deviation (10 K).]

75

shape is a combination of the true distribution of temperature and a contribution due to the Poisson distribution.

The shape of the temperature distributions for X = 0.0 and 0.4 cm in Figure 17 also appears in the data for X = 0.5 cm given in Figure 21(a). This histogram was obtained using original read rate of 100 Hz. The bin width is equal to the Poisson uncertainty corresponding to 57 K. The pdf is obtained by dividing the probability bin height by the bin width. The N_2 concentration pdf was also determined by using Equations (20) and (21) with the more intense 3-channel data. This is given in Figure 21(b) for the reduced read rate of 25 Hz. The lower read rate reduced the Poisson uncertainty to 9.4%. Since this is only slightly smaller than the observed 11.3% standard deviation in the data, a bin width equal to one half the Poisson value was used to reveal the shape.

The shape of the temperature pdf's can be understood from the realization that the ideal gas law given by Equation (6) establishes an anticorrelation between temperature and total number density when the pressure is constant. Thus, in the absence of combustion and for subsonic flows, if the density distribution is known, it is straightforward to compute the temperature distribution. Figure 21(b) clearly suggests that a Gaussian distribution would be a good starting point. This is supported by the concentration measurements of CO_2 and air described in the next section. Therefore, by assuming the pressure is constant and doing a coordinate transformation using Equation (6), (where p is now the total pressure) we can obtain the temperature pdf.[9,39] An example of this calculation is given in Figure 22(a) for a 40% standard deviation in density and a mean temperature of 600 K. Clearly, the shape of this plot is quite similar to that in Figure 21(a) and has a positive skewness similar to the pdf's in Figure 17. A more dramatic matchup with the theoretical pdf is given by the X = 0.0 pdf plotted in Figure 22(b) using a narrow bin width. If the
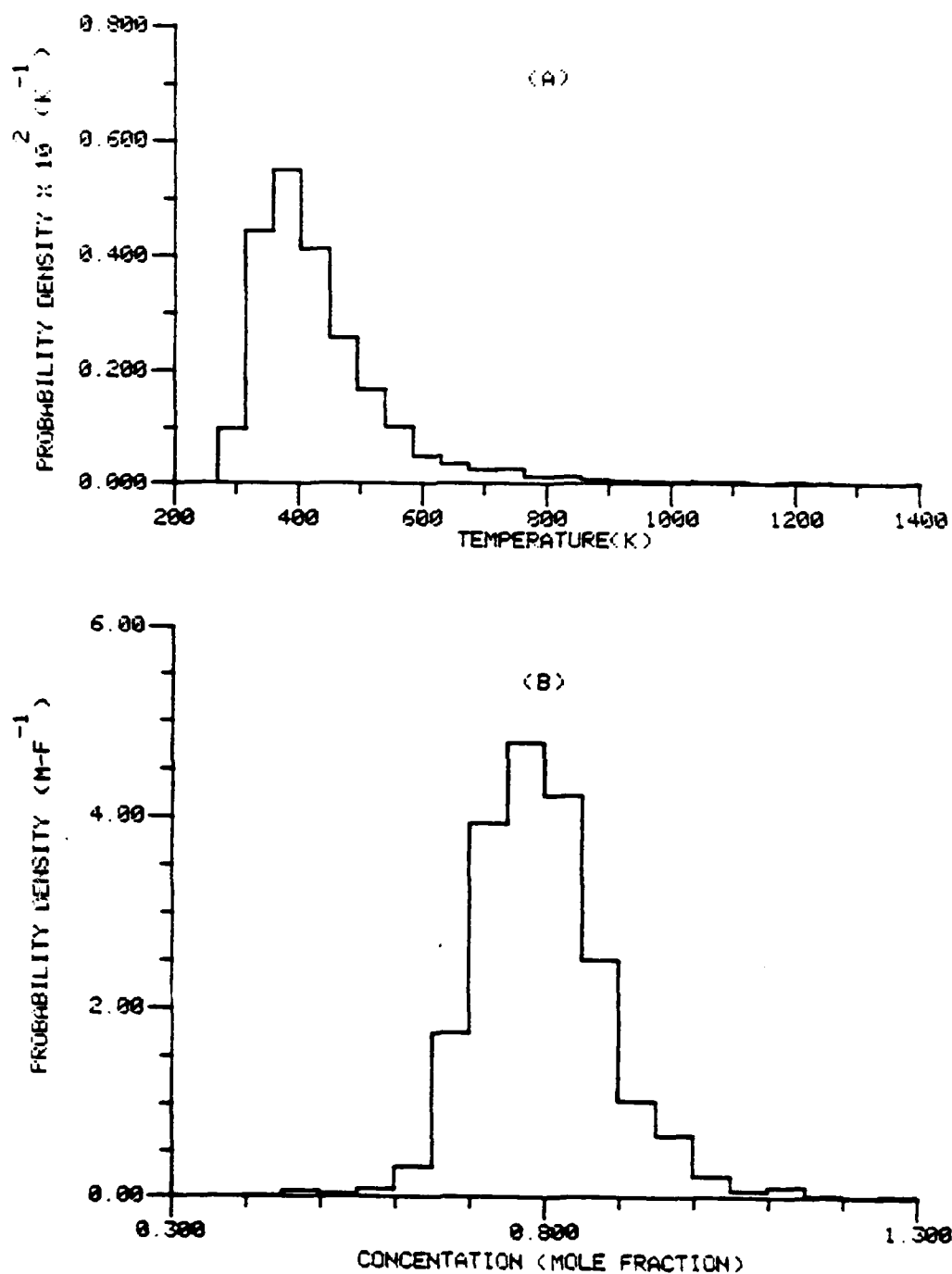
Figure 21.   Temperature and N_2 – Concentration PDF's for the
Methane Diffusion Flame Obtained from Simultaneously
Recorded Data at X = 0.5 cm (7.14r) and Z = 2.5d;
(a) Temperature PDF. (Bin width equals the Poisson
uncertainty. Read rate was 100 Hz.); (b) N_2 –
Concentration PDF. (Bin width equals one half the
Poisson uncertainty. Read rate was reduced to
25 Hz.)

77
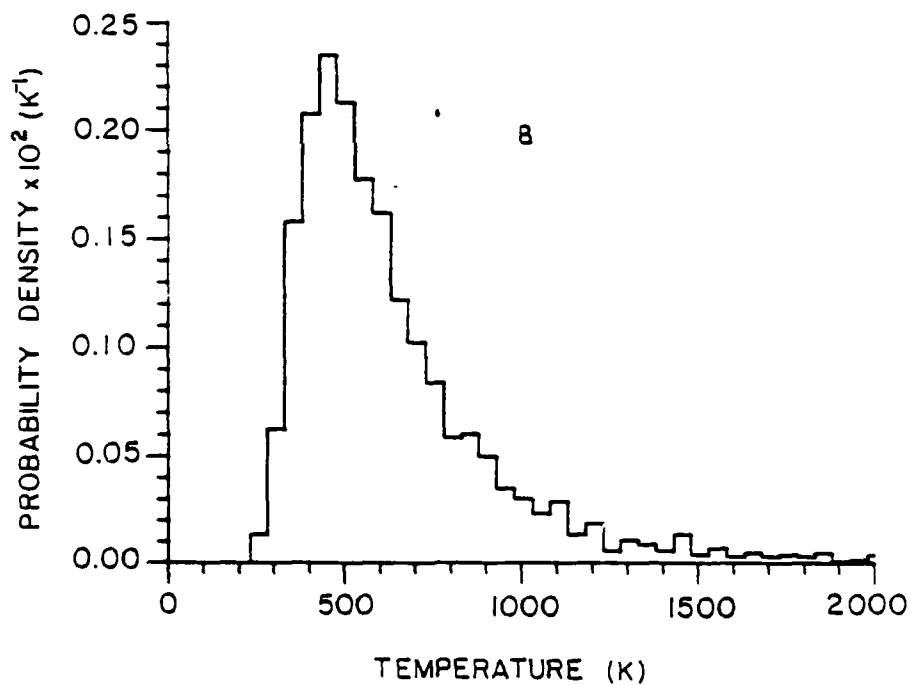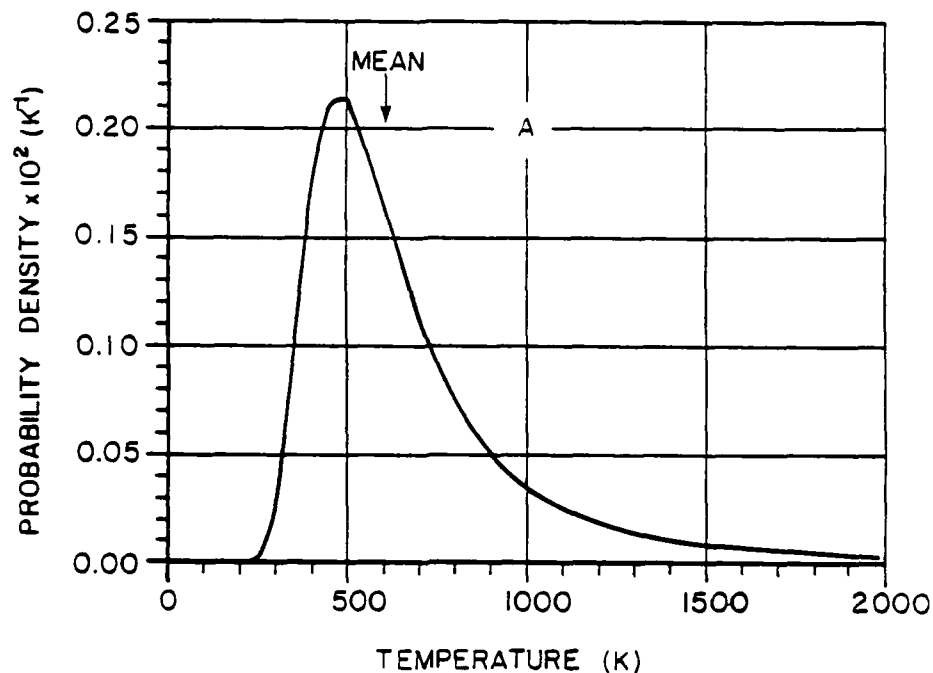
Figure 22. (a) Calculated Temperature PDF for an Ideal Gas at
Constant Pressure Having a Gaussian Density
Distribution with a 40% Relative Standard Deviation
and a Mean Temperature of 600 K.
(b) Experimental Temperature PDF for the Methane
Diffusion Flame On-Axis at Z = 2.5d. (Data record
was for 2048 reads at a read rate of 20 Hz. Minimum
bin width was used.)

78

2,250 K bin in Figure 17 is deleted, the mean temperature is
640 K with a measured standard deviation of 48%. These values
are reasonably consistent with the parameters used to plot Figure
22(a).

To evaluate this result we first note that the X = 0.0 data
were taken within the potential core of the flow. The histogram
in Figure 17 supports the expected near absence of combustion by
the small size of the 2,250 K bin. The high Poisson uncertainty
for this plot was due to the low N_2 concentration in this region,
whereas the X = 0.5 data were taken outside the flame front in
a region of high N_2 concentration, thereby giving a small Poisson
value, even with the higher read rate of 100 Hz. Two effects
contribute to the commonality of these data acquired from such
different regions. These are the Gaussian or near-Gaussian
character of the total number density pdf and the essentially
Gaussian character of the Poisson distribution of the photon
counting process.[26] Effectively, both processes contribute to
the same observed shape. How much of the pdf is attributable to
the temperature fluctuations can be measured using a "derived"
varia᛫ obtained by subtracting the Poisson variance from the
variance of the data. The resulting rms values are given in
Figure 19 as solid squares. The values obtained for the X = 0.0
and 0.5 cm data are respectively 32% and 18%. The corresponding
measured standard deviations are 57% and 19%. Clearly about 30%
of the observed distribution in Figure 22(b) is attributable to
actual temperature fluctuations while 90% of the pdf in Figure
21(a) is due to the actual fluctuations.

4.1.2.2 Spectral and Correlation Analyses

A common and well-established technique for analysis of
noise involves the determination of either the power spectral
density function (psdf) or the correlation function (acf), or
both. Useful representations of these functions are derivable
from real-time data when the read rate is higher than twice the
maximum frequency contained in the data and (very important) when

the number of measurements is very large. The latter condition can easily be fulfilled by the TiLaRS system while the former condition could only be fulfilled in the flame studies where excessive clipping was not needed. As discussed in the preceding paragraphs, this restriction was due largely to the $\Delta J = 3$ limitation imposed on the Raman line pair by the spectrometer. The need for large numbers of measurements was discussed in Section 3.3. To achieve any degree of precision in characterizing a psdf or an acf, say 10%, each point in the domain of these functions must result from an average of at least 200 measurements or reads. For example, if a spectrum out to 100 Hz with a resolution of 1 Hz is desired, more than 20,000 simultaneous reads in each channel are needed. At the minimum required read rate of 200 Hz (Nyquist frequency), this would take over 100 seconds of continuous data recording. Since we were limited to 4,096 reads per channel by the minicomputer memory, this kind of requirement was met by dividing the record into overlapping segments of equal lengths.[34] The psdf's calculated from these segments were then averaged to obtain a function with a relatively reduced "noise" level. The difficulty with this technique, aside from the lack of complete independence of the overlapping segments, is the loss of resolution. This turned out to be a problem in the psdf's studied here because of the need for low-frequency resolution. For example, if the 200-Hz read rate was to be used with 4,096 reads, then one could choose 31 one-half-overlapping segments with 256 points each to give a signal-to-noise (S/N) ratio of $\sqrt{31} = 5.6$ and a resolution of $100/128 = 0.78$ Hz (the positive frequencies use half the points). If higher resolution was needed, then 13 three-quarters-overlapping segments with 1,024 points each can be used. This gives a resolution of 0.195 Hz with S/N = 3.6. Clearly, there is no substitute for large quantities of data.
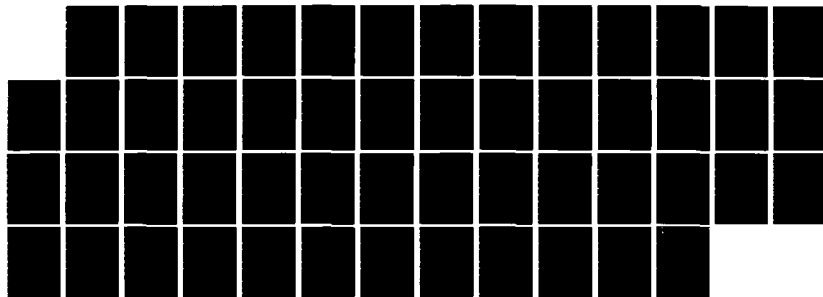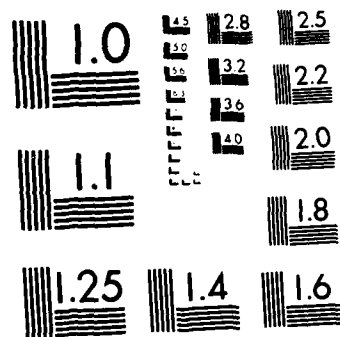
MICROCOPY RESOLUTION TEST CHART

NATIONAL BUREAU OF STANDARDS-1963-A

Another point of importance in these analyses is the
question of aliasing.[9,33,34] When the signal being sampled
contains frequencies f higher than one half, the sampling
frequency or read rate f_r, frequencies consisting of sums and
differences of f with the harmonics of f_r are generated. These
"alias" frequencies show up in the observed spectrum and
therefore constitute errors in the measurement. This result
assumes essentially synchronous, instantaneous sampling of the
signal as one might do in an analog measurement. In the
measurements reported here, the recorded signal is the total
count accumulated over the read interval Δt; therefore it is a
time-averaged measurement. As a result, frequencies higher than
$f_r/2$ are averaged out. It is easy to show that the net amplitude
contributed to each read interval by these signals is attenuated
according to f_r/f. The corresponding power is then attenuated by
$(f_r/f)^2$. This result applies to spectral features of finite
bandwidth. For a constant power spectrum as produced by "white
noise", the time averaging causes the alias noise due to
frequencies greater than $f_r/2$ to be folded back into the observed
spectrum such that the observed spectrum shows no attenuation.
Moreover, the observed spectrum is a consistent representation of
the spectral density of the white noise.

The runs at $X = 0.0$, 0.4, and 0.5 cm had small enough
clipping to permit psdf's and acf's to be determined. The psdf's
were obtained by squaring the magnitude of the Fourier transform
coefficients generated by a FFT routine. Since the read rates
for the $X = 0.4$ and 0.5 data were respectively 50 and 100 Hz,
then the spectra were calculated out to the Nyquist frequency,
namely 25 and 50 Hz. The spectra for these two runs are shown in
Figure 23. The $X = 0.4$ data were segmented in 15 one-half
overlapping records of 512 points each, while the $X = 0.5$ data
were divided into 13 three-quarter overlapping segments of 1,024
points each. These choices provide the same resolution of
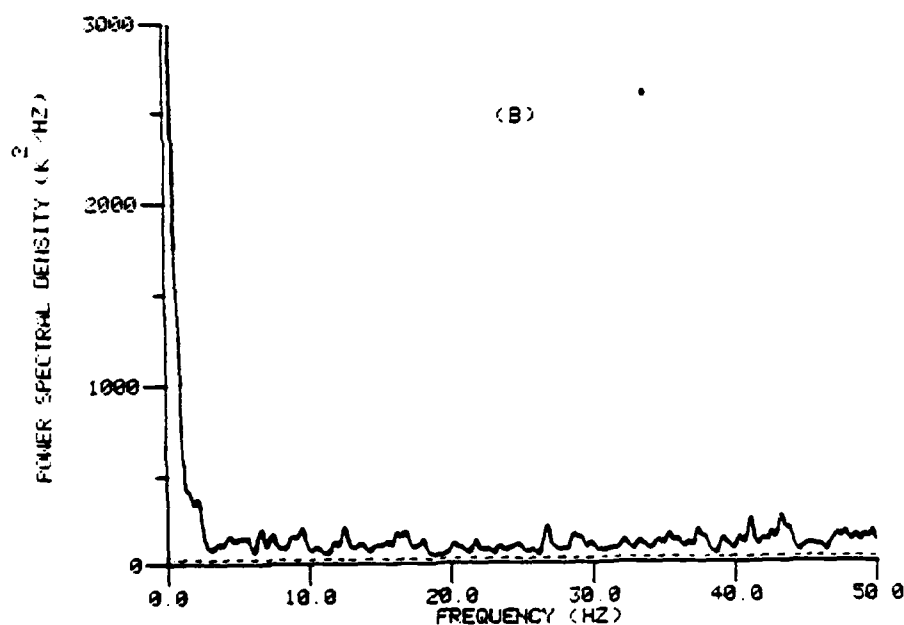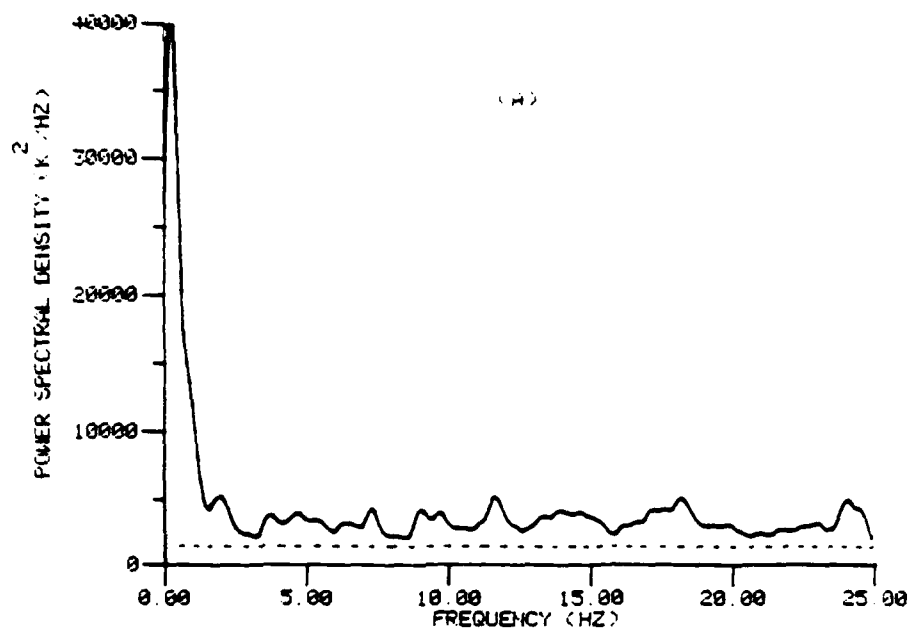
Figure 23. Temperature PSDF's for the Methane Diffusion Flame at Z = 2.5d; (a) For X = 0.4 cm (5.71r) and Average of 15 One-Half Overlapping Segments of 512 Points Each; (b) For X = 0.5 cm (7.14r) and Average of 13 Three-Quarter Overlapping Segments of 1024 Points Each. (Spectra were smoothed with a cosine filter of 0.7 Hz bandwidth. Dashed lines identify the "Poisson noise" levels.)

82

0.098 Hz. The spectra were smoothed with a cosine filter of
0.7-Hz bandwidth.

The dashed lines in Figure 23 identify the power spectral
densities due to the "Poisson noise" arising from the photon
counting process. These spectra give the total power summed over
both positive and negative frequencies. Hence, the Poisson level
is computed by taking the Poisson variance and dividing by the
bandwidth of the spectrum. As can be seen in Figure 23, the
spectra show an additional "white noise" contribution plus a
low-frequency feature. This feature has been consistently
observed in the temperature psdf's of earlier flame
measurements.[18] So far, it has been observed only near the flame
front and gets stronger as the front is approached. The psdf's
of the concentration data of these runs as well as the
temperature psdf at X = 0.0, do not show any low frequency
feature of this sort. The spectrum of the X = 0.0 data is given
in Figure 24. It was obtained using 15 segments of 256 points
each and a 0.7 Hz filter. The 20-Hz read rate limits the maximum
frequency to 10 Hz.

The low-frequency feature is clearly seen in 0 to 5 Hz
spectra given in Figure 25. These spectra were fitted to the
power spectral density function that can be described as white
noise passing through a low-pass filter.[9] This function can be
written as

$$G(f) = K_G/[f^2 + (1/2\pi t_c)^2]$$ (41)

where K_G and t_c are the constants which were fitted to the data.
The plots in Figure 25 show the resulting fits as solid points.
The short dashed lines indicate the total white noise level
estimated from the corresponding plots in Figure 23. These fits
permitted the total variance due to the "$1/f^2$" spectrum to be

83
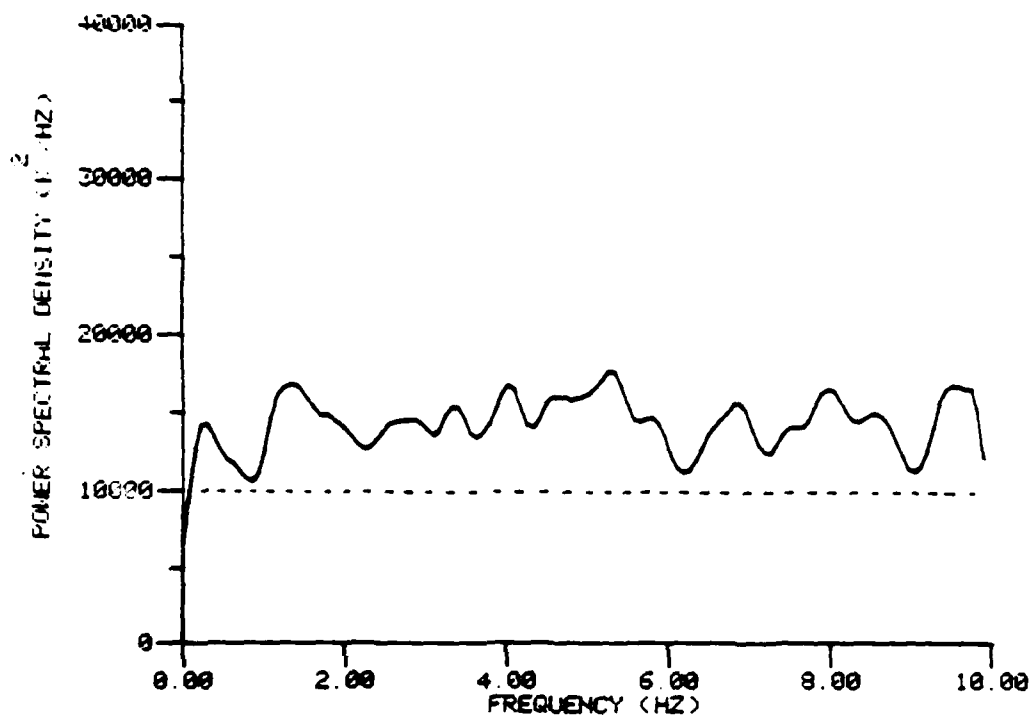
Figure 24. Temperature PSDF for the Methane Diffusion Flame On-Axis at Z = 2.5d (Averaged over 15 segments of 256 points each and a 0.7-Hz smoothing filter. The dashed line identifies the "Poisson noise" level.)
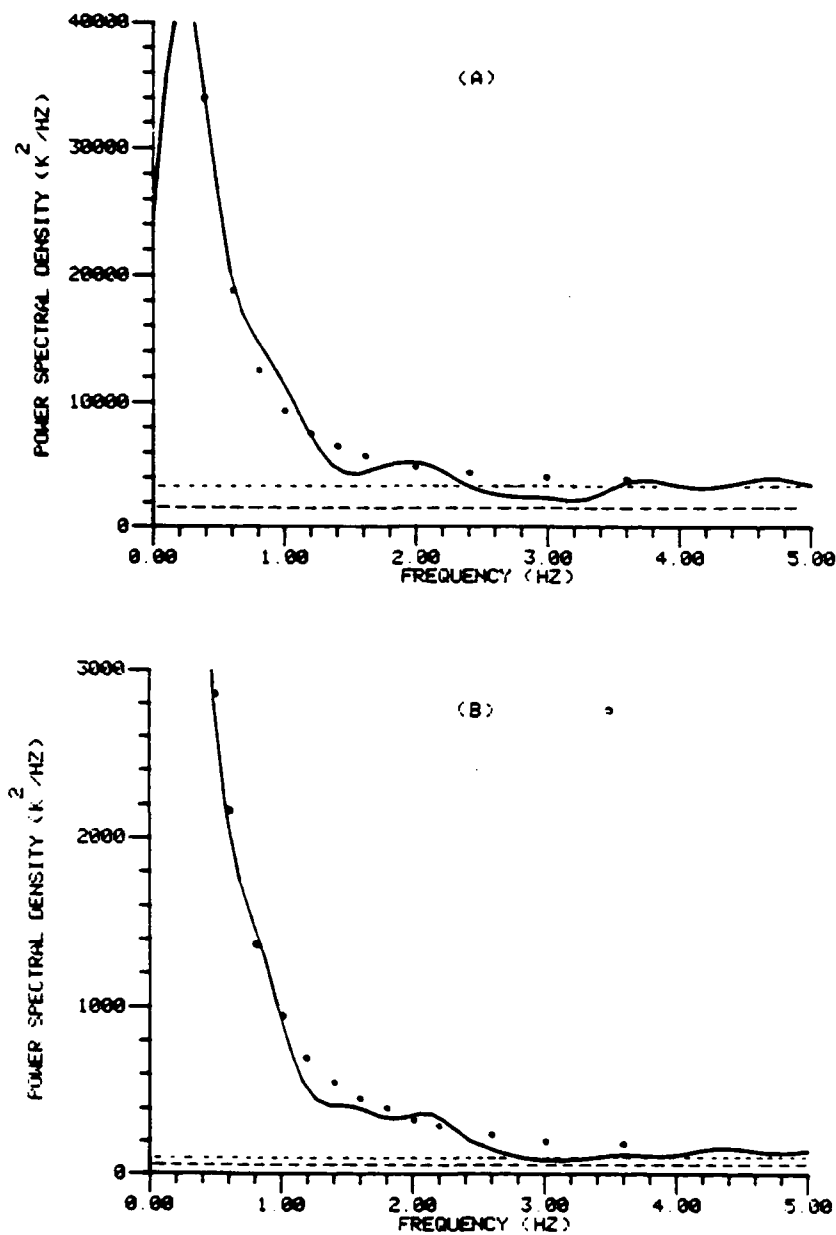
Figure 25.   Low-Frequency Regions of the PSDF's Given in Figure
             23 Showing Fits of "$1/f^2$" Spectra; (a) X = 0.4 cm,
             (b) X = 0.5 cm.   (Dots are the calculated fits, the
             short dashed lines indicate the estimated total
             "white noise" levels, and the long dashed lines iden-
             tify the Poisson levels.)

85

computed. Subtracting this and the Poisson variance $s_p^2 = G_p f_r/2$ from the observed variance, the non-Poisson or "thermal" white noise level G_T could be found. These results are summarized in Table 2.

TABLE 2

Results of $1/f^2$ Analysis of Temperature Fluctuations

X (cm)	K_G ($K^2 \cdot Hz$)	t_c (sec)	G_p (K^2/Hz)	G_T (K^2/Hz)	$C(0)$	$C_{exp}(0+)$
0.4	5,280	0.78	1,640	1,390	0.24	0.28
0.5	914	0.58	60	32	0.36	0.30

A further check on the $1/f^2$ analysis can be carried out using the acf. The acf can be obtained using the inverse Fourier transform of Equation (41).[9] This gives

$$R(\tau) = \pi^2 K_G t_c \exp(-\tau/t_c) \ . \tag{42}$$

The "acf coefficients" for the X = 0.4 and 0.5 data obtained by normalizing the acf's against the observed total variances s_{tot}^2, are plotted in Figure 26. These curves show an exponential-like decay with time constants consistent with the values of the integral time scale t_c given in Table 2. The values at one read interval greater than $\tau = 0$ in Figure 26 given by $C_{exp}(0+)$ in Table 2 also compare favorably with the acf coefficients computed from $C(\tau) = R(\tau)/s_{tot}^2$. However, the acf's show additional low-frequency features which distort the decay curves. Since these features depend on the segmenting procedure, it is assumed that they are caused, at least in part, by slow "trends" in the data records. The acf coefficients given in Figure 26 are averages of eight nonoverlapping segments with 512 points each. The current

86
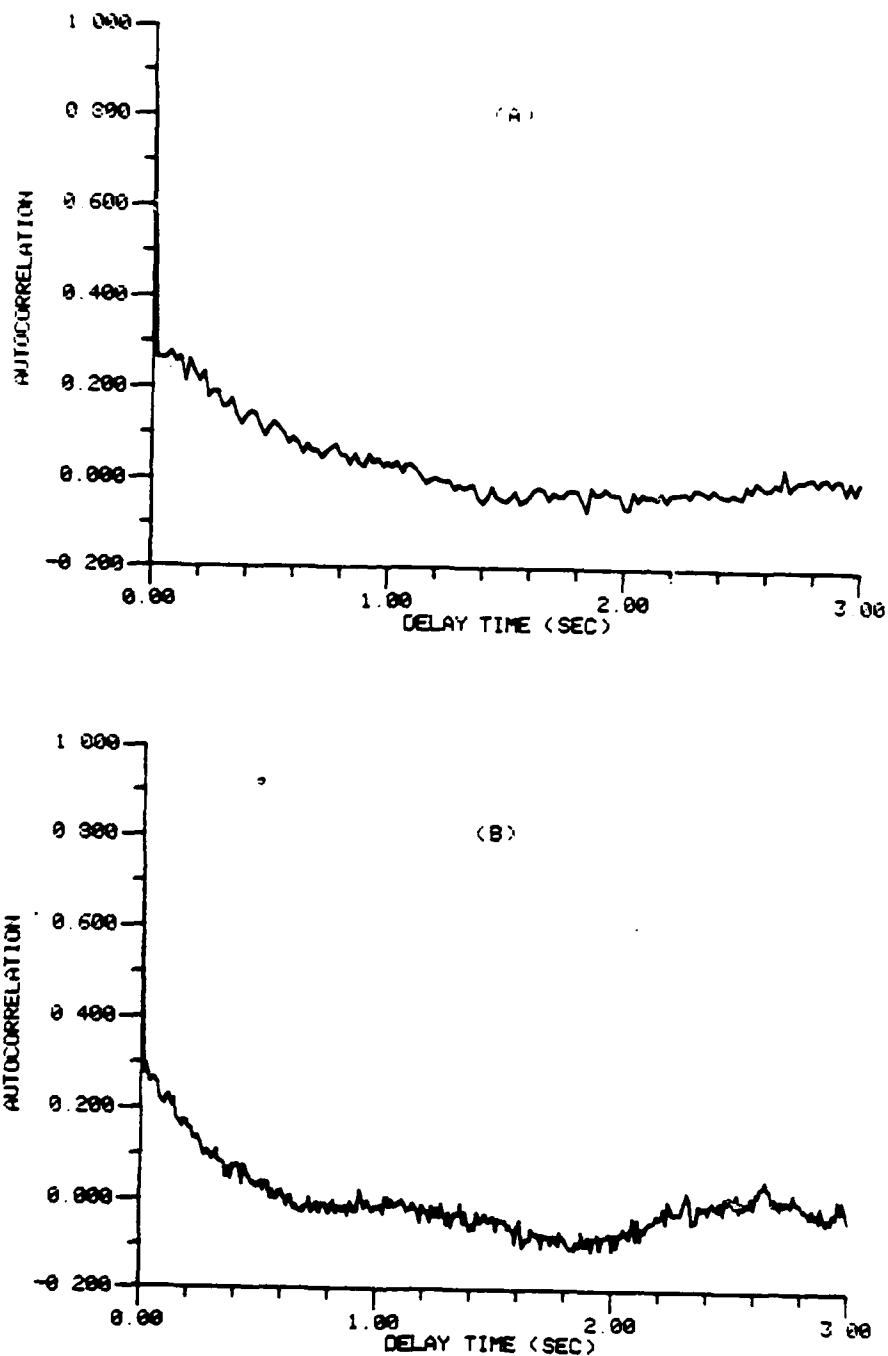
Figure 26. Temperature Autocorrelation Coefficients for the Methane Diffusion Flame at Z = 2.5d; (a) For X = 0.4 cm (5.71r); (b) For X = 0.5 cm (7.14r). (Averaged over eight nonoverlapping segments of 512 points each.)

software permits only the removal of the average of the data in the segment. What is needed is a polynomial fit to the data, perhaps up to third order, which is then subtracted before analysis. It should be noted here that $1/f^2$ behavior does not depend on segmenting or read rate.

Finally, Figure 26 also shows that the white noise identified in Figure 23 can be associated with a correlation time less than the resolution times in Figure 26. The resolution times in Figures 26(a) and (b) are respectively 20 and 10 msec. Part of this "fast" correlation is due to the uncorrelated detection noise which gives the Poisson variance while the origins of the remaining "fast" component can be associated with G_T in Table 2.

4.2 CARBON DIOXIDE JET STUDIES

Concentration measurements at constant temperature using RS are a straightforward application of Equations (1) and (2) which express the fact that the Raman count rate $\dot{n}_J$ is directly proportional to the molecular concentration N provided that the parameters of the measuring system are held constant. The essential parameters appearing in Equation (20) that are subject to variations are the wavelength setting, temperature, calibration constant, and laser power. Since mole fraction c is the preferred measured variable, the atmospheric pressure in Equation (21) must also be constant, or at least known. The objective of these studies was to make dynamic measurements of the fluctuations of the CO_2 and air mole fractions in a room temperature CO_2 jet.

4.2.1 Setup and Calibration

The studies were carried out using the same basic gas flow apparatus used in the CH_4 flame studies with the following exceptions. The nozzle was an ASME flat-top velocity profile, stainless steel nozzle with an orifice diameter of 4.77 mm. The nozzle was mounted on a 9-cm diameter aluminum disk so that the

face of the nozzle was flush with the outer surface of the disk. The exhaust pipe and mounting hardware used with the flame were removed. The flow rate of the "bone-dry" CO_2 gas (supplied in liquified form) was measured using a Fischer and Porter ball-in-tube flow meter. The pressure regulator which supplied that flow meter was preceded by an in-line gas heater. This heater was needed to offset the Joule-Thomson cooling of the CO_2 gas when it expanded in the regulator.

The flow meter calibration curve for CO_2 which was specified to be good to $\pm 3\%$ by the manufacturer was checked twice against the flow meter in the Room 20 test facility in Building 18 at W-PAFB operated by the Aero Propulsion Laboratory (APL). The first calibration was in reasonable agreement with the manufacturer's curve being high 2.4% at 2.0 kg/h and low 1.4% at 6.0 kg/h mass flow. In the second calibration, the curve value was only 0.3% high at 2.0 kg/h while the 6.0 kg/h flow rate showed a -6% discrepancy on the flow meter. The source of this latter disagreement at 6 kg/h was not resolved; however, the overall results suggest that the $\pm 3\%$ uncertainty is a reasonable assignment to the calibration curve.

The rotational RS lines of CO_2 are spaced 3.12 cm^{-1} compared to the 7.96 and 11.5 cm^{-1} spacings respectively of N_2 and O_2. The spectrum of CO_2 scanned with relatively narrow slits (80 μm) is given in Figure 27. With wider slits, such as 150 μm used in these CO_2 studies, there is no wavelength in the 0-to-70 cm^{-1} region shown in Figure 27 where CO_2 is not detected. It is fortunate that the strongest line in the spectrum of air occurs exactly at the minimum between two CO_2 lines. This line is at 60 cm^{-1}, shown in Figure 2, and is due to the near coincidence of the $J = 6$ line of N_2 and the $J = 9$ line of O_2. Similarly, the $J = 24$ line of CO_2 is located within the gap between the $J = 5$ line of O_2 and the $J = 4$ line of N_2 and it is well within the 29-cm^{-1} spacing limit from the 60-cm^{-1} air line imposed by the spectrometer exit slit. The optimum choice for the CO_2 line based on its intensity would be the $J = 18$ line situated between
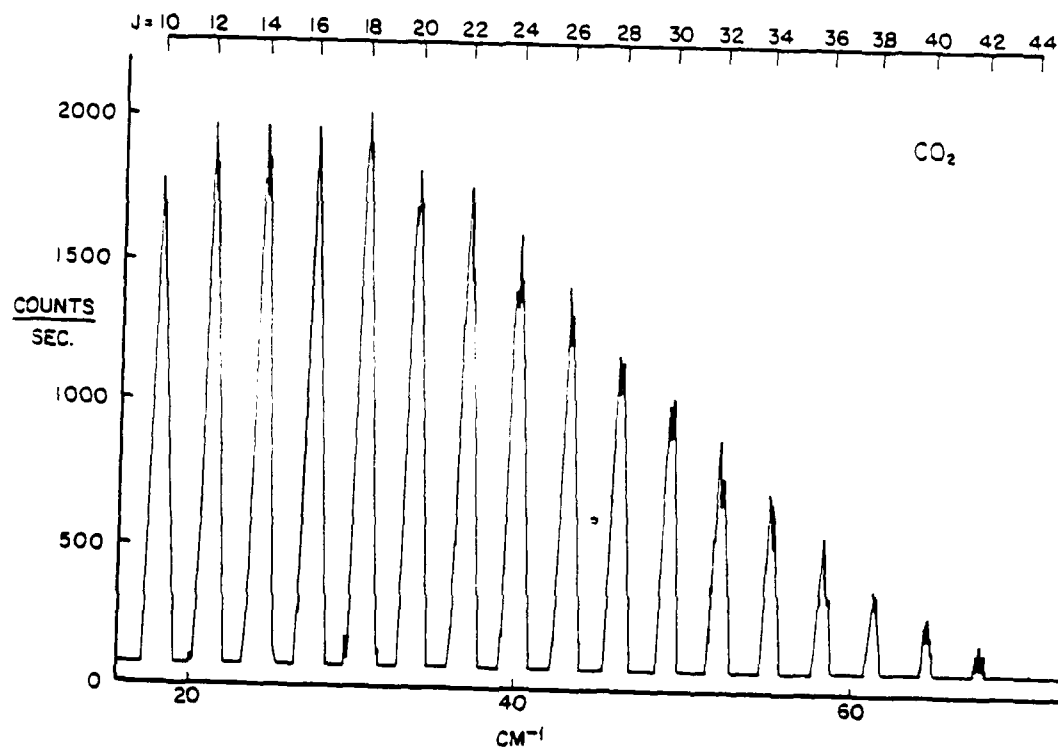
Figure 27. Observed Stokes Rotational Raman Spectrum of One-Atmosphere, Room-Temperature Carbon Dioxide for a Single Pass of the 2W, 488 nm Laser Beam. Right angle geometry was used with perpendicular polarization. The input image was slit limited where the slits were 80 μm wide by 10 mm high.

the $J = 2$ and $J = 3$ lines of N_2. In fact, both the $J = 13$ and 20
lines could be measured together using a wide slit on that
channel. However, as indicated above, the spacing from the
60-cm^{-1} "air" line is too large.

Ideally, a narrow slit, say ~ 100 μm or less, would be pre-
ferred because it would reduce the interference of CO_2 in the air
channel. A narrow slit was precluded, however, by the fact that
it would introduce slit-limited illumination of the entrance slit
due to the ~ 80-μm wide laser beam image. This is undesirable
because of the slight movements of the image on the entrance slit
due to schlieren effects produced by the jet. Such movements in
slit-limited illumination creates signal fluctuations superim-
posed on the fluctuations of the molecular concentration. The
150-μm slit width was considered the best compromise.

The scans taken over the CO_2 and air spectra with the two
channels using this slit width are shown in Figure 28. These
spectra reveal the source·of a major difficulty encountered
in this work. Because of the narrow slit, the degree of
"flatness" of the peaks of the two lines is very small if there
is any flatness at all. This is especially true, as can be seen
in Figure 28 for channel A. The 60-cm^{-1} "air" line has a sharper
peak than the CO_2 lines because of the 0.37 cm^{-1} (0.009 nm or
0.09 Å) mismatch between the N_2 and O_2 lines which make up this
air line. This is in contrast to the nearly flat-topped N_2 lines
shown in the spectrum in Figure 14, which was obtained with
300-μm slits. This flatness provided a degree of insensitivity
to slight drifts in the spectrometer wavelength setting in the
CH_4 flame studies. When the narrower slits were used, these
slight drifts made a significant change in the effective calibra-
tion of both channels. The drifts were caused by slow changes in
the internal temperature of the spectrometer. This problem was
not identified early enough to allow it to be corrected before
the completion of this program. Fortunately, calibration runs
were made at the beginning and end of the series of runs on the

91
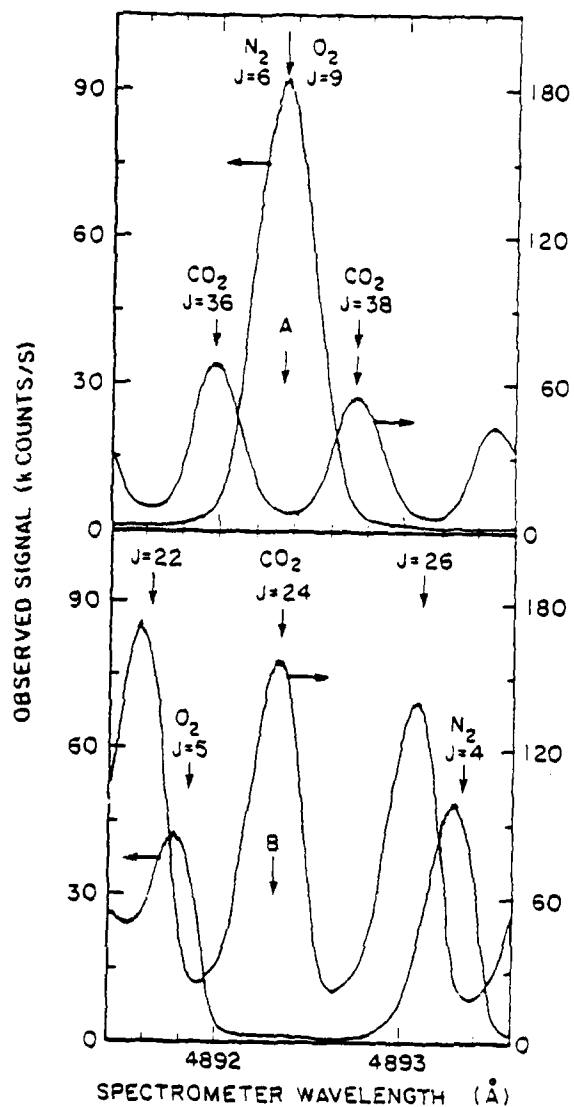
Figure 28. Superimposed Scans of ~100% Air and ~100% CO_2 at Room Temperature and Pressure. (Conditions were same as in Figure 14 except the exit slit width was 150 μm and the slit height for CO_2 was at 1 mm. See Figures 2 and 27.)

92

CO_2 jet. This provided a reasonable basis for compensating for the calibration shift.

The symmetric, sharp line shapes of the second-order spectra in Figure 28 are evidence for the good performance of the dual-channel, exit-slit optical system. The measured CO_2 line widths (fwhm) are 0.034 nm (1.42 cm^{-1}) while the 60-cm^{-1} air line is 0.038 nm (1.59 cm^{-1}) wide. The estimated minimum line width in the exit slit plane for an 150-μm exit slit and the 80-μm wide image width of the source using Figure 12 is about 0.027 nm. Since the scans in Figure 28 were all carefully started at the same wavelength, this figure also shows the good matchup of the channel settings with the peaks of the two lines. Recognizing that the CO_2 scans in Figure 28 were taken with a ~1-mm-high slit while the air spectra were taken with a 2-mm-high slit, the CO_2 interference shown in channel A in the figure is consistent with the 14.1% measured value.

The calibration for these studies was accomplished by first bringing the system to operational status using the system parameters intended for the experiments. The count rates were then measured in each channel when a known concentration of the appropriate gas was present in the observed volume. The calibration constants $\dot{n}_{Ar}$ and $\dot{n}_{Br}$, determined by applying Equation (24) to the observed calibration count rates, were then used in Equation (22) and (24) to determine the dynamic values of the mole fractions of the two gases from the measurements. For the CO_2 calibration, the nozzle orifice was centered on the observed volume and set about 1 mm away in the axial direction (i.e., Z direction). A low CO_2 flow rate was established to displace the air completely from the observed volume and the calibration was carried out. The CO_2 calibration constant $\dot{n}_{Br}$ for the J = 24 line was found to be 355.4 kcounts/s ±0.1% using 5.0 W laser power and a 1-mm-high by 150-μm-wide entrance slit. The other channel was positioned on the 60-cm^{-1} "air" line. This "mixed" line characterizes 99.0% of the composition of air. Because of

93

the similarity of the masses and viscosities of O_2 and N_2 at room temperature,[40] it is suggested that the small differences in the molecules would not be sufficiently important, at least in these preliminary studies, to offset the advantage of using the strong "air" signal provided by this line. The air calibration constant $\dot{n}_{Ar}$ was found to be 106.0 kcounts/s $\pm 0.05\%$ obtained with the conditions cited above. The uncertainties in the measurement of these constants were the observed standard deviations (essentially the same as the calculated Poisson uncertainties) divided by the square root of the number of measurements or reads.

4.2.2 Data and Results

Three sets of runs were carried out on the CO_2 jet. The first two were axial (Z-direction) profiles at 2.0 and 6.0 kg/h and the third was a radial (X-direction) profile at 6 kg/h. The axial runs extended from 0.3 (0.63d) to 14.0 cm (29.4d). The radial runs covered the range from 0.0 to 1.0 cm (4.2r) at the Z = 2.0 cm (4.2d) position. The maximum axial position was restricted to 14.0 cm due to a minor mechanical interference which has since been removed. The disappearance of the CO_2 signal determined the maximum radial position. The axial position in the radial set of runs corresponds approximately to the end of the potential core region. The Reynolds numbers Re were 10,000 and 30,000 respectively for the 2.0 and 6.0 kg/h flows.

The data were reduced to profiles of the mean concentration, relative rms concentration fluctuations, and the covariance of the concentrations of the two gases. In addition, where the signal levels were appropriate, auto-correlation functions (acf's), cross-correlation functions (ccf's), power spectral density functions (psdf's), the skewness β_3 and the kurtosis β_4 of the concentration distributions were obtained. All of the data were analyzed in terms of either mole fraction referred to the number density given by the gas law or the corresponding mole percent. If we neglect the trace constituents in air and assume that N_2

94

and O_2 are indistinguishable, then the sum of the air and CO_2
mole fractions will be unity. Actually, this is exact in the
limit of pure CO_2, whereas the sum is 1.?? in the limit of pure
air. Thus, one check on the accuracy of the data is in the
closeness of this sum to unity.

Once the calibration bias mentioned in the previous section
was corrected, the CO_2 data needed no further manipulation.
However, the apparent air concentration determined from channel-A
included a signal due to CO_2 which equaled 14.1% of the CO_2 con-
centration measured in the channel B. This correction was
applied to the channel A data on a point-by-point basis. It was
determined by assuming that the apparent air concentration c_A in
channel A is a linear combination of the true air concentration
c_c and a constant fraction Δ_A of the CO_2 concentration c_C
measured in channel B. The relation expressing this assumption
is $c_a = c_A - \Delta_A c_C$. The fraction was found by observing that the
mean air signals on axis at $Z = 0.3$, 0.5, and 1.0 cm were essen-
tially zero, that is $\langle c_a \rangle = 0$, and averaging the three values of
Δ_A computed from the data for these three positions. The
resulting corrections applied to the channel A data brought the
sum of the mean concentrations for the radial profile to within
an average deviation of 0.9% from the desired 100% value. The
results for the axial profiles were somewhat poorer, especially
for the 10.0 and 14.0 cm measurements which gave sums of ~95%.
The average deviations from 100% for the 2-kg/h and 6-kg/h axial
data sets were respectively 2.4% and 1.7%.

Corrections also had to be applied to the Poisson uncertain-
ties calculated for channel A, due to the need for subtracting
out the CO_2 interference. The Poisson uncertainty in the mole
fraction of air is given by

$$s_a = \sqrt{f_r \left(\frac{\bar{M}_A}{\bar{n}_{Ar}^2} + \Delta_a^2 \frac{\bar{M}_B}{\bar{n}_{Br}^2} \right)} \, , \qquad (43)$$

95

where it is assumed that the background measurements were made at low read rates such that $f_b/f_r \leq 0.1$. If the backgrounds are weak compared to the Raman signals, the $\dot{M}$'s can be replaced with the $\dot{n}$'s as given by Equation (24). The mole fraction Poisson uncertainty for the CO_2 measurements has the same form as Equation (43) except that the Δ_A term is absent and B replaces A.

The fluctuations observed in the signal from a given channel consist of two parts: (a) the fluctuations in the number of photoelectrons arising from the intrinsic randomness of the photoelectric effect which obey the Poisson distribution, (b) the fluctuations in the intensity of the light incident on the PMT.[38] Thus, the measured distribution $p(M, \Delta t)$ is neither the distribution of the gas $P(c)$ nor the Poisson distribution. If the integrated photon count rate incident on the PMT in one read time interval given by $\Delta t = f_r^{-1}$ (where dead time is negligible) is W and the dark count is negligible, then the observed distribution is given by[12,37,38]

$$p(M, \Delta t) = \frac{1}{M!} \int_0^\infty (nW)^M \exp(-nW) P(W) dW, \qquad (44)$$

where n is the PMT quantum efficiency. It is straightforward to show that the moments of $P(W)$ about zero are equal to the factorial moments of $p(M, \Delta t)$ given by[38]

$$M_j = \sum_{M=0}^\infty \frac{M!}{(M-j)!} p(M, \Delta t), \qquad (45)$$

96

where $\int p(M, \Delta t) = 1$, and for example,

$$M_1 = \sum_{M=0}^{\infty} M \, p(M, \Delta t) = \langle M \rangle \qquad (46)$$

$$M_2 = \langle M^2 \rangle - \langle M \rangle \; . \qquad (47)$$

(Note that both forms $\langle M \rangle \equiv \bar{M}$ are used in this report.)
Thus,

$$M_j = n^j \int_0^{\infty} W^j P(W) dW$$

or $\qquad\qquad\qquad\qquad\qquad\qquad\qquad\qquad\qquad (48)$

$$= n^j \langle W^j \rangle \; .$$

The mole or volume fractional concentration is given, using
Equation (24), by

$$c = f_r n / \bar{\dot{n}}_r = f_r (M - b') / \bar{\dot{n}}_r, \qquad (49)$$

where $\bar{\dot{n}}_r$ is the calibration count rate corresponding to 100% con-
centration. Since $M = nW$, then the concentration pdf is

$$P(c) = (\bar{\dot{n}}_r / n f_r) P(W) \; . \qquad (50)$$

From Equations (48) to (50), we have

$$M_j = \left(\frac{\overline{\dot{n}}_r}{f_r}\right)^j \int_0^1 \left(c + b'\frac{f_r}{\overline{\dot{n}}_r}\right)^j P(c)\,dc.\qquad (51)$$

The first moment about zero gives the mean concentration (i.e., $j = 1$) from Equation (51) to be

$$\bar{c} = (M_1 - \bar{b}')f_r/\overline{\dot{n}}_r$$

or   (52)

$$= (\bar{\dot{M}} - \bar{b}')/\overline{\dot{n}}_r \ .$$

The higher central moments of P(c) can be obtained from Equation (45) using[12,37]

$$\mu_m = (f_r/\overline{\dot{n}}_r)^m \sum_{j=0}^m \frac{m!}{j!(m-j)!} (-M_1)^j M_{m-j}\qquad (53)$$

for $m \geq 2$. For example, for $m = 2$,

$$\mu_2 = (f_r/\overline{\dot{n}}_r)^2 (M_2 - M_1^2) \ ,\qquad (54)$$

which gives, using Equations (46) and (47)

$$\mu_2 = (f_r/\overline{\dot{n}}_r)^2 (\langle M^2 \rangle - \langle M \rangle^2 - \bar{M}) \ .\qquad (55)$$

98

Equation (55) shows an important result, namely that the variance $s_c^2 = \mu_2$ of the concentration fluctuations is obtained by subtracting the Poisson variance $\bar{M}$ from the variance ($<M^2> - <M>^2$) in the recorded data.

The higher moments of interest are the third and fourth which are represented respectively by the skewness β_3 and the kurtosis β_4. These are given as[41]

$$\beta_3 = \mu_3/\mu_2^{1.5} \qquad (56)$$

and

$$\beta_4 = \mu_4/\mu_2^2 . \qquad (57)$$

For Gaussian distributions,

$$\beta_3 = 0 \text{ and } \beta_4 = 3 \qquad (58)$$

while for Poisson distributions,

$$\beta_3 = \bar{M}^{-1/2} \qquad (59)$$

$$\beta_4 = 3 + \bar{M}^{-1} . \qquad (60)$$

Although the procedure embodied in Equations (45) and (53) can provide the set of moments of the concentration distribution, it is not sufficient to define the original pdf. Two schemes have been described for arriving at a reasonable approximation of the pdf from the moments. Penney et al.[7] used a least-mean-squares

determination of the amplitude coefficients of a trial function, while Siddall and Diab[42] obtained a realistic approximation by maximizing the Shannon entropy function.[43] No effort to generate approximate pdf's of the concentration from the moments was carried out in the work reported here.

4.2.2.1 Probability Analysis

In all the runs, 4,096 reads were recorded for each channel. In the axial set, a read rate of 2.0 kHz was used out to 4.0 cm, 1.0 kHz at 7.0 cm, and 0.5 kHz for $Z > 7.0$ cm. In the radial set, 2.0 kHz was used for $X < 0.4$ cm and 0.2 kHz for $X > 0.4$ cm. The lower read rates were used to prevent the Poisson uncertainty from getting too large for the CO_2 concentration measurements. Two examples typical of the probability analyses of these data are shown in Figure 29. The bin widths in both cases are approximately Poisson. In the air channel, the mean signal level was 40 kcounts/s which made the rms concentration 65% of the Poisson uncertainty, while in the CO_2 channel the mean signal was 245 kcounts/s which made the rms concentration 107% of the Poisson level. These differences are reflected in the breadth of the pdf's given in Figures 29(a) and (b).

From the pdf studies, the mean and rms concentration values were obtained. These data for the axial sets are given in Figure 30. To put the rms values on the same footing, the rms profiles in Figure 30(b) were computed for a 0.5-kHz read rate at all positions. The mean concentration values were found to be insensitive to the choice of read rate, as expected.

The effect of the choice of read rate on the rms concentrations was of some concern in these studies. However, it was found that the difference between the rms concentration values at 0.5 and 2.0 kHz was almost entirely due to the difference in bandwidth. For example, for the $Z = 4.0$ cm (3.4d) data at 6 kg/h, the measured standard deviation s_m of the total
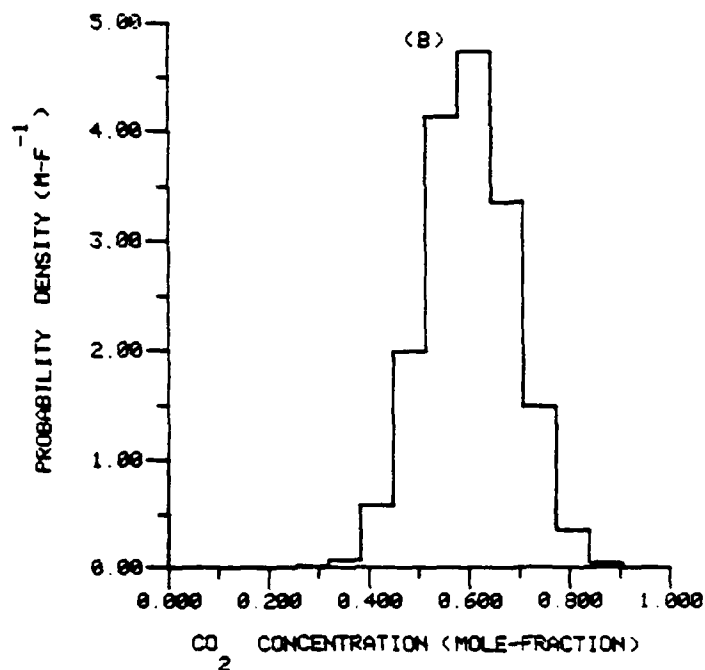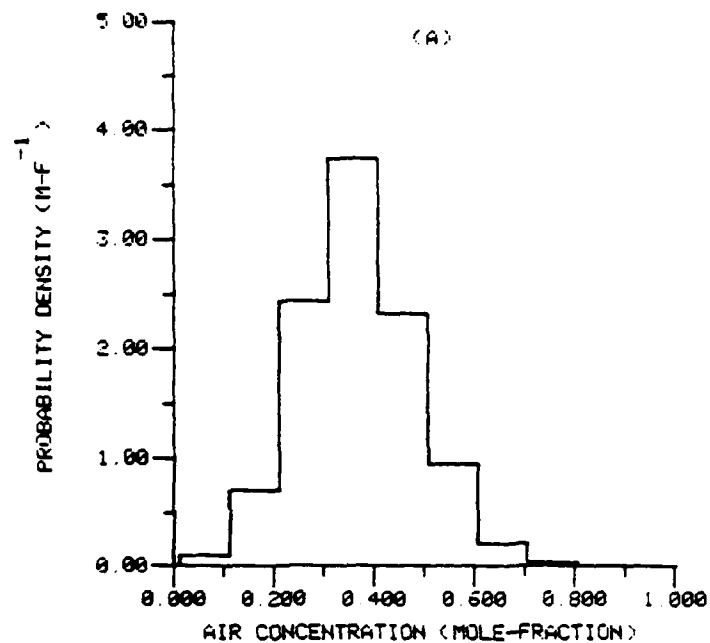
Figure 29.   Typical Concentration PDF's Obtained from
              Simultaneously Recorded Data On-Axis at Z = 4.0 cm
              (8.39d) for a 2.0-kg/h CO_2 Flow Rate; (a) Air;
              (b) CO_2.   (Data records have 4096 reads taken at
              2.0 kHz read rate. Bin widths are approximately
              equal to the Poisson uncertainties.)

101
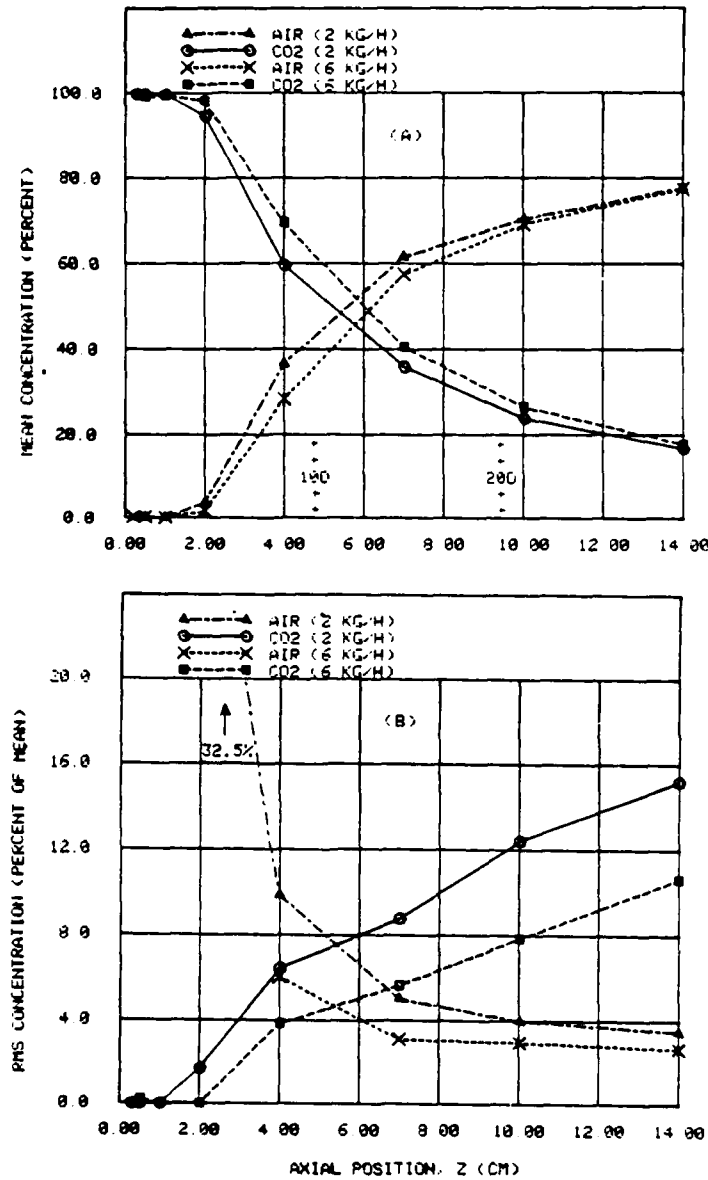
Figure 30. Axial Profiles of Air and CO_2 Concentrations Measured Simultaneously for 2.0 and 6.0 kg/h Flow Rates and 0.5 kHz Read Rate; (a) Mean Concentrations; (b) Relative RMS Concentrations.

102

Raman data of CO_2 at 500 Hz is 0.0416 mole-fraction (m-f). If a flat power spectrum is assumed (i.e., due to white noise), then $s_m \propto \sqrt{f_r}$; thus, at 2.0 kHz, this would give $s_m = 0.0832$ m-f. The actual value obtained at 2.0 kHz is $s_m = 0.0775$ m-f. The difference is due to the fact that the power spectral density due to the concentration is not white but decreasing slowly towards the Poisson spectral density as the frequency increases. Since the Poisson standard deviation s_p is proportional to $\sqrt{f_r}$ as given in Equation (43), then the power spectral density due to the fluctuations of the detection process given by $2s_p^2/f_r$ is independent of the read rate (where the bandwidth BW = $f_r/2$). Thus, the choice of read rate determines simply the bandwidth of the power spectrum that is integrated to give the observed value of s_m. As discussed in Section 4.1.2.2, the only situation in which the read rate becomes a real concern is when there is a peaked feature or resonance at a frequency higher than $f_r/2$. None of the data from the CO_2 studies show any evidence of a high-frequency feature.

The deviation of the total concentration from 99 to 100% due to calibration drift discussed in the previous section is clearly evident in Figure 30(a); however, the data show good symmetry in spite of this systematic error. A similar study of the mean CO_2 concentration profile due to a nozzle identical with the one used in these studies was carried out using a gas-sampling probe in the 25.4-cm-diameter APL combustion tunnel operated out of Room 20 in Building 18 of W-PAFB.[44] The jet nozzle was axially positioned in the face of a 14.0-cm-diameter centerbody. An annular air flow of 0.7 kg/sec was used to sweep the CO_2 from the tunnel. The Raman values shown in Figure 30(a) are consistently higher than the probe values for Z > 2.0 cm (4.2d). The averages of these differences are 5.0% and 4.5% respectively for the 2.0 and 6.0 kg/h flow rates. For the 2.0 kg/h flow rate, the Raman value is 1.8% higher than the probe value also at Z = 1.0 cm (2.1d). The values for the remaining positions in the two data

103

sets with $Z < 2.0$ cm were within 0.3% of each other. The peak discrepancy in the 2.0-kg/h data was 10.0% at $Z = 2.0$ cm, whereas in the 6.0-kg/h data the maximum was 7.2% at $Z = 4.0$ cm (3.4d). At many positions, three to five probe readings were obtained. The 2.0-kg/h data gave uncertainties generally under 1% while the 6.0-kg/h data gave uncertainties of 3.9% and 2.0% respectively at $Z = 2.0$ cm and 4.0 cm. Clearly, these uncertainties are not enough to account for the discrepancies between the Raman and probe data. Furthermore, the probable accuracy error in the Raman data, due primarily to the calibration drift, is about 2.0% low as suggested by the deviation of the total concentration from 100%. Thus, accounting for this error only increases the discrepancies between the probe data and the Raman data. Although the APL study was, in fact, on ducted flow of a jet while the Raman study was on a free jet, the discrepancies are in the region well before one centerbody diameter. This tends to minimize the differences in the experimental configurations. The implication is that one technique has an uncorrected bias. The reasonably good consistency between the air and CO_2 data shown in Figure 30(a) suggests that any bias in the Raman data is small. We note that the probe data did reveal an asymmetry in the radial profile data which could suggest that the tunnel axial measurements did not follow the flow axis.

Birch, et al.[37] fit their axial data to a hyperbolic function consistent with theoretical expectations. Thus, plotting the reciprocal of the mean concentration versus axial position should give a straight line. The Raman data gave reasonable fits in the 2.0 to 14.0 cm range with rms deviations from the fits of 7.2% and 4.7% respectively for the 2 and 6 kg/h flow rates. The probe data, however, gave 12.4% and 17.2% rms deviations for the corresponding runs.

The rms concentration values for air in Figure 30(b) could not be determined for $Z < 1.0$ cm (2.1d) due to the low concentration of air. Measurements were taken only at the points plotted in Figure 30. A point of interest in these data occurs when the concentrations are equal. In Figure 30(a), equality is about 49% for both flow rates at $Z = 5.4$ cm (11.3d) and 6.1 cm (12.8d) respectively for 2.0 and 6.0 kg/h. In Figure 30(b) for 2.0 kg/h, the air and CO_2 "curves" cross exactly at 5.4 cm; however, so also do the 6.0-kg/h "curves". At equal concentrations, since the mole-fractions of the two gases are anticorrelated, we should expect equal rms values as given by the 2.0-kg/h data. The most likely implication regarding the 6.0-kg/h data in Figure 30(b) is that the measurements of the air concentration fluctuations are too low, at least relative to the CO_2 values.

The results of the radial measurements are given in Figure 31. The mean profiles in Figure 31(a) show excellent anti-correlation with an equal-concentration value of 50% at $X = 0.28$ cm (1.17r). The radial profiles of the rms concentration values for air and CO_2 are given in Figure 31(b). The measurements could be carried out only to $X = 0.4$ cm at 2.0 kHz read rate after which the CO_2 concentration was too weak for viable fluctuation measurements. The radial data beyond $X = 0.4$ cm was recorded at 0.2 kHz. The plots for the two read rates show good consistency with each other and between the two gases. However, Figure 31(b) shows that equal rms values of the two gases occur at slightly different positions compared to the crossing of the mean values. In particular, for 0.2 kHz read rate, the rms values cross at $X = 0.23$ cm while, at 2 kHz, they cross at $X = 0.25$ cm. The implication of these results is that while a read rate of 2.0 kHz was adequate for the 2.0-kg/h flow, at least with regard to rms profiles, it was not high enough to record the fluctuations present in the 6.0-kg/h flow.
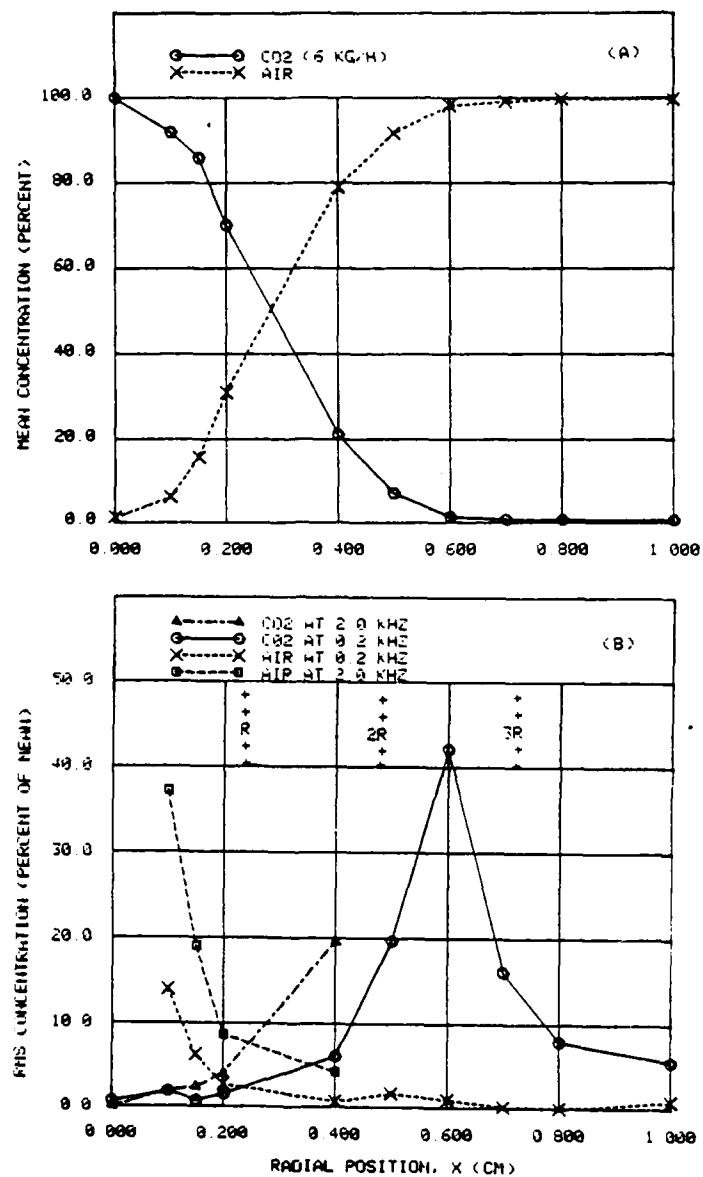
Figure 31.   Radial Profiles of Air and CO_2 Concentrations
Measured Simultaneously for 6.0 kg/h Flow Rate at
$Z = 2.0$ cm (4.19d); (a) Mean Concentrations; (b)
Relative RMS Concentrations.

106

A significant feature in the rms data is the peak in the percent rms concentration of CO_2 at $X = 0.6$ cm (2.52r). This would appear to define a very clear boundary of the mixing region. We note that the air fluctuations do not show a similar behavior of such magnitude.

A more precise analysis of the fluctuation measurements can be carried out using the covariance between the air and CO_2 fluctuations. The assumed constancy of temperature and pressure dictate that the total of the mole fractions is unity throughout the series of measurements. Since the air and CO_2 mole fractions constitute at least 99% of the gas in the observed volume, we can write

$$c_a + c_c = 1 , \tag{61}$$

where c_a and c_c are respectively the air and CO_2 mole fractions. Then the variances in these quantities given by s_a^2 and s_c^2 are related as

$$s_a^2 + s_c^2 + 2s_{ac}^2 = 0$$

or, if we define a normalized covariance T as

$$T \equiv \frac{2s_{ac}^2}{s_a^2 + s_c^2} , \text{ then } T = -1 , \tag{62}$$

where s_{ac} is the covariance between c_a and c_c and is estimated using

$$s_{ac}^2 = \frac{1}{N} \sum_{i=1}^{N} [(c_{ai} - \bar{c}_a)(c_{ci} - \bar{c}_c)] , \qquad (63)$$

where N is the number of data pairs or reads (N = 4,096 here).

The measured values of covariance are plotted in Figure 32. The axial data in Figure 32(a) shows, in particular, a lower covariance at 6.0 kg/h than at 2.0 kg/h, which ties in with the lower-than-expected air rms values at the higher flow rate. Similarly the radial data at 0.2 kHz read rate in Figure 32(b) show low covariance values consistent with the low air rms data in Figure 31(b). These characteristics can be made quantitative by calculating T in Equation (62). This quantity can be used as a test for self-consistency of the data. For both air and CO_2, the rms values (i.e., s_a and s_c) were obtained from the data as described by Equations (44) through (55). This involved a subtraction of constant background levels as well as the Poisson variance. In addition, the "true" air values had to be obtained by a subtraction of a fraction of CO_2 concentration from the apparent air values. These manipulations plus the fact that the background levels were really not constant and that the CO_2 fraction in the air channel was probably not constant all indicate the likelihood of $T \neq -1$. It should be noted here that a calculation similar to Equations (44) to (55) carried out for finding s_{ac}^2 shows that Equation (63) gives the covariance between the fluctuations of the light signals. In effect, the Poisson noise signals in the two variables are completely uncorrelated, and therefore, do not contribute to s_{ac}^2. Thus, the closeness of T to -1 is an indication of the correctness of both the measurement and calculations of the fluctuations.
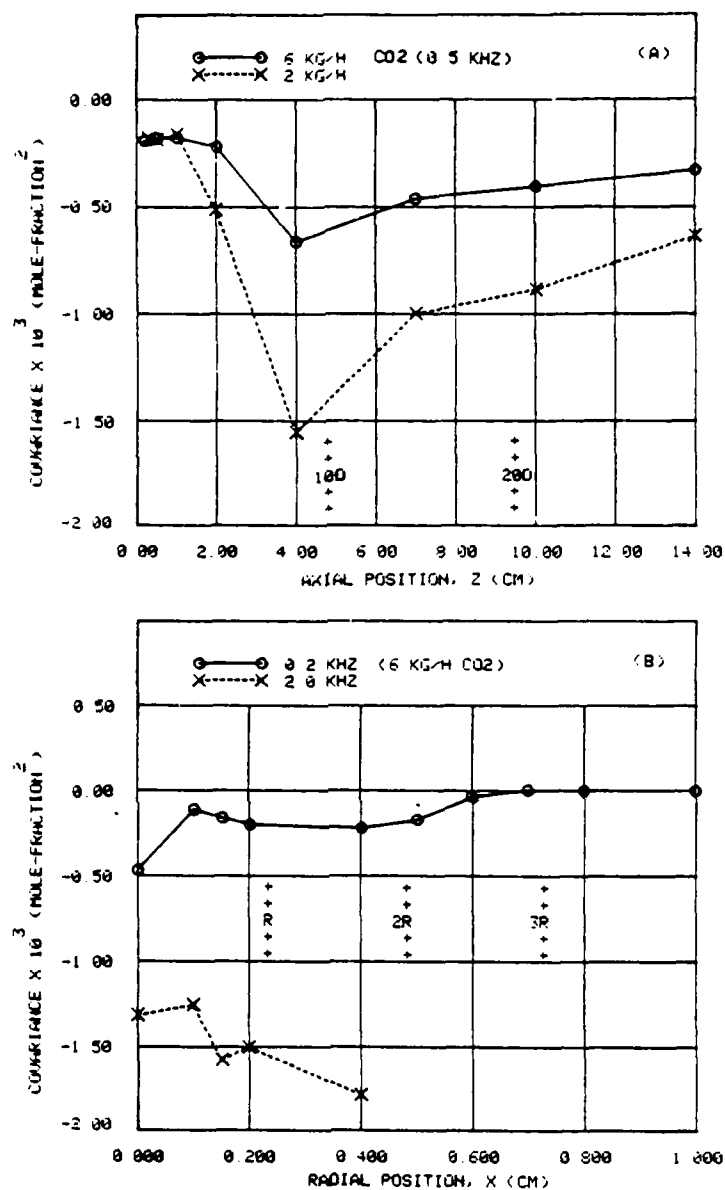
Figure 32. Air-CO_2 Concentration Covariance Profiles; (a) Axial;
(b) Radial at $Z = 2.0$ cm (4.19d).

The meaning of $T = -1$ is that the two variables are perfectly anticorrelated. In this instance, we have that $s_a = s_c$. This result allows us to define a "quotient factor" q as

$$q \equiv 2s_a s_c / (s_a^2 + s_c^2) \qquad (64)$$

which equals unity only when $s_a = s_c$ and is less than unity whenever $s_a \neq s_c$, regardless of which quantity is small. This factor allows us to test the rms values of concentration independent of the covariance. The values of T and q are given in Table 3 for positions where the air or CO_2 signal levels are not excessively low. We note that the ratio T/q is the linear correlation coefficient which cannot exceed the magnitude of unity. Clearly, this ratio in Table 3 does exceed unity which indicates a bias in the data. The values of q and the rms values themselves indicate that the air rms values are low for the high flow rate. The suggestion is that the air fluctuations are not being adequately resolved. This is supported in the radial data by the closer proximity of q to unity at the higher read rate.

Thus, the results given in Table 3 lead to two conclusions. First, there is a bias in the data which becomes worse at the high flow rate, particularly off axis. Second, the air rms values are too low except, perhaps, at the low flow rate. The degree to which these two discrepancies are connected is not clear. However, the implication of all these data is that the measurements made in the flowfield where the turbulence was fairly high either did not adequately detect the fluctuations in the air concentration or that there is a breakdown of the assumed conditions in the observed volume.

TABLE 3

Normalized Covariance T and Quotient Factors q for CO_2 Jet

CO_2 Flow (kg/h)	Read Rate (kHz)	Profile	Position (cm)	T	$\bar{T}$	q	$\bar{q}$
2.0	0.5	Axial (Z)	4.0	−1.11		0.998	
			7.0	−1.01	−1.02	1.000	0.999
			10.0	−1.05	±0.066	0.998	±0.001
			14.0	−0.91		0.998	
6.0	0.5	Axial (Z)	4.0	−1.31		0.907	
			7.0	−1.09	−1.05	0.970	0.969
			10.0	−0.94	±0.16	1.000	±0.043
			14.0	−0.84		0.997	
6.0	0.2	Radial (X)	0.1	−0.53		0.79	
			0.15	−2.07		0.94	
			0.20	−2.02	−1.19	0.97	0.89
			0.40	−2.13	±0.99	0.74	±0.10
	at Z = 2.0 cm		0.50	−0.76		0.99	
			0.60	−0.53		0.89	
6.0	2.0	Radial (X)	0.1	−2.90		0.978	
			0.15	−2.38	−2.13	0.936	0.973
			0.20	−1.99	±0.70	0.999	±0.027
	at Z = 2.0 cm		0.40	−1.25		0.980	

The latter possibility includes nonconstancy of temperature and/or pressure, differences between the O_2 and N_2 molecules, and the contributions of the minor constituents of air. Of these, changing temperature is a possible source of difficulty. This is due to the Joule-Thompson cooling of the CO_2 gas due to expansion at the pressure regulator. Since the gas was preheated to offset this cooling, it is not obvious that this is a significant contributor to the bias.

Inadequate detection of the air fluctuations could be due to a bias in the measurement scheme. For example, the observed volume is a very thin, flat, bow-tie-shaped figure. If all gas molecules, on the average, independent of their positions in the flowfield, move through the volume in all directions, or if they move slowly in one direction, the measurements should be self consistent. On the other hand, if the two gases move differently at different positions, the shape of the observed volume becomes a factor in the fluctuation measurements. Basically, the larger the size of a particular dimension of the observed volume, the greater will be the integration of the fluctuations of concentration that arise from molecules moving with a component parallel to that dimension. Since the long dimensions of the volume in these studies were transverse (X and Y axes) to the flow axis (Z) and the radial measurements were particularly inconsistent, presumably due to the low rms air values, it is suggested that the component of velocity of the air molecules transverse to the flow axis increased significantly relative to the CO_2 molecules in the 6.0-kg/h flow compared to the 2.0 kg/h flow. This would seem to be consistent with the larger molecular weight of CO_2 relative to O_2 and N_2 and the elementary behavior of objects in elastic collisons. Thus, it is suggested that the shape of the observed volume in an optical measurement of a gas variable introduces a bias in the measurements of the fluctuations of that variable which depends on the movement of the gas. This hypothesis can easily be tested using the TiLaPS

112

system simply by doing a radial profile study along the Y axis. This would change the orientation of the observed volume relative to the flow axis. Also, the length of the Y-dimension of the observed volume can easily be changed thereby changing the sensitivity of the measurement to the motion of the gas.

The third and fourth moments of the raw air and CO_2 data were calculated in order to determine the skewness β_3 and the kurtosis β_4 of the concentration pdf's. Because of the need for corrections and the possibilities of significant biases in the air measurements, these quantities for the air concentration pdf's are not presented. The results of these calculations for the CO_2 data are given in Figure 33. Both axial and radial data are presented in this figure and the axial data are given, where possible, for both 0.5 and 2.0 kHz read rates. The reduction of read rate was accomplished by combining successive reads in the data set. For example, since the original 2.0-kHz data sets had 4,096 reads, the reduction to a 0.5-kHz read rate reduced the number of reads to 1,024. Except for the 2.0-kHz value at $Z = 2.0$ cm (4.2d), the skewness shows a tendency to become slightly negative with increasing Z. The rather striking skewness at $Z = 2.0$ cm (4.2d) for the 2.0-kHz read rate and 2.0-kg/h flow rate and the corresponding large kurtosis can be attributed in part to the fact that the concentration values are limited to unity mole fraction, and therefore, presents a limit on the instantaneous values that are possible. This argument can also be applied to the large values of β_3 and β_4 obtained from the radial data.

One source of the difficulty in these data is suggested by the changes in β_3 and β_4 with read rate at the positions close to the nozzle. At these positions the CO_2 concentration fluctuations are small and, because the mean concentrations are high, the absolute "Poisson" noise levels are high. When the read rate is high, the count per read is low and the uncertainties in the moment determinations are large. As seen at
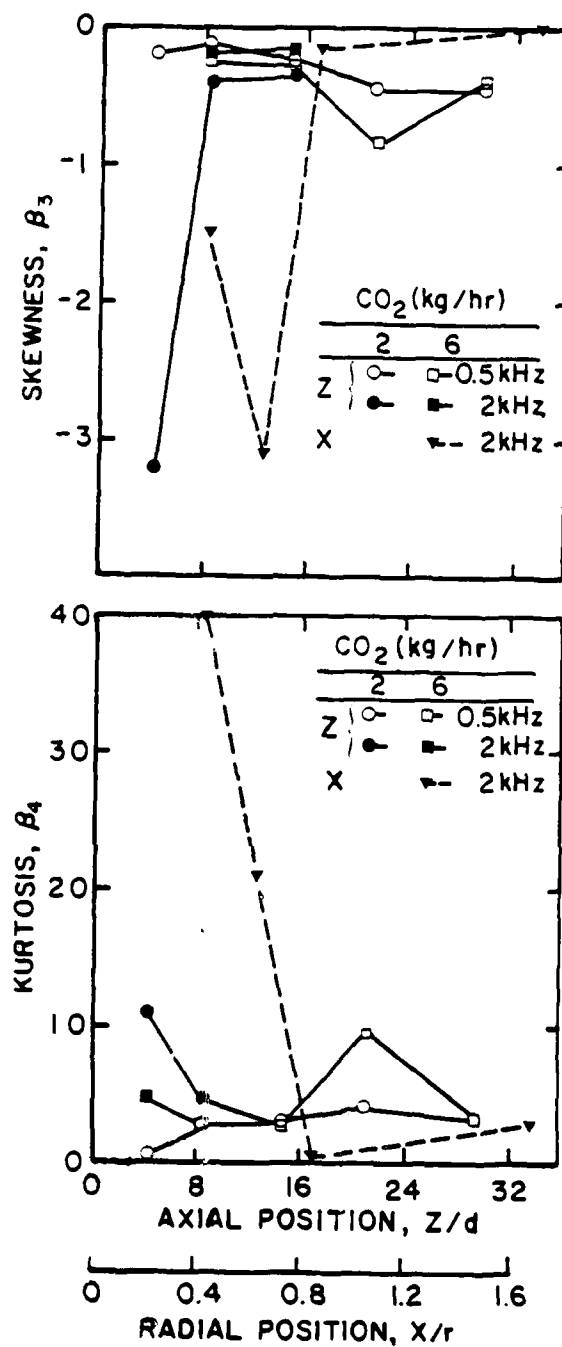
113

Figure 33. Skewness and Kurtosis of the CO_2 PDF's of the Axial and Radial Data. (Radial data at $Z = 4.19d$. Note read rates given in legend.)

114

$Z/d = 8.4$ and $Z/d = 14.7$, read rate had a somewhat smaller influence on the values of β_3 and β_4 than at $Z/d = 4.2$ consistent with the higher rms values at these positions compared with positions closer to the nozzle. Nevertheless, the distortion of the pdf's implied by high $|\beta_3|$ and/or β_4 is clearly evident in the pdf's shown in Figures 34(a) and (b). The increased bandwidth that accompanies increased read rate may reveal features in the pdf due to fast fluctuations that are not seen at lower read rates. For comparison, a pdf having "reasonable" values of β_3 and β_4 is given in Figure 34(c). We note that most of the β_4 values for $Z/d \geq 8.4$ are close to 3.0 as suggested by Equations (58) and (60). An interesting exception to this result is the 6.0-kg/h data at $Z = 10.0$ cm (20.1d). The data set shows a rather sizable increase in $|\beta_3|$ and β_4 compared to the 2.0-kg/h values. This result suggests that an extensive study of the dependence of β_3 and β_4 on flow rate may reveal some interesting properties of the flowfield.

4.2.2.2 Spectral and Correlation Analyses

The psdf's of a number of the pairs of data sets were computed and examined. Generally, they were nearly flat (i.e., "white") or had a slow $1/f^2$ dependence. Typical examples of these spectra are shown in Figure 35 for $Z = 4.0$ cm (8.4d), 2.0 kg/h CO_2 flow, and a 2.0 kHz read rate. These spectra were computed by averaging 61 segments obtained by overlapping successive segments by three quarters of a segment length, where each segment had 256 points. In addition, a 50-Hz-wide "filter" function was applied to the spectra. The widths of the "noise" peaks in the spectra given in Figure 35 reveal this filter characteristic. The dashed lines identify the calculated power spectral density due to the Poisson noise. If the two spectra given in Figures 35(a) and (b) are overlaid such that the two dashed lines coincide, the general shape and strength of the spectra appear identical within the uncertainties of the apparent "noisy" character of the curves. Interestingly, there are some features of this "noise" that appear almost identically in the
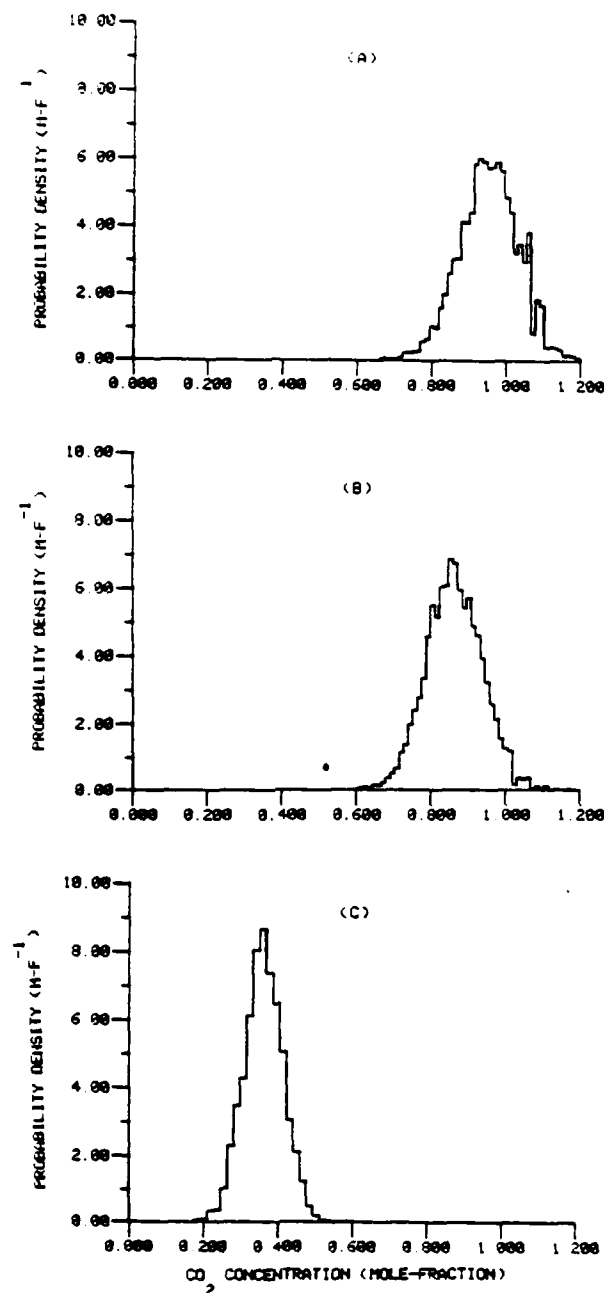
Figure 34. CO_2 Concentration PDF's Plotted with Minimum Bin
Widths to Reveal Shapes; (a) On-Axis at Z = 2.0 cm
(4.19d) at 2.0 kHz Read Rate for 2.0-кg/h CO_2 Flow
Rate; (b) At X = 0.4 cm (1.68r) and Z = 2.0 cm
(4.19d) at 2.0 kHz Read Rate for 6.0-кg/h CO_2 Flow
Rate; (c) On-Axis at Z = 7.0 cm (14.7d) at 1.0 кHz
Read Rate for 2.0-кg/h CO_2 Flow Rate.

116
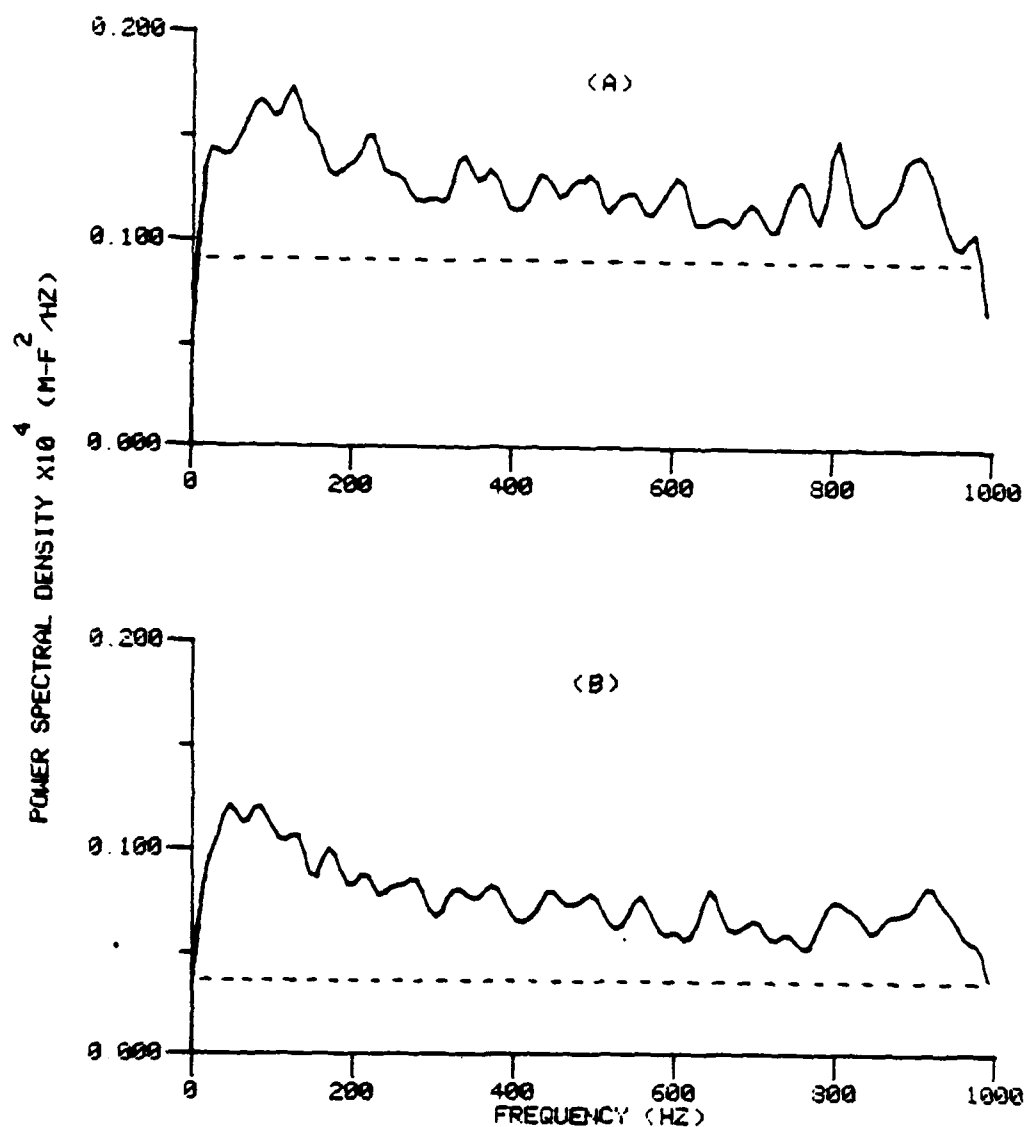
Figure 35. Concentration PSDF's Obtained from Simultaneously
Recorded Data On-Axis at Z = 4.0 cm (8.38d) for a
2.0-kg/h CO_2 Flow Rate; (a) Air; (b) CO_2. (Data
records have 4096 reads taken at 2.0 kHz read rate.
Spectra are averages over 61 three-quarter
overlapping segments of 256 points each and a 50-Hz
cosine filter. Dashed lines are the calculated power
spectral density due to "Poisson noise".)

117

two spectra. More detailed measurements are needed to resolve this matter.

Applying the $1/f^2$ analysis to Figure 35(a) similar to that used to analyze the temperature psdf's using Equation (41), we obtain $t_c \sim 0.47$ ms and $K_G \sim 0.56$ m-f^2 Hz. This integral time scale is about equal to the read time interval Δt which means that the acf's of those data will not reveal this property of the data. This fact is clearly seen in the acf's given in Figures 36(a) and (b). These acf's are averages of 16 nonoverlapping segments with 256 points each. Clearly, all the fluctuations have correlation times shorter than the 0.5 ms time delay resolution of the data. It is important to note that the detailed shape and strength of the psdf's shown in Figure 35 are independent of the read rate. A lower read rate simply reduces the maximum bandwidth of the spectrum that can be obtained from that data. Of course, as seen in Figure 35, there is an increased noise level in the power spectrum as the frequency increases, which distorts the spectrum near $f_r/2$.

As the integral time scale shortens below the read time, the spectrum flattens. The spectrum looks like white noise. This suggests that whenever an apparently white noise level is obtained, there is a random process with an integral time scale somewhat shorter than the read time interval. This was observed in most of the psdf's computed from the 6.0-kg/h data, which means that this Reynolds number flow of 30,000 has an integral time scale somewhat less than 0.5 ms. Thus, read rates of at least 5 kHz are needed to accurately probe such flowfields. This is in agreement with the studies of Birch, et al.[37]

The ccf given in Figure 36(c) confirms the fast character of the fluctuations. It also shows the expected anticorrelation of the concentration of the two gases.

118
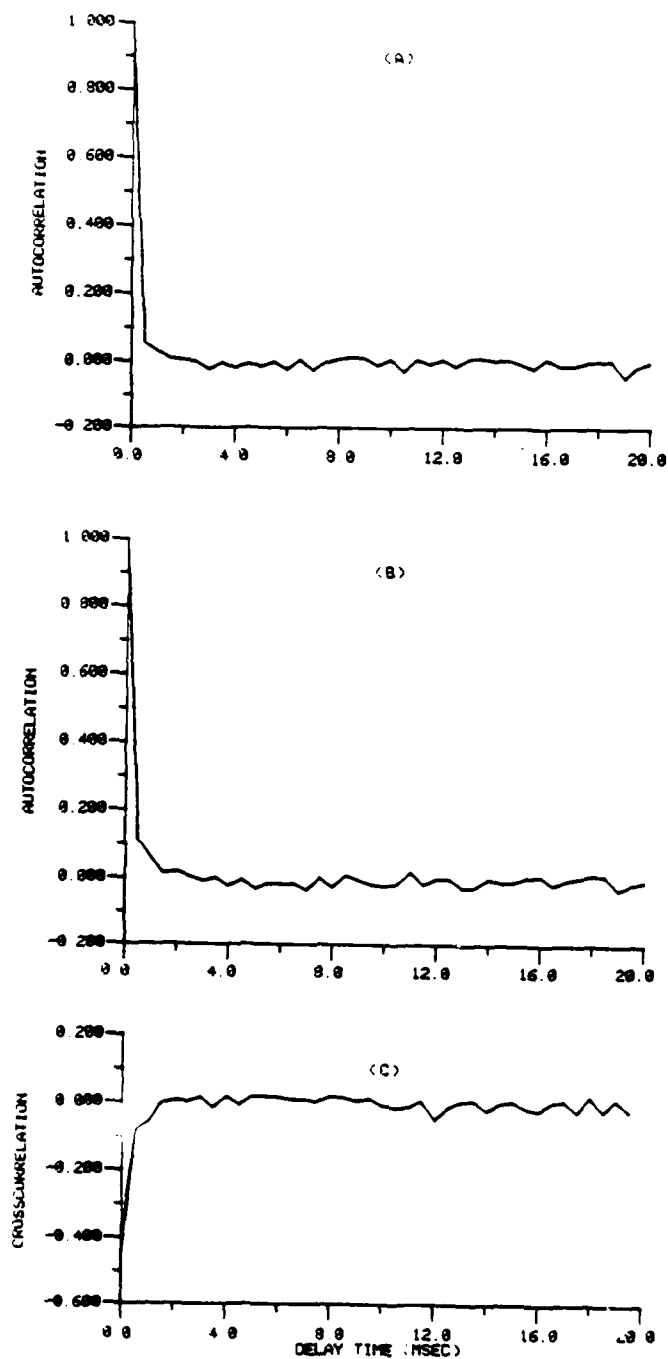
Figure 36. Concentration Correlation Coefficients of Data used in Figure 35; (a) Air ACF; (b) CO_2 ACF; (c) Air-CO_2 CCF. (Functions are averages of 16 non-overlapping segments of 256 points each.)

119

In summary, the spectral analyses showed that the fluctuations consisted of a $1/f^2$ contribution with an integral time scale about equal to the read time interval, an apparently flat or white noise contribution, and the usual Poisson contribution. In the CO_2 data given in Figures 35 and 36, the apparent white noise is about 20% of the total measured variance while the $1/f^2$ contribution is about 33%. The remainder is due to the Poisson contribution.

SECTION 5

CONCLUSIONS

We have shown that dynamic and simultaneous two-channel spontaneous Raman measurements can be carried out in cold flow or a flame using the pure rotational lines. The data obtained from a room-temperature CO_2 jet and a CH_4 diffusion flame yielded to analyses involving pdf's, psdf's and acf's. The results of these analyses were reasonably consistent with the published results of similar studies.[15,37] Although not accomplished in this work, the potential for accurate temperature measurements near 2,000 K at read rates of 100 Hz using the TiLaRS concept was shown. Increases in the spectrometer throughput, the gain of the multi-pass cell and the optimization of other factors in the TiLaRS system indicate that this frequency can be increased by at least a factor of two. Clearly, the maximum read rate depends not only on the maximum temperature to be measured but also the total number of reads that can be recorded. For example, an increase in the number of reads by 16 would permit an increase in the maximum read rate by a factor of four for the same precision in the mean measurement.

In this work we developed and made operational a set of computer programs designed to handle the data acquisition, the data analysis, and the presentation of the data in the form of computer-generated plots. These programs provide a large degree of flexibility in the various stages of measurement and analysis.[27]

The two-channel TiLaRS system uses a relatively simple but unique modification of the exit-slit image of a conventional double spectrometer. The performance of the exit-slit optical system and multipass optical cell were in good agreement with the original design goals. We have established a dependable and consistent procedure for adjusting and calibrating the TiLaRS

system and have identified the most likely sources of error in this procedure and in the measurements.

These studies have shown the importance of the Poisson uncertainty in the evaluation of the real-time data. We also have shown how to properly account for this uncertainty in each type of data set. This includes simultaneous temperature and concentration measurements as well as simultaneous measurements of the concentrations of two gases at constant temperature and pressure. Furthermore, the problem of interference by one gas with the measurements of the other gas has been successfully resolved for at least the mean and rms values of the concentrations.

It is clear that the performance of the current TiLaRS system is optimum at temperatures below 1,200 K, particularly for room-temperature studies. It should also be noted that temperature measurements in environments such as nonmethane flames, where there are a large variety of molecular species in the flow, have not been tried. For such measurements to have a reasonable probability for success, a third channel would be required for measuring the background signal.

Among the results of the studies, we have determined that the shape of the temperature pdf of a noncombusting gas is consistent with the predictions of a Gaussian total-number-density pdf transformed via the ideal gas law at constant pressure to the temperature pdf. We have identified the interesting presence of a $1/f^2$ component in the temperature fluctuations of the CH_4 flame front and in the concentration fluctuations of the CO_2 jet. This temperature fluctuation component is consistent with reported flame front measurements.[45] It is interesting that the N_2 concentration fluctuations associated with the above temperature measurements did not show a $1/f^2$ behavior. The CO_2 jet studies also revealed the possibility of an important bias associated with the size and shape of the observed volume and the flow direction of the gas

relative to that volume. Such a bias would not be apparent in single-channel dynamic measurements.

The essence of the difference between the TiLaRS concept compared to systems that use a low-repetition rate, high-peak power laser is that in the TiLaRS system we strive to acquire a very large number of measurements, namely on the order of 10 to 100 times more data than has been typical with a low-prf laser.[6,17] This quantity of data permits small contributions of the thermodynamic variable being studied to be extracted with reasonable precision from the data sets where the information determined from a single read of the set would not be useful. As dramatically seen in our efforts to obtain smooth psdf's, the determination of the shape and magnitude of pdf's, psdf's, or acf's for example, or any parameter for that matter, associated with a more-or-less random variable (i.e., noise) to some useful degree of precision requires a very large number of measurements. Of course, the sacrifice made in the TiLaRS approach was to restrict the measurements to those flowfields that have no significant interferences from "minor" species. Actually, in the flame studies reported here, there undoubtedly were interferences from CO, CO_2, and/or H_2O which were not too significant because of the inability to measure temperatures in the combustion zone. In the future these will have to be dealt with. These inter-ferences present a challenge primarily to the resolution of the instrument and the skill of the experimenter but not the feasibi-lity of the technique. The technique is intrinsically simple and the data relatively easy to reduce to the desired variable. These are important features if a very large quantity of data is to be recorded and processed. It is evident that a large quan-tity of data, at least ~2,000 values, are needed to quan-titatively characterize the statistical properties   the type of random variables that are associated with turbulent flowfields.

SECTION 6

RECOMMENDATIONS

The recommendations fall into three categories: techniques, apparatus, and measurements. These recommendations concern principally the optimization of the TiLaRS approach and the exploration of its capabilities. They are presented roughly in order of decreasing priority. The priorities are arranged to achieve optimum capability in flame measurements. Some of the priorities would change if cold flow measurements are emphasized.

Techniques:

a.   Modify the exit slit and exit-slit optics to permit a wider opening so as to allow $\Delta J = 4$ in temperature measurements.

b.   Determine the modifications of the beam-insertion technique and/or optical characteristics of the laser beam necessary to obtain higher gains with the multipass cell.

c.   Design software to permit recording runs having at least 16 K samples per channel.

d.   Add an independently-adjustable third channel to permit simultaneous measurement of the background signal level. This includes software and computer modifications to handle the third channel.

e.   Use a shorter focal length lens for the collection lens L_1 so as to increase the solid angle of light collection in flame measurements.

f.   Replace L_4 in Figure 11 with two shorter focal-length, plano-convex cylindrical lenses to reduce aberrations and light loss.

g. Add a channel to record the Rayleigh scattering intensity simultaneous with the Raman measurements.

h. Add a channel to record the vibrational Raman band of methane simultaneous with the rotational Raman channels.

i. Develop a method to record the intensities of two or more spectral lines in a given channel so as to enhance the signal-to-noise ratio at high sampling rates. This would require the development of new analysis software.

j. Develop software to fit a pdf to a set of moments obtained from cold flow measurements.

Apparatus:

a. Replace the current ruled gratings with holographic gratings so as to reduce the scattered laser light in the Raman channels. This is a minimal recommendation. A much more sizable improvement in throughput, reduction of scattered laser light, number of available channels (at least five), and overall performance can be achieved only through the acquisition of a new spectrometer.

b. Modify the current slit height control or replace it in order to obtain continuous adjustability over zero to 5 mm.

c. Replace the data acquisition hardware and software with a system that has more memory, is faster, is more user friendly, and which can handle a wider variety of real-time I/O functions than the current Data General Nova minicomputer.

d. Devise apparatus to protect the PMT's from accidental exposure to excessive light levels.

e. Acquire a photon correlator for Raman and Rayleigh studies in cold flow and Rayleigh studies in flames.

Measurements:

a.   Study the influence of observed-volume size and orientation
on the measured moments in an axial-symmetric, cold flowfield.

b.   Do a more intensive study of a well-characterized flame to
explore the shape changes of the temperature and N_2 concentration
pdf's.

c.   Investigate fully the nature of the $1/f^2$ behavior of the
temperature fluctuations of the flame front.

d.   Do N_2 concentration measurements in the flame where the
Poisson uncertainty is minimized using Equation (39).

e.   Carry out measurements of Rayleigh scattering and/or Raman
scattering from the methane vibrational band simultaneous with
the rotational Raman measurements in a well-characterized flame.
This would include the case where the gases are chosen to give a
nearly constant Rayleigh scattering cross section throughout the
flowfield so as to permit temperature calculations from the
Rayleigh data.   These results could be compared to the Raman-
determined temperatures.

f.   Do cold flow measurements in a well-characterized, two-
component flowfield using various gases and flow rates.   The
effort here would be to study the behavior of the moments and the
time scales of the fluctuations of the two gases and how they
relate to the mixing process.

REFERENCES

1. M. Lapp, "Flame Temperatures from Vibrational Raman Scattering," in Laser Raman Gas Diagnostics, edited by Marshall Lapp and C. M. Penney (Plenum Press, NY 1973), pp. 107-145.

2. R. E. Setchell, "Analysis of Flame Emissions by Laser Raman Spectroscopy," presented at the 1974 Spring Meeting, Western States Section of the Combustion Institute (Washington State University, Pullman, WA, May 6-7, 1974), Paper WSS/CI 74-6.

3. J. H. Bechtel, "Laser Probes of Premixed Laminar Methane-Air Flames and Comparison with Theory," in Laser Probes for Combustion Chemistry, edited by David R. Crosley (American Chemical Society, Washington, D. C., 1980), pp. 85-102.

4. W. M. Roquemore and P. P. Yaney, "Comparison of Thermocouple, Gas Sampling, and Raman Measured Temperatures in an Afterburning Turbojet Engine Plume," in Proceedings of the 10th Materials Research Symposium, on Characterization of High Temperature Vapors in Gases, edited by John W. Hastie (National Bureau of Standards Special Publication 561/1, Super. of Doc. U. S. Government Printing Office, Washington, D. C., 1979), pp. 973-1025.

5. P. P. Yaney, R. J. Becker, T. H. Hemmer, and W. M. Roquemore, "Laser Spontaneous-Raman Scattering Applied as a Diagnostic Probe to Practical Combustors," in Proceedings of the International Conference on Lasers '79, Edited by Vincent J. Corcoran (STS Press, McLean VA, 1980), pp. 88-97; P. P. Yaney, Combustion Diagnostics Using Laser Spontaneous-Raman Scattering (Aero Propulsion Laboratory, W-PAFB, OH, April, 1979), Technical Report AFAPL-TR-79-2035.'

6. M. Lapp and C. M. Penney, "Instantaneous Mesurements of Flame Temperature and Density by Laser Raman Scattering," in Proceedings of the Dynamic Flow Conference 1978, edited by Bengt W. Hansen (Sijthoff and Noordhoff, Alphen aan den Rijn, the Netherlands, 1979), pp. 665-683; M. Lapp, "Raman-Scattering Measurements of Combustion Properties," in Laser Probe. for Combustion Chemistry, edited by David R. Crosley (American Chemical Society, Washington, D. C., 1980), pp. 207-230; M. C. Drake, M. Lapp, C. M. Penney, and S. Warshaw, in Proceedings of the AIAA 19th Aerospace Sciences Meeting, Paper AIAA-81-0103 (American Institute of Aeronautics and Astronautics, New York, NY, 1981).

7. C. M. Penney, S. Warshaw, M. Lapp, and M. Drake,
    "Observations of Fast Turbulent Mixing in Gases Using a
    Continuous Wave Laser," in Laser Probes for Combustion
    Chemistry, edited by David R. Crosley (American Chemical
    Society, Washington, D. C., 1980), pp. 247-253.

8. M. C. Drake, M. Lapp, C. M. Penney, S. Warshaw, and B. W.
    Gerhold, "Measurements of Temperature and Concentration
    Fluctuations in Turbulent Diffusion Flames Using Pulsed
    Raman Spectroscopy," in 18th Symposium (International) on
    Combustion (The Combustion Institute, Pittsburgh, PA, 1981),
    pp. 1521-1531.

9. J. S. Bendat and A. G. Piersol, Random Data: Analysis and
    Measurement Procedures (Wiley-Interscience, NY, 1971).

10. L. P. Goss, G. L. Switzer, D. D. Trump, and P. W. Schreiber,
    "Temperature and Species-Concentration Measurements in
    Turbulent Diffusion Flames by the CARS Technique," in
    Proceedings of the AIAA 10th Aerospace Sciences Meeting,
    Paper AIAA-82-0240 (American Institute of Aeronautics and
    Astronautics, NY, 1982).

11. A. C. Eckbreth and P. W. Schreiber, "Coherent Anti-Stokes
    Raman Spectroscopy (CARS): Application to Combustion and
    Gas-Phase Diagnostics," in Chemical Applications of
    Nonlinear Raman Spectroscopy, Edited by A. B. Harvey
    (Academic Press, NY, 1981), pp. 27-87.

12. A. D. Birch, D. R. Brown, M. G. Dodson, and J. R. Thomas,
    "Studies of Flammability in Turbulent Flows Using Laser
    Raman Spectroscopy," in 17th (International) Symposium on
    Combustion, Leeds, England, August 20-25, 1978. (Organized
    by the Combustion Institute, Pittsburgh, PA, 1978). A. D.
    Birch, D. R. Brown, M. G. Dodson, and J. R. Thomas, "The
    Determination of Gaseous Turbulent Concentration
    Fluctuations Using Raman Photon Correlation Spectroscopy,"
    J. Phys. D: Appl. Phys. $\underline{8}$ L167 (1975).

13. I. Chabay, G. J. Rosasco, and T. Kashiwagi, "Species-
    Specific Raman Spectroscopic Measurements of Concentrations
    Fluctuations in Unsteady Flow," J. Chem. Phys. $\underline{70}$, 4149
    (1979).

14. W. R. Fenner, H. A. Hyatt, J. M. Kellam, and S. P. S. Porto,
    "Raman Cross Section of Some Simple Gases," J. Opt. Soc. Am.
    $\underline{63}$, 73 (1973).

15. R. W. Dibble and R. E. Hollenback, "Laser Rayleigh Thermometry in Turbulent Flames," in 18th Symposium (International) on Combustion (The Combustion Institute, Pittsburgh, PA, 1981), pp. 1489-1499.

16. C. M. Penney, R. L. St. Peters, and M. Lapp, "Absolute Rotational Raman Cross Sections for N_2, O_2, and CO_2," J. Opt. Soc. Am. 64 (5), 712 (1974).

17. R. W. Dibble, W. Kollmann, and R. W. Schefer, "Conserved Scalar Fluxes Measured in a Turbulent Nonpremixed Flame by Laser Doppler Velocimetry and Laser Raman Scattering," presented at the 1982 Fall Meeting of the Western States Section of the Combustion Institute (Sandia National Laboratories, Livermore, CA, October 11-12, 1982) Paper WSS/CI 82-52.

18. P. P. Yaney, R. J. Becker, P. D. Magill, and P. Danset, "Dynamic Temperature Measurements of Flames Using Spontaneous Raman Scattering," in Temperature, Its Measurement and Control in Science and Industry, edited by J. F. Schooley (American Institute of Physics, NY, 1982), pp. 639-648.

19. R. Goulard, A. M. Mellor, and R. W. Bilger, "Combustion Measurements in Air-Breathing Propulsion Engines. Survey and Research Needs," Combustion Sci. Technol. 14, 195 (1976).

20. Gerhard Herzberg, Molecular Spectra and Molecular Structure, Vol. 1, Spectra of Diatomic Molecules, (Van Nostrand Reinhold Co., NY, 1950).

21. S. Broderson, "High-Resolution Rotational-Vibrational Raman Spectroscopy," in Raman-Spectroscopy of Gases and Liquids, edited by A. Weber, (Springer-Verlag, NY, 1979). pp. 7-70.

22. A. Weber, "High-Resolution Rotational Raman Spectra of Gases," in Raman Spectroscopy of Gases and Liquids, edited by A. Weber (Springer-Verlag, NY, 1979), pp. 71-122.

23. H. W. Schrotter and H. W. Klockner, "Raman Scattering Cross Sections in Gases and Liquids," in Raman Spectroscopy of Gases and Liquids, edited by A. Weber (Springer-Verlag, NY, 1979), pp. 123-202.

24. A. B. Harvey, "Measurement of Vibrational and Rotational-Transitional Temperatures Independently from Pure Rotational Raman Spectra," in Laser Raman Diagnostics, edited by M. Lapp and C. M. Penney (Plenum Press, NY, 1974), pp. 147-152.

25. M. C. Drake, C. Asawaroenqchai, and G. M. Rosenblatt, "Temperature from Rotational and Vibrational Raman Scattering: Effects of Vibrational-Rotational Interactions and Other Corrections," in Laser Probes for Combustion Chemistry, edited by D. R. Crosley (American Chemical Society, Washington, D. C., 1980), pp. 231-237.

26. P. R. Bevington, Data Reduction and Error Analysis for the Physical Sciences, (McGraw-Hill, NY, 1969), Chapters 3 and 4.

27. P. P. Yaney, R. J. Becker, P. T. Danset, and M. R. Gallis, Operations Manual for the Time-Resolved Laser Raman Spectroscopy System--TiLaRS, (AFWAL Aero Propulsion Laboratory, Contract No. F33615-78-C-2005, December, 1982), UDR-TR-82-157.

28. P. P. Yaney, "Reduction of Fluorescence Background in Raman Spectra by the Pulsed Raman Technique," S. Opt. Soc. Am. 62, 1297 (1972).

29. R. A. Hill, A. J. Mulac, and C. E. Hackett, "Retroreflecting Multipass Cell for Raman Scattering," Appl. Opt. 16, 2004 (1977).

30. The Magnification quoted in Reference No. 18 is in error.

31. See References Nos. 4 and 5 for the previous history of the Spectrometer used here.

32. Statistical Analysis of Waveforms and Digital Time-Waveform Measurements (Frequency and Time Division, Hewlett-Packard Co., February, 1969), Application Note 93.

33. R. B. Blackburn and J. W. Tukey, The Measurement of Power Spectra, (Dover Publications, Inc., NY, 1958).

34. W. K. George, Jr., P. D. Beuther, and J. L. Lumley, "Processing of Random Signals," in Proceedings of the Dynamic Flow Conference 1978, pp. 757-793.

35. P. D. Welch, "The Use of Fast Fourier Transform for the Estimates of Power Spectra: A Method Based on Time Averaging Over Short, Modified Periodograms," reprinted from IEEE Trans. Audio and Electroacoust. AU-15, 70 (June, 1967) in Modern Spectrum Analysis, edited by Donald G. Childers (IEEE Press, NY, 1978), pp. 17-20.

36. L. I. Boehman, private communication.

37. A. D. Birch, D. R. Brown, M. G. Dodson, and J. R. Thomas, "The Turbulent Concentration Field of a Methane Jet," J. Fluid Mech. <u>88</u>, 431 (1978).

38. C. J. Oliver, "Correlation Techniques," in <u>Photon Correlation and Light Beating Spectroscopy</u>, edited by H. Z. Cummins and E. R. Pike (Plenum Press, NY, 1974), pp. 151-223.

39. Chris P. Tsokas, Probability Distributions: An Introduction to Probability Theory with Applications, (Wadsworth Publishing Co., Belmont, CA, 1972) Chapters 4 and 6.

40. <u>Handbook of Physics and Chemistry</u>, 49th Edition, edited by Robert C. Weast (Chemical Rubber Co., Cleveland, OH, 1968-69), pp. D-45 and F-151.

41. <u>Handbook of Mathematical Functions</u>, edited by M. Abramowitz and I. A. Stegun (Dover Publications, Inc., NY, December, 1972), pp. 928-930.

42. J. N. Siddall and Y. Diab, "The Use of Probabilistic Design of Probability Curves Generated by Maximizing the Shannon Entropy Function Constrained by Moments," J. Eng. for Industry (Trans. of the ASME Paper No. 74-WA/DE-2, American Society of Mechanical Engineers, August 1975), pp. 843-852.

43. C. E. Shannon, "A Mathematical Theory of Communication," Bell Sys. Tech. Jour. <u>27</u>, 379 (1948).

44. W. M. Roquemore, private communication.

45. L. Boyer, P. Clavin, and F. Sabathier, "Dynamic Behavior of a Premixed Turbulent Flame Front," in <u>18th Symposium (International) on Combustion</u> (The Combustion Institute, Pittsburgh, PA, 1981), pp. 1041-1049.

END

FILMED

12-83

DTIC